

**PROBING THE SURFACE- AND INTERFACE-SENSITIVE MOMENTUM-
RESOLVED ELECTRONIC STRUCTURE OF ADVANCED QUANTUM
MATERIALS AND INTERFACES**

A Dissertation
Submitted to
The Temple University Graduate Board

In Partial Fulfillment
Of the Requirements for the Degree
DOCTOR OF PHILOSOPHY
(College of Science and Technology)

By
Arian Arab
May 2019

Examining Committee Members:

Alexander X. Gray, Advisory Chair, Department of Physics, Temple University

Xiaoxing Xi, Department of Physics, Temple University

Peter S. Riseborough, Department of Physics, Temple University

Daniel R. Strongin, External Member, Department of Chemistry, Temple University

©
Copyright
2019

By
Arian Arab

All Rights Reserved

ABSTRACT

In this dissertation, we used a combination of synchrotron-based x-ray spectroscopic techniques such as angle-resolved photoelectron spectroscopy (ARPES), soft x-ray ARPES, hard x-ray photoelectron spectroscopy (HAXPES), and soft x-ray absorption spectroscopy (XAS) to investigate momentum-resolved and angle-integrated electronic structure of advanced three- and two-dimensional materials and interfaces. The results from the experiments were compared to several types of state-of-the-art first-principles theoretical calculations.

In the first part of this dissertation we investigated the effects of spin excitons on the surface states of samarium hexaboride (SmB_6), which has gained a lot of interest since it was proposed to be a candidate topological Kondo insulator. Here, we utilized high-resolution (overall resolution of approximately 3 meV) angle-resolved and angle-integrated valence-band photoemission measurements at cryogenic temperatures (1.2 K and 20 K) to show evidence for a V-shaped density of states of surface origin within the bulk gap of SmB_6 . Our temperature-dependent measurements of the valence-band spectra revealed a sharp feature appearing within the bulk gap of SmB_6 at low temperatures. We attribute this feature to a resonance caused by the spin-exciton scattering in SmB_6 , which destroys the protection of surface states due to time-reversal invariance and spin-momentum locking. The near-Fermi-energy spin-exciton-driven scattering is thermally activated and only appears below the temperature of about 25 K. This temperature is considerably lower than the temperature at which the bulk hybridization gap is first observed. Therefore, it is plausible that the formation of the Fermi-liquid, which is

responsible for the surface conduction should only occur at very low temperatures and may be responsible for the plateau in the resistivity at 5 K.

In the second part of this dissertation we investigated the electronic structure of a strongly-correlated oxide NdNiO_3 grown along the unconventional pseudocubic $[111]$ direction and buried under 4 unit cells (u.c.) of an insulating oxide LaAlO_3 . Over the last several decades transition-metal oxides (TMO) have been demonstrated to host a wide variety of strongly-correlated-electron phenomena, such as metal-insulator transitions and high-temperature superconductivity, induced by chemical doping and/or various external stimuli. Until now, majority of the work has been focused on systems grown along the pseudocubic $[001]$ direction. Recently, however, several theoretical proposals have been put forward to utilize TMO heterostructures consisting of a few u.c. grown epitaxially along the $[111]$ direction. Here, we realized the first momentum-resolved soft x-ray ARPES measurement of the valence-band electronic structure of artificial graphene-like Mott crystal NdNiO_3 $[111]$ buried under four u.c. of an insulating oxide LaAlO_3 . Our measurements of the buried Ni $3d$ states near the Fermi level exhibit excellent agreement with the first-principles calculations and establish the realization of an antiferro-orbital order in this artificial lattice. Such ‘engineered’ electronic structure is unique to this quazi-2D crystal and cannot be realized either in the bulk or thin-film nickelates grown along the conventional $[001]$ direction. Our findings open the door for engineering novel polarized Mott-electronic ground states in rare-earth nickelates, as well as other strongly-correlated transition-metal oxides. From the technical perspective, we demonstrate that soft x-ray ARPES can be used to measure the momentum-resolved electronic structure of ultrathin (2 u.c.) layers, buried within complex oxide heterostructures.

ACKNOWLEDGEMENTS

Firstly, I would like to thank my supervisor Dr. Alexander X. Gray for his kind support and considerations throughout my doctoral studies. Without his supervision and sincere effort, I would not be able even to start with my projects. I would also like to thank my colleagues Ravini U. Chandrasena and Weibing Yang for their efforts during the time that I was not able to attend a beamline for our measurements of $\text{LaAlO}_3/\text{NdNiO}_3$ [111].

Special thanks goes to Dr. Peter Riseborough for his kind support and extremely helpful discussions in our joint project on the material SmB_6 .

Our experimental research would not be possible without high-quality samples, grown by the best experts in the field. I would like to express my sincere gratitude to Dr. Jak Chakhalian for providing the $\text{LaAlO}_3/\text{NdNiO}_3$ heterostructure for our photoemission measurements. Special thanks goes to the members of Dr. Chakhalian's group at Rutgers University, specifically Dr. Sriminta Middey and Dr. Xiaoran Liu.

In addition to this, I would like to express my special gratitude to Dr. Rossitza Pentcheva and Okan Koksal who developed the computational machinery which helped us understand and interpret our experimental results.

My deepest gratitude goes to Dr. Jan Minár, for his invaluable contribution with the one-step theory calculations.

At the end, I would like to express gratitude towards family and friends for their immense support and encouragement throughout my doctoral studies.

To *Eliza, Reza and Afshin* for their unconditional love and support throughout my
graduate studies

TABLE OF CONTENTS

	Page
ABSTRACT.....	iii
ACKNOWLEDGMENTS.....	v
DEDICATION.....	vi
LIST OF FIGURES.....	x
LIST OF ABBREVIATIONS.....	xiv
CHAPTERS	
1.INTRODUCTION AND EXPERIMENTAL TECHNIQUES.....	1
1.1 Photoelectron Spectroscopy (PES).....	1
1.1.1 Basic concepts and experimental considerations.....	2
1.1.2 Angles-resolved photoelectron spectroscopy (ARPES).....	7
1.1.3 Bulk sensitivity vs. surface sensitivity.....	21
1.2 Kondo insulator (KI) material SmB ₆ , an introduction.....	24
1.2.1 Anderson model and the Kondo effect.....	25
1.2.2 Heavy-fermion metals and Kondo lattice.....	33
1.2.3 Kondo insulators.....	36
1.2.4 Spin excitons.....	37
1.2.5 Topological phases of Kondo insulators.....	40
References Cited in Chapter 1.....	42
2. INSTRUMENTATION AND EXPERIMENTAL PROCEDURE.....	49
2.1 Introduction.....	49

2.2 BESSY II synchrotron radiation source at the Helmholtz-Zentrum Berlin (Germany).....	51
2.3 Swiss Light Source at the Paul Scherrer Institute (Villigen, Switzerland).....	53
2.4 Diamond Light Source (Oxfordshire, United Kingdom).....	55
References Cited in Chapter 2.....	58
3. DATA ANALYSIS METHODS.....	59
3.1 Introduction.....	59
3.2 X-ray photoelectron spectroscopy (XPS) GUI in MATLAB.....	61
References Cited in Chapter 3.....	72
4. EFFECTS OF SPIN EXCITONS ON THE SURFACE STATES OF SmB ₆	73
4.1 Introduction.....	73
4.2 Experiment and results.....	76
4.3 Theory.....	82
4.4 Discussion.....	86
References Cited in Chapter 4.....	88
5. ELECTRONIC STRUCTURE OF A GRAPHENE-LIKE ARTIFICIAL CRYSTAL OF NdNiO ₃ (111).....	93
5.1 Introduction.....	93
5.2 Experimental results.....	97
5.2.1 Soft x-ray angle-resolved photoemission E _b -k _x measurements.....	98
5.2.2 Soft x-ray valence-band resonant photoemission measurement.....	102
5.2.3 Hard x-ray valence-band photoemission measurement.....	105
5.2.4 Soft x-ray angle-resolved Fermi-surface mapping.....	106

5.3 Conclusion.....	111
References Cited in Chapter 5.....	112
6. SUMMARY AND OUTLOOK.....	117
APPENDICES.....	121
A - ANALYSIS OF THE FOUR-DIMENSIONAL DFT DATA FOR ARPES INTERPRETATION.....	121
B - DIFFERENCE BETWEEN THE 1×1 AND $\sqrt{3}\times\sqrt{3}$ STRUCTURES FOR PEROVSKITES ALONG [111].....	123
C - AFM, XRD AND STEM MEASUREMENTS OF $\text{LaAlO}_3/\text{NdNiO}_3$ [111].....	124
D - ADDITIONAL ISOENERGETIC K_X - K_Y MAPS FOR NdNiO_3 [111] (THEORY).....	127
E - ADDITIONAL E_B - K_X MAPS FOR P1 AND P3 SYMMETRIES (THEORY).....	128
References Cited in Appendices.....	129

LIST OF FIGURES

PAGE

- 1.1 Schematic diagram describing the relationship between the energy levels in a solid and the distribution of the photoelectrons' kinetic energies in a PES experiment. w is the work function which is measured with respect to the Fermi Level. E_0 is the bottom of the valence band with respect to the Fermi Level and V_0 is the inner potential, and is measured with respect to the vacuum level ($V_0 = E_0 + w$).....3
- 1.2 Schematic diagram of a typical photoemission experiment. Incident photons liberate electrons from the sample in terms of photoelectrons. The liberated electrons are captured through an aperture in the optical column of a hemispherical electrostatic energy analyzer, measuring the kinetic-energy and momentum dispersion of the photoelectrons.....6
- 1.3 Components of the photoelectron momentum \mathbf{K} in vacuum in terms of the azimuth angle (φ) and the take-off-angle (ϑ).....8
- 1.4 Components of the photoelectron momentum \mathbf{K} in terms of the detector angle. (a) The case of tilt angle (β) of zero. (b) The case of non-zero tilt angle, introduced by rotating the sample along the x -axis and thus, resolving the y -component of the momentum \mathbf{K}_y9
- 1.5 Schematic graph illustrating the Bloch states in the nearly free electron picture. By neglecting the photon momentum, the extra momentum transfer between the initial and final Bloch states should be coming from the reciprocal lattice vectors, \mathbf{G}19
- 1.6 Inelastic mean free path of 41 different elements versus the kinetic energy of the electrons.....22
- 2.1 Schematic illustration of the BESSY II storage ring located in Berlin, Germany51
- 2.2 SX-ARPES endstation at the ADDRESS beamline of the SLS53
- 2.3 Schematic illustration of beamline I09 at the Diamond Light Source55
- 3.1 a) Data analysis and post-processing GUI designed in MATLAB. b) k-Path software for simulating the ARPES data using theoretical DFT calculations.....61
- 3.2 a) Au valence-band spectrum at room temperature and at photon energy of 6450 eV. b) Au valence band spectrum shown with dot black circles at room temperature and photon energy of 6450 eV. Fermi-Dirac distribution is also shown with the dashed red line at room temperature which doesn't fit to the VB spectra of Au at RT. The Gaussian function with a FWHM of 240 eV is also shown with the small red dashed line. Blue curve which fits the experimental data is the convolution between the Fermi-Dirac

distribution at RT and the Gaussian function of FWHM of 240 eV, hence the experimental resolution can be determined to be about 240 eV.....	62
3.3 Photoemission spectrum of the material $\text{LaAlO}_3\text{-NdNiO}_3$ [111] at photon energy of 6450 eV and thus probing the entire depth of the sample as evident from photoemission core levels from top layer (LaAlO_3) and the buried layer (NdNiO_3).....	64
3.4 Blue curve shows the angle integrated photoemission spectrum at 1.2 K. Red dashed line is the calculated Shirley background and the Black curve is the spectrum data after Shirley background removal.....	65
3.5 Photoemission spectrum of the material SmB_6 at 1.2 K (blue curve) and 20 K (red curve). Fermi Dirac functions convoluted with a Gaussian of FWHM of 3 meV is also shown. Difference between the F-D functions is shown with the black color curve. Difference between the F-D function multiplied by the experimental data is also shown with the color gray. At Fermi difference between black-color curve and gray-color curve will be minimum.....	66
3.6 Schematic illustration of linecut in momentum space for a normal emission geometry measurement at photon energy of 600eV and with analyzer's acceptance angle range of 20° for the material WP_2 . The linecut highlights the 14 th BZ in the extended-BZ scheme which covers three adjacent BZs.....	69
4.1 a) Cubic crystal structure of (SmB_6) b) Schematic graph of BZ with high symmetry points identified as Γ , X, M, R. The yellow plane highlights the plane probed by ARPES measurements at photon energy of 35 eV in the $k_x\text{-}k_y$ plane in momentum space.....	76
4.2 a) ARPES $k_x\text{-}k_y$ map at Fermi energy b) ARPES $E_b\text{-}k_x$ maps along the high symmetry direction $\bar{X} - \bar{\Gamma} - \bar{X}$ at two different sample's surface temperatures of 1.2 K and 20 K.....	77
4.3 The angle integrated valence-band photoemission spectra measured at the sample temperatures of 1.2 K (blue line) and 20 K (red line). The difference between the spectra at these two temperatures is shown in orange. To enhance the excursions, the difference spectrum has been multiplied by a factor of 10. The inset shows a close-up of the difference spectrum near the Fermi-energy. Spectra were measured along the $\bar{X} - \bar{\Gamma} - \bar{X}$ direction in the BZ and integrated over the entire angular range of the detector ($\sim 30^\circ$).....	78
4.4 The graph on top, shows the normalized PES spectrum at 1.2 K and the bottom graph shows the normalized PES spectrum at 20 K. Both spectra were first Shirley-background-subtracted and then normalized to unity to the area under the curve. Fermi velocity is calculated by taking the slope of the graphs at the Fermi level based on the Equation (4.2).....	81

4.5	The thermally activated temperature dependence of the imaginary part of the self-energy due to interactions with spin excitons, for electrons on the surface Fermi surface.....	84
4.6	The frequency dependence of the $T = 0$ self-energy.....	85
5.1	a) Schematic diagram of the $\text{LaAlO}_3/\text{NdNiO}_3$ heterostructure, grown along the $[111]$ direction b) High-resolution STEM cross sectional image of the sample and the corresponding schematics identifying atomic arrangements in the bilayer.....	97
5.2	a) Schematic diagram of the experimental geometry with all the relevant momentum vectors shown and labeled b) Momentum-resolved k_x - k_z map obtained by scanning the excitation photon energy. At the photon energy of 642 eV, the final photoelectron wave vector \mathbf{k}_f points close to a high-symmetry point along the k_z direction in the extended BZ picture.....	98
5.3	a) SX-APRES spectrum of the valence-band dispersion measured along the $K'-\Gamma$ -K high-symmetry direction. The white EDC curve represents the momentum-integrated MEW-DOS, with most prominent features A-D labeled. b) The DFT+U calculation of the spin-projected band structure for the AFM P1 (1×1) configuration shown for the same cut of the BZ. c) Momentum distribution curves recorded at the binding energies of the features A, B, C and D.....	100
5.4	SX-APRES spectrum of the valence-band dispersion measured along the $K'-\Gamma$ -K high-symmetry direction at photon energy of 642 eV. Spectrum can be normalized by the binding-energy-averaged and the k -averaged spectra to enhance the dispersive features.....	101
5.5	a) Angle-integrated VB spectra recorded at the photon energies of 868.5 eV (off resonance) and 873.4 eV (on resonance) reveal the contribution of the Ni $3d$ states via resonant enhancement. Inset shows the Ni L_2 XAS spectrum with the blue and red markers at the relevant photon energies. b) The difference spectrum obtained by subtracting the ‘off’ spectrum shown in panel (a) from the ‘on’ spectrum. Two distinct components A and B, corresponding to the NdNiO_3 -derived Ni $3d$ states, are fitted using two Gaussian peaks centered at -1.1 and -2.2 eV. c) Bulk-sensitive HAXPES spectrum recorded at the photon energy of 6.45 keV with the IMFP of approximately 85 Å. Inset shows a high-statistics spectrum of the valence-band maximum (at -265 meV), referenced to the Au Fermi edge. d) Cross-section weighted element-projected and total DOS of the superlattice, calculated in the GGA+ U framework of DFT, and broadened by convolution with Gaussian and Lorentzian functions to account for both experimental and hole-lifetime broadening.....	103

5.6 Momentum-resolved XPD-corrected SX-ARPES photoemission intensity map of the Ni 3 <i>d</i> states near the valence-band maximum (feature A, centered at -1.6 eV below E_F).....	106
5.7 a) Non-normalized momentum-resolved photoemission intensity map of the VB feature A, containing combined contributions from the Ni 3 <i>d</i> dispersive states and the XPD intensity modulations. The central intensity peak appears shifted toward the [111] emission direction due to a significant XPD contribution to the spectrum. b) Non-normalized photoemission intensity map of the VB feature B comprised of flat XPD-like bands. The central intensity peak appears exactly along the [111] emission direction, confirming an overwhelming fraction of the XPD-derived intensity in the spectrum.....	107
5.8 a) Perovskite structure along conventional [001] direction on the left and along [111] direction in the middle are shown; right panel shows the hexagonal Brillouin Zone of the [111] structure. b) Isoenergetic cuts through the band structure in reciprocal space for the majority (top row) and minority (bottom row) bands, calculated for the binding-energy range from -0.5 eV to -1.6 eV, and spanning the major Ni 3 <i>d</i> features near the VB maximum.....	108
5.9 One step theory calculation of the momentum-resolved SX-ARPES spectra showing Ni 3 <i>d</i> states near the Fermi level. Calculations were carried out using experimental SX-ARPES geometry for the photon energy of 642 eV. Clear modulations of the intensities between adjacent BZs due to the strong matrix-element effects are observed, consistent with the experimental observations.....	109
A.1 Schematic diagram identifying the global coordinate system and the axes of rotations along the x, y and z directions.....	122
B.1 Schematic diagrams of perovskite structures along [001] and [111] pseudocubic directions.....	123
C.1 a) AFM image revealing surface morphology b) RHEED image recorded during the growth confirming atomic layer-by layer growth of each unit cell along [111] direction.....	124
C.2 HAADF-STEM image shown in (a) and intensity scan along a long column, indicated in the magnified HAADF-STEM image (b) and plotted in (c).....	125
C.3 XRD measurement to probe the crystal structure.....	125
D.1 Additional isoenergetic cuts through the band structure in reciprocal space for the majority (top row) and minority (bottom row) bands.....	127
E.1 Additional E_b-k_x band-structure calculations for P1 and P3 symmetry.....	128

LIST OF ABBREVIATIONS

1. Angle-Resolved Photoelectron Spectroscopy (ARPES)
2. Hard X-ray Photoelectron Spectroscopy (HAXPES)
3. X-ray Absorption Spectroscopy (XAS)
4. Samarium Hexaboride (SmB_6)
5. Unit Cell (u.c.)
6. Transition Metal Oxides (TMO)
7. Photoelectron Spectroscopy (PES)
8. Kinetic Energy (KE)
9. Binding-Energy (BE)
10. Density of States (DOS)
11. Valence-Band (VB)
12. Fermi Level (FL)
13. Full-Width Half-Maximum (FWHM)
14. X-ray Photoelectron Spectroscopy (XPS)
15. Electron Spectroscopy for Chemical Analysis (ESCA)
16. Synchrotron Radiation (SR)
17. Charge Coupled-Device (CCD)
18. Ultrahigh-Vacuum (UHV)
19. Room Temperature (RT)
20. Take-Off-Angle (TOA)
21. Swiss Light Source (SLS)
22. Diamond Light Source (DLS)
23. Brillouin Zone (BZ)
24. Inelastic Mean-Free Path (IMFP)
25. Kondo Insulator (KI)
26. Topological Kondo Insulator (TKI)
27. Antiferromagnetism (AFM)
28. Ferromagnetism (FM)
29. Anderson Single Impurity Model (ASIM)
30. Ruderman–Kittel–Kasuya–Yosida (RKKY)
31. Quantum Critical Point (QCP)
32. Topological Insulator (TI)
33. Paul Scherrer Institute (PSI)
34. Resonant Inelastic X-ray Scattering (RIXS)
35. Near-Edge X-ray Absorption Fine Structure (NEXAFS)
36. X-ray Standing Wave (XSW)
37. X-ray Photoelectron Diffraction (XPD)
38. Graphical User Interface (GUI)
39. Density Functional Theory (DFT)
40. Matrix-Element Weighted Density of States (MEW-DOS)
41. Energy Distribution Curve (EDC)
42. Momentum Distribution Curve (MDC)
43. Scanning Transmission Electron Microscopy (STEM)
44. Spin-Orbit Coupling (SOC)

45. X-ray Linear Dichroism (XLD)
46. Reflection High-Energy Electron Diffraction (RHEED)
47. High-Angle Angular Dark Field (HAADF)
48. X-ray Diffraction (XRD)

CHAPTER 1

INTRODUCTION AND EXPERIMENTAL TECHNIQUES

1.1 Photoelectron spectroscopy (PES)

The photoemission process, generally known as the *photoelectric effect*, was first demonstrated by Hertz and Hallwachs in 1887 and 1888 [1, 2]. In these early experiments, incident monochromatic light (in the ultraviolet region of the electromagnetic spectrum) was focused onto the surfaces of potassium or sodium metals. As a result, electrons from the surface of the material were ejected into vacuum (the ejected electrons are commonly referred to as photoelectrons). Kinetic energies (KE) of the liberated electrons were determined by an external stopping-potential barrier mounted within the vacuum chamber. The magnitude of the measured photoelectron current was found to be proportional to the intensity of the incident light beam, while the photoelectrons' cut-off energy was found to be dependent on the frequency of the incident light. Later, this phenomenon was explained by Albert Einstein in 1905 [3], introducing quantized nature of light (photons), with the energy of a single photon given by:

$$E = h\nu \quad (1.1)$$

Here h is the Planck constant ($h = 4.135 \times 10^{-34} \text{ eV}\cdot\text{s}$) and ν is the frequency of the incident light. Energy of the photoelectrons could be calculated using one of the fundamental laws of physics, *the law of conservation of energy*. Thus, the kinetic energy of the most energetic photoelectron will be equal to the energy of the incident photon minus the material's *work function* (w), which is a measure of the potential barrier at the surface

of the sample, preventing the valence electrons from escaping the sample due to the screening effects at the surface after the electron removal:

$$KE_{max} = h\nu - w \quad (1.2)$$

The same principle could be adopted for less energetic photoelectrons (*i.e.* bound electrons) by subtracting the binding-energy (BE) of these bound electrons from the right side of Equation (1.2), yielding a general equation for the photoelectrons' kinetic energy:

$$KE = h\nu - w - BE \quad (1.3)$$

Thus, in a photoemission experiment, the binding energies of electrons in a material could be determined by measuring their kinetic energies at the detector.

1.1.1 Basic concepts and experimental considerations

In the previous section we described the photoemission process as a basic photoelectric effect. Here, we will try to give additional explanation regarding the photoemission process and what can be learned by performing PES measurements, along with some basic experimental considerations in a typical PES experiment. Schematic diagram in Figure (1.1), explains the relationship between the energy levels in a solid and the distribution of the photoelectrons' kinetic energies in a PES experiment, which effectively maps the cross-section-weighted density of states (DOS) of the sample's electronic structure. Materials have specific core levels (at unique binding energies) and a valence-band (VB), corresponding to the DOS of the nearly-itinerant electrons up to the Fermi level (FL). It should be noted that Figure (1.1) presents a simplified picture of the real photoemission process, however, it is instrumental in demonstrating the key processes

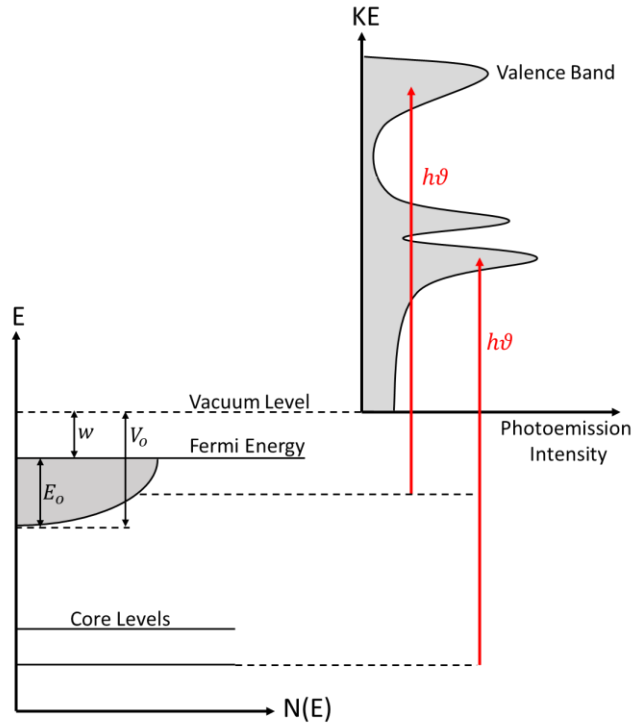


Figure (1.1) – Schematic diagram describing the relationship between the energy levels in a solid and the distribution of the photoelectrons' kinetic energies in a PES experiment. w is the work function which is measured with respect to the Fermi Level. E_0 is the bottom of the valence band with respect to the Fermi Level and V_0 is the inner potential, and is measured with respect to the vacuum level ($V_0 = E_0 + w$).

and concepts involved. Firstly, the photoemission process can only occur for the electrons in the filled, or occupied, states, *i.e.* a photoemission process does not facilitate direct information about the unoccupied states. Secondly, as could be seen in Figure (1.1), each peak in the PES spectrum exhibits a measurable background intensity on the higher-binding-energy side.

In a real experiment, photoexcited electrons will scatter inelastically within the sample (from ions, impurities, and other electrons) and result in a continuum of secondary electrons with lower kinetic energies, which will manifest itself as an inelastic background in the photoemission spectrum [4-6]. Various background subtraction methods, such as the Shirley background subtraction [5], are commonly used to remove such background for facile peak fitting and data analysis.

Finally, as can be seen in Figure (1.1), for core levels, which are expected to have sharp and unique binding energies, the photoemission spectrum will have a specific bandwidth in energy (*i.e.* peak broadening), which is a characteristic of the spectroscopic technique (in this case PES). Several factors contribute to the observed peak broadening in a photoemission experiment. First, the peak broadening is partly due to the limited combined energy resolution of the source and the analyzer. This effect could be modeled by convolving the function that describes the shape of a given peak with a Gaussian lineshape with a specific full-width half-maximum (FWHM) corresponding to the total experimental resolution. Another important factor is the natural lifetime broadening of the PES spectrum according to the uncertainty principle, which results in a Lorentzian lineshape [7-9]. Another factor is the thermal broadening of the core-level peaks, which results in a Gaussian line shape [10, 11]. To account for all these effects, Voigt functions, which are convolutions of a Lorentzian function and a Gaussian function, are often used to fit the photoemission spectral lines.

In general, the spectral lineshape obtained through a real PES experiment could be much more complicated than the one shown in Figure (1.1). Specifically, the many-body electron correlations and the photoelectron-photohole effects will lead to more complicated line shapes, including asymmetries, peak splitting and satellites. Some of these complications arise from the photoemission process itself, which is a complicated many-body phenomenon, which affects the final lineshapes in a typical PES measurement [12-14].

Discussion of these effects is beyond the scope of this thesis; however, it is important to mention that a wealth of information can be extracted from the analysis of the shapes

and positions of the core levels along the energy scale. For example, as we know, binding energies of the core-level electrons in a material depend on the chemical environment surrounding the respective atoms [13]. Thus, by carrying out core-level photoemission measurements one could detect and identify the chemical states of the constituent ions in the material under investigation. Because of this immediate analytical applicability, the original name of the technique, which is now commonly referred to as x-ray photoelectron spectroscopy (XPS), was *electron spectroscopy for chemical analysis* (ESCA) [15]. Detailed reviews of the historical developments in the field of photoemission spectroscopy are provided in references [16, 17].

Figure (1.2), shows a schematic diagram of the experimental geometry for a typical photoemission experiment. The photon source could be a gas-discharge lamp, a laser, an x-ray tube, or a synchrotron radiation (SR) beamline. In this thesis, we utilized synchrotron radiation for all our photoemission experiments. In Chapter 2, we will discuss in detail the properties of the light produced by a synchrotron source, as well as all the relevant experimental considerations and advantages, compared to conventional lab-based sources.

Photoelectrons ejected from the sample during the photoemission process are analyzed for their kinetic energy by means of an electrostatic photoelectron energy analyzer. For crystalline samples, the ejected photoelectrons escape from the surface of the materials at different angles, depending on their momenta. With the recent advances in two-dimensional imaging detectors utilizing charge coupled-device (CCD) cameras, it is possible to record a kinetic-energy photoemission spectrum along a particular emission direction (linecut) in the momentum space. Thus, modern-day electrostatic analyzers are

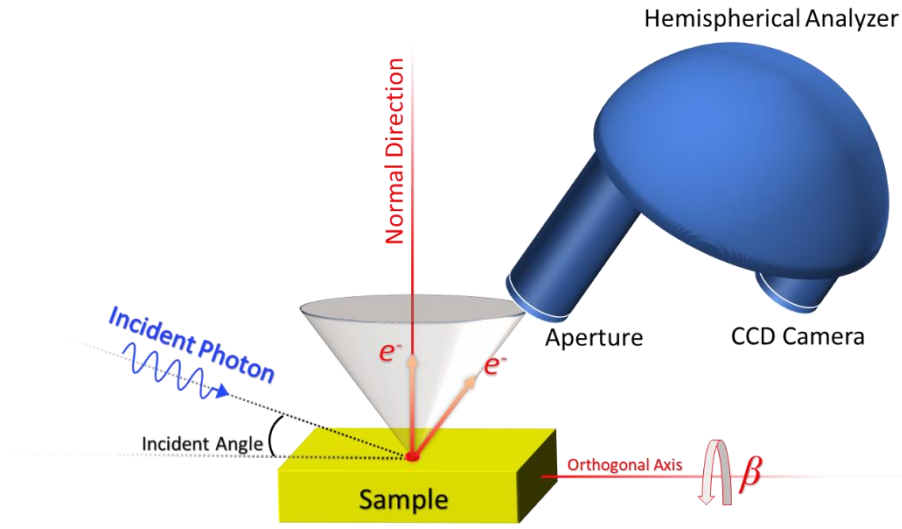


Figure (1.2) – Schematic diagram of a typical photoemission experiment. Incident photons liberate electrons from the sample in terms of photoelectrons. The liberated electrons are captured through an aperture in the optical column of a hemispherical electrostatic energy analyzer, measuring the kinetic-energy and momentum dispersion of the photoelectrons.

capable of resolving not only the photoelectron kinetic energies, but also their final photoelectron momenta [18].

Another important technical consideration in any photoemission experiment is the fact that, in the presence of contamination in the analysis chamber or at the surfaces of the sample, the photoemitted electrons could be easily absorbed, scattered and deflected by all atoms and molecules in their path. Thus, photoemission experiments must be done in ultrahigh-vacuum (UHV) conditions (10^{-9} - 10^{-11} torr), in order to prevent interference with the adsorbed atoms/molecules at the surface of the material under investigation, as well as scattering by gaseous molecules between the sample and the detector. Adsorption of these gaseous molecules at the surface of the sample and the formation of a contaminant layer also presents a great technical challenge. For example, it takes only half-an-hour to form one monolayer of CO adsorbate at the surface of a solid at room temperature (RT) and 10^{-9} torr pressure (assuming a sticking coefficient of one, which means every molecule

impinging on the surface of the material sticks). Thus, at the pressures on order of 10^{-11} torr, surface-sensitive experiments can be carried out for longer amounts of time, without seeing the effects of contamination at the sample surface [19].

1.1.2 Angle-resolved photoelectron spectroscopy (ARPES)

As was described in the previous section, by performing angle-resolved photoelectron spectroscopy measurements, one can map the photoelectron kinetic energies (and thus their binding energies through Equation (1.3)) versus the photoelectron momentum \mathbf{K} in vacuum. As shown in Figure (1.3), from geometric considerations, we can write down the components of the photoelectron momentum \mathbf{K} in vacuum in terms of the emission angles as follows:

$$|\mathbf{K}_x| = |\mathbf{K}| \sin(\vartheta) \cos(\varphi) \quad 1.4 \text{ a)}$$

$$|\mathbf{K}_y| = |\mathbf{K}| \sin(\vartheta) \sin(\varphi) \quad (1.4 \text{ b)}$$

$$|\mathbf{K}_z| = |\mathbf{K}| \cos(\vartheta) \quad (1.4 \text{ c)}$$

The photoelectron momentum \mathbf{K} could be derived from the free-electron momentum dispersion equation (since photoelectrons are in vacuum, their dispersion relations should be parabolic):

$$|\mathbf{K}| = \sqrt{\frac{2mE_{kin}}{\hbar^2}} \approx 0.5124 \sqrt{E_{kin}(eV)} [\text{\AA}^{-1}] \quad (1.5)$$

Here m is the mass of the electron at rest and E_{kin} is the kinetic energy of the photoelectron in eV.

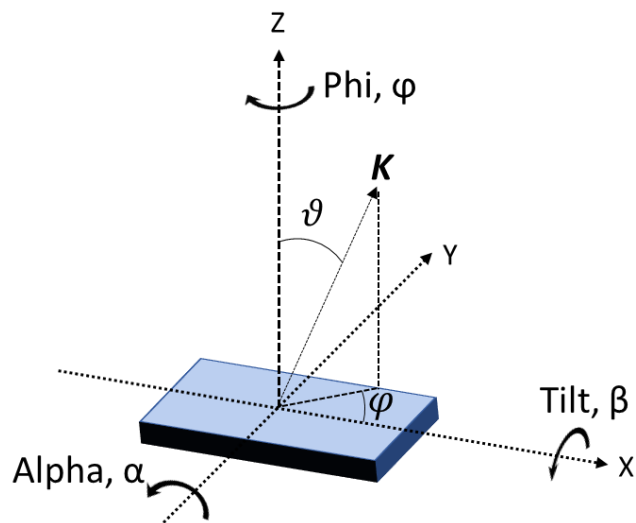


Figure (1.3) – Components of the photoelectron momentum \mathbf{K} in vacuum in terms of the azimuth angle (φ) and the take-off-angle (ϑ).

It is instructive to check whether the photoemission measurements carried out at typical photon energies require a relativistic correction. For example, let us consider photoelectrons with energies on the order of 5000 eV, which is in the hard x-ray regime. From the relativistic energy equation, it is trivial to calculate that the speed of photoelectrons at this energy will be about seven times smaller than the speed of light. Hence, in this case, we are safe treating the photoemission measurements in the non-relativistic limit. Finally, as an example of a typical value of the final photoelectron momentum $|\mathbf{K}|$, for a photoelectron with kinetic energy of 1000 eV, its momentum will be approximately 16.2 \AA^{-1} .

Here, we will consider a limiting case of the, so called, normal-emission measurements, wherein the sample's normal is aligned along the direction of the analyzer aperture, and thus the analyzer captures the electrons that are emitted along the direction normal to the sample's surface as shown in Figure (1.4 a). We will furthermore restrict the azimuthal angle of the sample to the value of zero $\varphi = 0$. For the photoelectrons that are

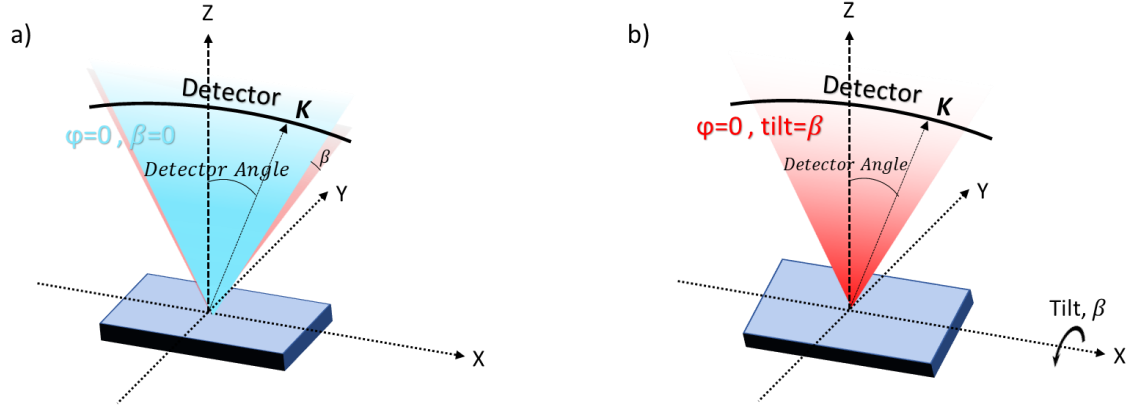


Figure (1.4) – Components of the photoelectron momentum \mathbf{K} in terms of the detector angle. (a) The case of tilt angle (β) of zero. (b) The case of non-zero tilt angle, introduced by rotating the sample along the x -axis and thus, resolving the y -component of the momentum \mathbf{K}_y .

emitted in this “normal plane” (*i.e.* the plane at $\varphi = 0$ and normal to the sample’s surface), the final photoelectron momentum components in vacuum could be written as:

$$|\mathbf{K}_x| = |\mathbf{K}| \sin(\theta_{TOA}) \quad (1.6 \text{ a})$$

$$|\mathbf{K}_y| = 0 \quad (1.6 \text{ b})$$

$$|\mathbf{K}_z| = |\mathbf{K}| \cos(\theta_{TOA}) \quad (1.6 \text{ c})$$

where θ_{TOA} is the take-off-angle (TOA). If one rotates the sample along the orthogonal axis (through angle β), the analyzer will capture the photoelectrons that are emitted in planes other than the *normal plane*, as shown in Figure (1.4 b). By doing so, one could resolve the y -component of the photoelectron momentum \mathbf{K}_y in addition to the x -component of the momentum \mathbf{K}_x . Thus, the photoelectron momentum components in this case could be expressed as follows:

$$|\mathbf{K}_x| = |\mathbf{K}| \sin(\theta_{TOA}) \quad (1.7 \text{ a})$$

$$|\mathbf{K}_y| = |\mathbf{K}| \cos(\theta_{TOA}) \sin(\beta) \quad (1.7 \text{ b})$$

$$|\mathbf{K}_z| = |\mathbf{K}| \cos(\theta_{TOA}) \quad (1.7 \text{ c})$$

In a typical ARPES experiment, angle β is usually called the ‘tilt angle’. In a more general case, the detector could be positioned along a direction other than the normal direction, but still in the normal plane ($\varphi = 0, \beta = 0$). Such common experimental configuration could be achieved by either rotating the sample through angle (α), as shown in Figure (1.3), or by rotating the detector (a less common and more technically-challenging approach). In this case, the analyzer will capture photoelectrons that are emitted away from the normal emission direction, and thus the components of the photoelectron momentum could be expressed as follows:

$$|\mathbf{K}_x| = |\mathbf{K}| \sin(\theta_{TOA} + \alpha) \quad (1.8 \text{ a})$$

$$|\mathbf{K}_y| = |\mathbf{K}| \cos(\theta_{TOA} + \alpha) \sin(\beta) \quad (1.8 \text{ b})$$

$$|\mathbf{K}_z| = |\mathbf{K}| \cos(\theta_{TOA} + \alpha) \quad (1.8 \text{ c})$$

For non-crystalline samples, wherein coordinates x , y and z are not tied to the crystallographic axes of the sample, the azimuthal angle φ is arbitrary and could thus be set to zero.

Various ARPES instruments and systems have different experimental configurations in terms of the orientation and position of the detector with respect to the sample normal and the incident light beam. As we will see in Chapter 2, at the ADDRESS beamline of the Swiss Light Source (SLS), the so called ‘in-between angle’ between the incident x-ray beam and the detector is fixed at 70° , while at the beamline I09 of the Diamond Light Source (DLS) this angle is set to 87° .

Up to this point we have discussed the final photoelectron momentum in vacuum. Now the question is, how can we relate the above-mentioned final photoelectron momentum to the single-electron momentum inside the sample? From now on we will

write down the momentum of a single electron inside the sample using the smaller-case letter k , while for the photoelectrons in vacuum the momentum will be written using upper-case K , as in the previous section.

In the early descriptions of the photoemission process, it was thought that the photoemission signal originates exclusively from the surface of a metallic sample. In this framework, proposed by Sommerfeld [20], the conduction electrons in the bulk of such a sample are free to move (free-electron gas) and thus cannot absorb photons due to the laws of conservation of energy and momentum. Therefore, it was thought that the photoemission signal cannot originate from the bulk, but rather must emanate from the surface of the sample, where the potential difference between the sample and the vacuum creates a surface potential. Of course, Sommerfeld's free-electron model was a crude approximation for describing the electronic behavior in a crystalline metal, where the electrons, in fact, move in a periodic potential. The first theory of bulk photoemission which, considered the periodic nature of a crystal, was proposed by Fan in 1945 [21] and was described within the more accurate 'nearly free-electron' picture. To date, a comprehensive explanation of the photoelectric process as a many-body process is still under investigation due to its complexity.

In 1964, Berglund and Spicer [22] proposed a model, which is now widely-known as the *three-step model*. In this model, the photoemission process is separated into three independent steps. First, a photon absorption event excites an electron Bloch state from the initial state into the excited state. Then, the excited electron travels to the surface of the material. During this process, an electron can be scattered both elastically and inelastically

In the three-step model we will consider only the elastically-scattered electrons. Finally, the electron overcomes the potential barrier at the surface and escapes into the vacuum.

Although it is well-understood that the actual photoemission process is more complex, the three-step model provides a very useful formalism for both fundamental and practical applications. It is important to mention that a more quantum-mechanically-accurate *one-step model* was proposed by Pendry in 1976 [23]. However, an in-depth discussion of this model is beyond the scope of this thesis [24, 25].

In the photoemission process, the initial state is an N -electron system wave-function and the final state consists of the wave-function of the resultant $N-1$ electron system and the plane-wave function describing the propagation of a free electron in vacuum. In terms of the probability amplitude, the optical excitation can be approximated to the first order of perturbation by the Fermi's Golden Rule as follows [26]:

$$p_{fi} = \frac{2\pi}{\hbar} |\langle \psi_f^N | H_{int} | \psi_i^N \rangle|^2 \delta(E_f^N - E_i^N - hf) \quad (1.9)$$

The interaction Hamiltonian can be simplified using the dipole approximation (if the vector potential \mathbf{A} is constant over the atomic dimensions, which is usually true in the ultraviolet regime, where we have $\nabla \cdot \mathbf{A} = \mathbf{0}$ and $\mathbf{A} \approx \mathbf{A}_0$), with an optional gauge where the electric potential φ is zero. As a result, we can write:

$$H_{int} = \frac{e}{mc} \mathbf{A}_0 \cdot \mathbf{p} \quad (1.10)$$

As can be seen from the Fermi's Golden Rule in Equation (1.9), there should be an overlap between the amplitude of the initial and final states for a non-zero optical transition. We can further simplify the interaction amplitude using the Hartree-Fock approximation [27] as follows: for the initial wave-function (ψ_i^N), we can write down the wave-function as the product of the one-electron orbital, ϕ_i^k , and an $(N-1)$ -electron wave-function (ψ_i^{N-1}):

$$\psi_i^N \sim \phi_i^k \psi_i^{N-1} \quad (1.11)$$

Here, it is important to note that ψ_i^{N-1} is not an eigenstate of the $N-1$ electron Hamiltonian. Rather, it is just what remains of the N -electron wave-function after considering the one-electron orbital contribution to the wave-function.

As for the final wave-function (ψ_f^N), we could express it as the product of the wave-function for an $N-1$ electron system (eigenstate of the Hamiltonian of an $N-1$ electron system), ψ_f^{N-1} , and the wave-function for a propagating photoelectron, ϕ_f^k :

$$\psi_f^N \sim \phi_f^k \psi_f^{N-1} \quad (1.12)$$

It should be noted that ψ_f^{N-1} might be very different from ψ_i^{N-1} , since ψ_f^{N-1} is the wave-function for a system of $N-1$ electrons, and the absence of an electron can change the effective potential in the system and hence the electronic wave-function.

It should also be noted that all the steps mentioned above are assumed to happen in the limit of the *sudden approximation*, wherein we discard the relaxation of the system during the photoemission process. In other words, the photoemission process (in the three-step model) will happen so fast that the $N-1$ electron system will have no time to interact with the excited photoelectron. The sudden approximation is sensible for the experiments carried out at high kinetic energies but starts to break-down for low-kinetic-energy experiments, wherein the response of the system should be considered during the photoemission process.

In summary, in the sudden approximation limit, we can express the interaction term for the optical excitation amplitude as follows:

$$|\langle \psi_f^N | H_{int} | \psi_i^N \rangle|^2 \sim |\langle \phi_f^k | H_{int} | \phi_i^k \rangle|^2 |\langle \psi_f^{N-1} | \psi_i^{N-1} \rangle|^2 \quad (1.13)$$

The first term on the right-hand side of Equation (1.13) is the one-electron dipole matrix element which imposes some basic rules on the photoemission intensities and distributions based on the symmetries of the electronic wave-functions and the interaction term [28].

For the second term on the right-hand side of the Equation (1.13), we could argue that for a non-interacting electron system, it does not matter whether we *first* remove an electron from the N -electron system and *then* write down the wave function for the $N-1$ electron system, or if we decompose the initial N -electron wave function based on the Hartree-Fock approximation and then write the $N-1$ electron function; in both cases the final and the initial wave functions will be identical, and this term will be equal to a Dirac delta function.

Since the total photoemission intensity is the sum of all the possible transitions between the initial and the final states, the ARPES spectra in a non-interacting limit consist only of the Dirac delta functions at the Hartree-Fock orbital energies for the states with non-zero dipole matrix elements. For an interacting electron system, the amplitude of the second term on the right-hand side of the Equation (1.13) is, in general, not-zero; and thus, the ARPES spectra will contain the many-body effects as well.

In many-body physics for correlated electron systems, one of the most common approaches is to use the Green's functions, wherein the response of a system could be investigated by adding or removing an electron from the system by means of *greater* (one-electron addition) or *lesser* (one-electron removal) Green's functions.

It could be shown that the retarded Green's function for a system can be written as (Lehmann Representation):

$$G^\pm(\mathbf{k}, \omega) = \sum_m \frac{|\langle \psi_m^{N\pm 1} | c_{\mathbf{k}\sigma}^\pm | \psi_i^N \rangle|^2}{\omega - E_m^{N\pm 1} + E_i^N \pm i\zeta} \quad (1.14)$$

where the operator $c_{\mathbf{k}}^\pm$, creates or annihilates an electron with energy ω , momentum \mathbf{k} , and spin σ in the N -electron system initial wave-function ψ_i^N . Here, ζ is a positive infinitesimal constant that can be eliminated by taking the limit of the Equation (1.14) as ζ approaches zero at the end of the calculation.

The spectral function $A(\mathbf{k}, \omega) = A^+(\mathbf{k}, \omega) + A^-(\mathbf{k}, \omega)$ is defined as the imaginary part of the Green's function and has an important meaning in the context of spectroscopy.

$$A^\pm(\mathbf{k}, \omega) = -\frac{1}{\pi} \text{Im}(G^\pm(\mathbf{k}, \omega)) = \sum_m |\langle \psi_m^{N\pm 1} | c_{\mathbf{k}\sigma}^\pm | \psi_i^N \rangle|^2 \delta(\omega - E_m^{N\pm 1} + E_i^N) \quad (1.15)$$

As can be seen from Equation (1.15), this is nothing but the second term in the right-hand side of Equation (1.13) modified by discarding the one-electron dipole matrix term and considering all the possible transitions between the initial and the final states.

Thus, we can assert that, based on the definition of Green's function and spectral function in many-body physics, the photoemission intensity is directly proportional to the spectral function (hence the name 'spectral function', since it can be measured via spectroscopic techniques).

As mentioned above, the spectral function is composed of two parts: one-electron *removal* and one-electron *addition* ($A^-(\mathbf{k}, \omega), A^+(\mathbf{k}, \omega)$). In a PES measurement we measure the one-electron *removal* part of the spectral function, and hence a complete experimental determination of the spectral function requires complementary methods to measure the one-electron *addition* contribution (for example, inverse photoemission spectroscopy). The lack of information regarding the other part of the spectral function is sometimes approximated by assuming electron-hole symmetry close to the FL [29].

Below, we briefly describe the basic properties of the many-body Green's functions. It is easy to show that the Green's function for the non-interacting electron system can be written as:

$$G^0(\mathbf{k}, t) = -i\theta(t)e^{-i\epsilon(\mathbf{k})t} \rightarrow G^0(\mathbf{k}, \omega) = \frac{1}{\omega - \epsilon(\mathbf{k}) + i\zeta} \rightarrow A^0(\mathbf{k}, \omega) = \delta(\omega - \epsilon(\mathbf{k})) \quad (1.16)$$

where $\epsilon(\mathbf{k})$ is the single-particle energy-momentum dispersion. As a result, spectral function for a non-interacting electron system will be a Dirac delta function. This is not surprising, since the removal or addition of an electron from/to a non-interacting electron system can only occur when the energy (ω) is equal to the single-particle electron energy-momentum dispersion.

When we modify the original Green's function $G^0(\mathbf{k}, t)$ to include the decay term due to the scattering processes, it becomes

$$G^{modified}(\mathbf{k}, t) = -i\theta(t)e^{-i\epsilon(\mathbf{k})t}e^{-\frac{t}{\tau}} \rightarrow G^{modified}(\mathbf{k}, \omega) = \frac{1}{\omega - \epsilon(\mathbf{k}) + \frac{i}{\tau} + i\zeta}$$

$$\rightarrow A^{modified}(\mathbf{k}, \omega) = -\frac{1}{\pi} \frac{\frac{1}{\tau}}{(\omega - \epsilon(\mathbf{k}))^2 + (\frac{1}{\tau})^2} \quad (1.17)$$

As can be seen from Equation (1.17), the Lorentzian spectral function corresponds to a particle with a well-defined energy $\epsilon(\mathbf{k})$, which defines the center of the peak with a finite width given by lifetime τ . Since the electron is interacting with other particles in this picture, it can exchange momentum with other electrons, and hence the state \mathbf{k} can be changed to a different state with a lifetime τ . As a result, in its simplest form, the correlated electron system can be described based on the concept of *quasiparticles* with specific lifetimes.

For a general case, which includes all the interaction terms in a system, the spectral function can be written as follows (this is the general form of the Equation (1.17)):

$$G(\mathbf{k}, \omega) = \frac{1}{\omega - \epsilon(\mathbf{k}) - \Sigma(\mathbf{k}, \omega) + i\zeta} \quad (1.18)$$

wherein $\Sigma(\mathbf{k}, \omega)$ is the one-electron self-energy composed of the real part and the imaginary parts ($\Sigma(\mathbf{k}, \omega) = \Sigma'(\mathbf{k}, \omega) + i \Sigma''(\mathbf{k}, \omega)$). The real and the imaginary parts of the self-energy contain all the information regarding the energy renormalization and the lifetime of an electron with energy $\epsilon(\mathbf{k})$ and momentum \mathbf{k} , propagating in a many-body system, as well as its effects on the electronic structure.

Based on the definition above, the explicit form of the spectral function in terms of the electron self-energy can be obtained as follows:

$$A(\mathbf{k}, \omega) = -\frac{1}{\pi} \text{Im}(G(\mathbf{k}, \omega)) = -\frac{1}{\pi} \frac{1}{\Sigma''(\mathbf{k}, \omega)} \frac{1}{1 + \left(\frac{\omega - \epsilon(\mathbf{k}) - \Sigma'(\mathbf{k}, \omega)}{\Sigma''(\mathbf{k}, \omega)} \right)^2} \quad (1.19)$$

Again, as can be seen from Equation (1.19), its general shape is a Lorentzian peak whose maximum is at $\epsilon(\mathbf{k}) + \Sigma'(\mathbf{k}, \omega)$, with a half-width of $\Sigma''(\mathbf{k}, \omega)$ and a height of $\frac{1}{\Sigma''(\mathbf{k}, \omega)}$.

Full description of the electron self-energy for a many-body system is an intricate problem, which requires the use of Feynman diagram perturbation theory and, in general, is unknown [30]. However, we can see that the real part of the self-energy changes the binding-energy of the electrons and the imaginary part increases the peak width and lowers its height. As a result, PES measurements can give us direct information on the behavior of the self-energy in a many-body system, and thus a wealth of information can be learned about the behavior of such systems by looking at their PES spectra.

In derivations of the formulas on the pages 12-17 we used references [27, 31, 32].

As an example of this, in Chapter 4, we describe our PES measurements of single-crystalline samarium hexaboride (SmB_6), wherein we argue that our results of high-resolution PES valence-band measurements possibly explain the controversial resistivity plateau, seen at temperatures much below the expected coherence temperature corresponding to the Fermi-liquid theory.

We conclude our theoretical overview on the photoemission process by going back to the original question of how to relate \mathbf{K} , photoelectrons momentum in vacuum, to the electron's momentum \mathbf{k} inside the sample. As we know, the momentum and energy conservation laws should hold for the incident photon and the N -electron system as whole:

$$E_f^N - E_i^N = h\nu \quad (1.20 \text{ a})$$

$$\mathbf{k}_f^N - \mathbf{k}_i^N = \mathbf{k}_{h\nu} \quad (1.20 \text{ b})$$

The photon momentum can be written simply as $|\mathbf{K}_{h\nu}| \left[\frac{1}{\text{\AA}} \right] = 0.506 E[\text{keV}]$, where the energy of the photon is in kilo-electron volts. For example, for photons with the energy of 100 eV, the photon momentum will be approximately 0.05 \AA^{-1} , which is much smaller than the typical Brillouin zone (BZ) dimensions of $2\pi/a$ in a solid (a is the lattice constant). As a result, for the conventional ARPES experiments at low photon energies, the contribution from the photon momentum can be neglected.

Now, let us consider the electronic band-structure for a solid in the nearly free-electron picture, wherein interaction among the electrons is treated as a perturbation to the free-electron gas on the lattice. The effects of interaction between the electrons in this model will be large only at the boundaries of the BZ, based on the perturbation theory. As

Figure (1.5) – Schematic graph illustrating the Bloch states in the nearly-free electron picture. By neglecting the photon momentum, the extra momentum transfer between the initial and final Bloch states should be coming from the reciprocal lattice vectors, \mathbf{G} .

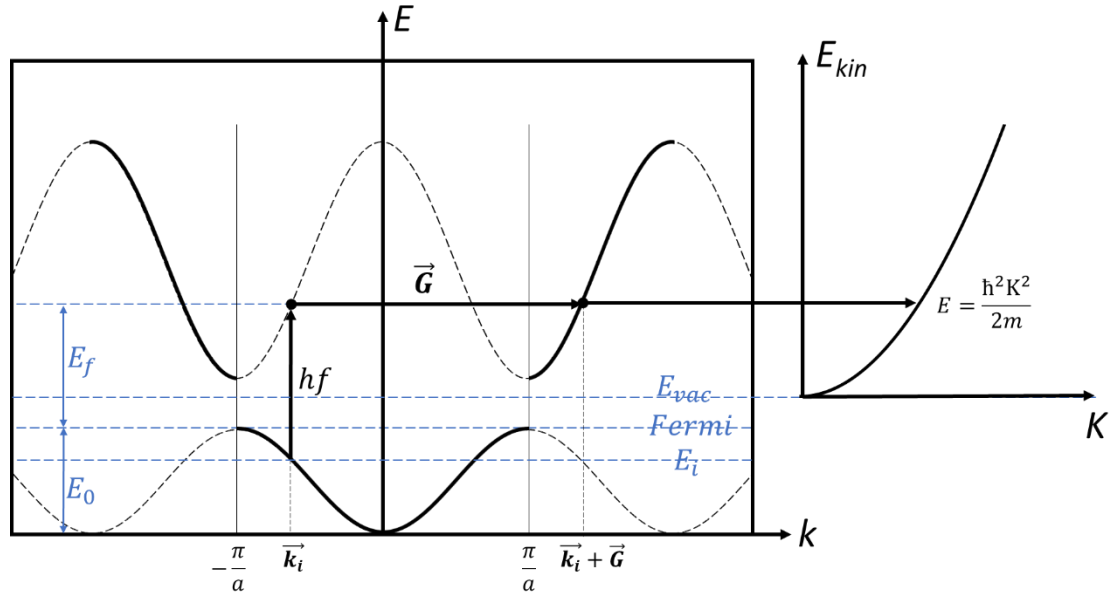


Figure (1.5) – Schematic graph shows the bands in a nearly free electron model. By neglecting photon momentum, the extra momentum transfer between initial and final states should be coming from reciprocal lattice vector's \mathbf{G} .

a result, the free-electron band dispersion (parabolic bands) will be fully-gapped near the boundaries of the BZ, as shown in Figure (1.5).

In this limit, excitation of an electron due to a photon absorption can only occur if additional momentum is available to transfer the electrons from the initial state to the excited state, both along the energy direction and the momentum direction. Since the photon momentum here is negligible (photon energy imparts energy transfer), additional momentum transfer gained by the electron during the excitation from the initial to the final state comes from the periodicity of the lattice, \mathbf{G} . The \mathbf{G} vectors are the reciprocal lattice vectors and are introduced due to the periodicity of the lattice. Therefore, transitions between the momentum-space points can be expressed through the reciprocal lattice vector as $\mathbf{k}_f - \mathbf{k}_i = \mathbf{G}$. As a result, direct transitions in a photoemission process can be viewed in terms of the picture given by the *extended-BZ scheme*.

If we take into account the effects of the surface during the transition of an electron from the sample into the vacuum, we see that for the elastically-scattered electrons, due to the translational symmetry of the lattice in the x - y plane, the component of the electron momentum parallel to the sample's surface \mathbf{k}_{\parallel} will be conserved to within a reciprocal lattice vector \mathbf{G}_{\parallel} . As for the z -component of the electron momentum, due to the presence of an abrupt potential change along the z axis, the perpendicular momentum \mathbf{k}_{\perp} will not be conserved across the sample surface.

When we match the direct transitions of the bulk Bloch eigenstates inside the sample, which are described above, to the free-electron waves in vacuum, we obtain:

$$|\mathbf{k}_{\parallel}| = |\mathbf{K}_{\parallel}| = \frac{1}{\hbar} \sqrt{2mE_{kin}} \sin(\vartheta) \quad (1.21)$$

If we use the nearly-free electron description of a solid in a photoemission experiment, we can also obtain the perpendicular component of the momentum of a photoelectron in a sample as follows:

$$E_f(k) = \frac{\hbar^2 k^2}{2m} - |E_0| = \frac{\hbar^2 (k_{\parallel}^2 + k_{\perp}^2)}{2m} - |E_0| \quad (1.22)$$

where $E_f(k)$ and E_0 are referenced to the FL and represent electron energies of the final state and the bottom of the valence-band, respectively. Since $E_f = E_{kin} + w$ and $\frac{\hbar^2 k_{\parallel}^2}{2m} = E_{kin} \sin^2 \vartheta$, one can easily show that

$$k_{\perp} = \frac{1}{\hbar} \sqrt{2mE_{kin} \cos^2 \vartheta + V_0} \quad (1.23)$$

where $V_0 = |E_0| + w$ is the inner potential.

It should be noted that the nearly-free-electron approximation for the final state explained above works best for materials in which the Fermi surface has a simple spherical topology (free-electron like). However, this approximation is also quite often used for more

complicated systems, even if the initial states are not free-electron like. For more complicated cases one can use the results of band-structure calculations of the final bulk Bloch states to replace the nearly free-electron picture.

Equations (1.21) and (1.23) will be used in this thesis for determining the final electron wave-vector in our ARPES studies.

1.1.3 Bulk sensitivity vs. surface sensitivity

As discussed in the previous section, within the three-step model of photoemission, the photoexcited electrons in a solid will travel from the bulk of the material to its surface and, during the ‘third step’, will be liberated into the vacuum by overcoming the potential barrier at the surface of the sample.

While propagating within the bulk of the sample, the photoelectrons will be scattered both elastically and inelastically. The elastically-scattered electrons will result in direct transitions (discussed previously in relation with the three-step model) and the inelastically-scattered electrons will yield secondary-electron emission and the appearance of the inelastic background, as discussed earlier.

The photoelectron inelastic mean-free path, or IMFP, is an important parameter used widely to estimate the probing (or information) depth of a photoemission measurement. More precisely, IMFP is the measure of the distance over which the probability of an electron escaping the sample at a depth z , without significant energy loss due to the inelastic

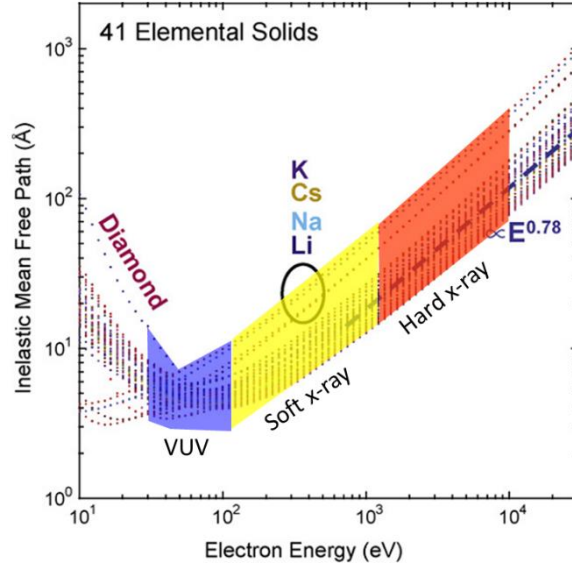


Figure (1.6) – Inelastic mean free path of 41 different elements versus the kinetic energy of the electrons (adapted from Reference [35]).

process, drops to e^{-1} of its original value I_0 at the surface. We consider that, up to this depth, the detected photocurrent from the sample is mostly compromised of the photoelectrons that were scattered elastically, and thus could be interpreted within the framework of the three-step model of photoemission.

Based on the discussion above, it is evident that for the photoelectrons originating from a depth given by z (as measured from the sample surface) the intensity $I(z)$ at the detector will be given by [19]:

$$I(z) = I_0 e^{\frac{-z}{\Lambda \cos(\theta_{TOA})}} \quad (1.24)$$

Here, θ_{TOA} is the photoelectron take-off angle, as measured with respect to the sample's normal, and Λ is the IMFP.

Determination of the IMFP in theory and experiment is a nontrivial problem. Different methods have been used to determine this quantity [33, 34], which is both material- and kinetic-energy-dependent. It has been demonstrated, however, that for most

solids, the photoelectron IMFP will follow the, so called, ‘universal curve’, characterized by the functional dependence on the kinetic energy, as follows [34]:

$$\Lambda = \frac{\alpha}{E^2} + \beta\sqrt{E} \quad (1.25)$$

Here, α and β are empirically-determined constants. Figure (1.6) shows the IMFP curves for 41 elemental solids, calculated with the widely-used TPP-2M formula [35]. As can be seen from Figure (1.6), in the soft x-ray regime (*i.e.* for the kinetic energies ranging from ~250 to 1500 eV) the typical values of the IMFP are in order of 10 Å (or less), which makes such measurement predominantly surface-sensitive. By increasing the photon energies into the hard x-ray regime (~2000 - 10,000 eV), the photoelectron IMFP could be potentially increased up to ~100 Å, thus enhancing the bulk sensitivity of the photoemission measurement [36, 37].

It is important to note that going to very low photon energies (*e.g.* laser-ARPES, with $h\nu = 6$ eV) is often discussed as a way to enhance the probing depth in a photoemission measurement. However, the effectiveness of this approach is highly material-dependent and seems to mostly be applicable to materials with large bandgaps [38]. Therefore, it seems clear that the only universally-robust way of increasing the IMFP and thus enhancing bulk-sensitivity in a photoemission measurement is by increasing the photon energies and carrying out measurements in the soft- and hard x-ray regimes [39, 40].

In the studies described in this thesis, we used photon energies of less than 100 eV to probe the surface states of single-crystalline SmB₆; as well as photon energies on the order of 600-1000 eV to investigate the momentum-resolved electronic structure of an ultrathin (2 unit cell (u.c.)) layer of NdNiO₃, buried under a 4 u.c.-thick capping layer of insulating oxide LaAlO₃. For the latter study, high photon energies were necessary to enhance the

IMFP in order to increase the information depth and be able to probe the buried layer. In this study, we also used photon energies in the hard x-ray regime (6.45 keV) in order to nearly-uniformly probe the entire depth of the sample (with an IMFP of about 85 Å) and to map the DOS of this heterostructure for direct comparison with the first-principles theoretical calculations.

1.2 Kondo insulator (KI) material SmB₆, an introduction

In Chapter 4 we discuss the results of our photoemission study of the single-crystal SmB₆. Here, we briefly describe some of the most important physical features of this complicated correlated electron system.

Strongly-correlated electron systems are a class of materials in condensed-matter physics, in which many-body interaction energies are on the order of or greater than the kinetic energies. To mention some, *cuprate superconductors* [41], *heavy-electron compounds* [42], and *fractional quantum hall systems* [43] fall into the classification of strongly-correlated electron systems in condensed matter. Among these systems, heavy fermion compounds are a large class of correlated materials, with atoms having partially-filled *d* or *f* bands.

The material SmB₆ is a *Kondo insulator*, which has received a lot of recent attention due to the theoretical proposal that it could host topological phases and thus represents the first example of a *topological Kondo insulator (TKI)* [44, 45]. As the next step, we will consider a more general case of the Kondo lattice, wherein magnetic impurities are present at every lattice point of the crystal and are coupled to the itinerant electrons through the hybridization matrix elements. Finally, we will introduce the Kondo insulator materials

and, specifically, SmB₆. At the end, we will briefly discuss possible topological phases in the Kondo insulator materials.

1.2.1 Anderson model and the Kondo effect

Materials with local magnetic moments develop *magnetism*. The simplest example of a local magnetic moment in a material is an unpaired electron in an isolated atom or ion, where a classic Curie-Weiss magnetic susceptibility is given by the Equation (1.26) below:

$$\chi \approx \frac{C}{T+\theta} \quad (1.26)$$

Here C is the *Currie* constant, which is material-dependent, and the *Currie-Weiss* temperature (θ) can be determined from experiment. For positive θ , the material will be *antiferromagnetic (AFM)*, and for negative θ *ferromagnetic (FM)* interaction between magnetic moments is favored [46].

Next, we turn our attention to the problem of the temperature dependence of resistivity in metals. From *Landau's Fermi liquid* theory [47], we know that the electron-electron scatterings in a metal results in a T^2 dependence of the resistivity with respect to temperature, T [48]. Lattice vibrations also contribute to the resistivity of a metal in terms of phonons, which scale as T^5 due to the electron-phonon scattering. The phonons' contribution to the resistivity of a metal was first calculated by Bloch in 1928 [49].

It should be noted that the description given above is not complete. For some metals, such as lead, niobium, and aluminum [50] as temperature is decreased below a characteristic critical value, resistivity becomes zero and gives rise to a superconducting state, wherein two electrons pair-up to form a boson called the Cooper pair [51].

For normal metals that do not exhibit superconductivity (*e.g.* copper and gold), resistivity decreases as the temperature is reduced, until it saturates at a finite temperature-independent value. The residual resistivity is attributed to the scattering of the electrons from impurities and crystal imperfections [52, 53]. Adding more defects will shift the absolute value of this finite residual resistivity to a higher value, but the character of the temperature dependence will remain the same.

The phenomena discussed above are relevant in the context of intrinsic metals, wherein no doped magnetic impurities are present. However, in 1933 [54, 55] during the first experiments on noble metals, such as gold, copper, and silver, it was observed that the resistivity curves exhibit minima at the characteristic temperatures with an upturn (increase) for lower temperatures. Later, it was discovered that this effect was due to the presence of magnetic impurities, such as Mn and Fe, which are naturally present in noble metals. In other words, doping non-magnetic metals with magnetic impurities, such as *3d* transition metals or *4f* rare-earth elements, will give rise to resistivity minima.

In 1960 it was also shown that, when small concentrations of magnetic impurities, such as iron, are added to a metallic sample, they do not always result in a resistivity minimum. For example, iron impurities in pure niobium do not develop a local moment, however they do in the niobium-molybdenum alloy, for the concentrations of molybdenum exceeding 40% [56]. As a result, in both above-mentioned cases, the formation of magnetic moments is responsible for the emergence of the resistivity minimum and a logarithmic temperature-dependent behavior of the resistivity immediately below this minimum [57].

As the temperature is lowered further, the resistivity will no longer exhibit this logarithmic dependence but rather will approach a constant value at $T=0$. At high

temperatures, magnetic susceptibility of the impurity spins follows the Currie-Weiss law, as expected for free magnetic moments. However, below the characteristic temperature described above, the susceptibility approaches a constant value, which is a characteristic of a singlet state where the impurity and the conduction electron spins form a condensate [57]. As a result of this spin condensation, local moments will vanish below this characteristic temperature (screening of the local moments, Kondo effect).

These experimental observations motivated physicists to develop new theoretical models of the magnetic-moment formation. In 1961, Phillip W. Anderson [58] formulated a model describing the formation of localized magnetic moments in dilute magnetic alloys, which is now called the *Anderson single impurity model (ASIM)*, in which a single magnetic impurity is immersed into a Fermi sea of conduction electrons as follows:

$$H = \sum_{\mathbf{k}\sigma} \epsilon_{\mathbf{k}} c_{\mathbf{k}\sigma}^{\dagger} c_{\mathbf{k}\sigma} + \epsilon_d \sum_{\sigma} d_{\sigma}^{\dagger} d_{\sigma} + \sum_{\mathbf{k}\sigma} (V_{d\mathbf{k}} d_{\sigma}^{\dagger} c_{\mathbf{k}\sigma} + hc) + U d_{\uparrow}^{\dagger} d_{\uparrow} d_{\downarrow}^{\dagger} d_{\downarrow} \quad (1.27)$$

Here, $c_{\mathbf{k}\sigma}^{\dagger}, c_{\mathbf{k}\sigma}$ ($d_{\sigma}^{\dagger}, d_{\sigma}$) creates, annihilates a conduction electron (magnetic impurity) with energy $\epsilon_{\mathbf{k}}$ (ϵ_d) and spin σ . The first term is the kinetic energy of the electrons. The magnetic impurity (second term) is represented by a single state with energy ϵ_d . The third term is the s - d hybridization of the d -level with the conduction band (s -band for conduction electrons of a metal and d -band for the transition-metals impurities), and the last term is the Coulomb's cost energy (Hubbard-like term) for double occupancy of the d -level.

The core idea behind the *ASIM* is the presence of the Hubbard like term with energy U . If we suppose that the impurity level with energy ϵ_d is lying below the FL ($\epsilon_d < 0$) and is occupied with a spin-up electron; furthermore, if we take the double-occupancy penalty energy for the d -level to be very large as compared to ϵ_d , then, in order to put another electron into the impurity level with spin down, it will require extra 'penalty'

energy of U . As a result, the DOS of the spin-down electrons will remain zero and thus, in effect, the formation of a local magnetic moment can be explained. On the other hand, if we suppose that U is not large enough, as compared to ϵ_d , then, due to the hybridization processes the number of the conduction electrons will decrease, and so will the energy of the impurity state with spin-down. As a result, the states with spins that are up and down will move closer to each other and approach the FL. If this process is strong enough, then a solution with nonmagnetic ground states will be achieved [59].

The above explanation is provided in the mean-field approximation [59]. Inclusion of the effects stemming from the correlations between localized electrons, as well as those between localized and conduction electron, will lead to more complicated processes. In fact, at $T=0$ the magnetic moments will be screened completely and, as a result, a nonmagnetic ground state will form.

The important concept in this description is the presence of a virtual bound state with the energy level which is close to the FL, on which the conduction electrons can be localized as a result of the hybridization function V_{dk} in a spin-exchange process. The electron from the localized impurity state can tunnel to an unoccupied state just above the FL, and another electron from the Fermi sea can replace it. If these electrons have different spins, this process is called a ‘spin-flip process’. An alternate spin-flip process is the double occupancy of the impurity level with a cost of Coulomb energy U . As mentioned above, when all these processes happen together, a many-body phenomenon known as the ‘Kondo resonance’ is created with a spin singlet state and a width of $\sim k_B T_K$, which is pinned at the FL.

The value of the Kondo resonance ($k_B T_K$) is determined from the energy scales in the single impurity Anderson Hamiltonian. Through this process, the bandwidth of the impurity state will be shifted closer to the FL and broadened through the hybridization with the electrons in the *Fermi Sea*. As a result, close to the impurity level, the local moment will be screened.

The Kondo temperature (T_K) introduced above, sets the energy scale for the crossover between the local magnetic behavior (free spin) and the low-temperature physics, where the spin and the conduction electrons are entangled to form a spin-singlet state. The mechanism by which the local moments are screened results in the Kondo effect. In order to explain the physics of the interaction between the local magnetic moments and the conduction electrons via a spin-spin exchange process, we will introduce the Kondo model.

The Hamiltonian for the antiferromagnetic exchange interaction between the magnetic moments and spin density of the surrounding medium is assumed to be

$$H = J \vec{\sigma} \cdot \vec{S} \quad (1.28)$$

where \vec{S} is the spin of the local moment and $\vec{\sigma}$ is the spin-density of the electron medium. The antiferromagnetic interaction is an example of super-exchange, resulting from high-energy valence fluctuations between the conduction electrons (for instance, *s*-shell of Au) and the localized electrons (*d*-shell, in case of a transition-metal impurity) [58,60].

From Schrieffer-Wolf transformations [61] it can be shown that, in the Kondo regime, where the transitions into the unoccupied and doubly-occupied states are blocked (large U), virtual processes lead to an effective antiferromagnetic coupling J between the impurity spins (located at the origin) and the conduction-electrons spins. The coupling

constant J is a function of the hybridization strength V , impurity state energy level ϵ_d , and the Coulomb's cost energy U :

$$J = |V|^2 \left[\frac{1}{\epsilon_d + U} - \frac{1}{\epsilon_d} \right] \quad (1.29)$$

As a result, the effective Hamiltonian can be written in a form of Equation (1.30) below.

Jun Kondo in 1964 [62], incorporated the antiferromagnetic interaction from Anderson's description into a model which is now called the *Kondo model*:

$$H = \sum_{\mathbf{k}\sigma} \epsilon_{\mathbf{k}} c_{\mathbf{k}\sigma}^\dagger c_{\mathbf{k}\sigma} + J \psi^\dagger(0) \vec{\sigma} \psi(0) \cdot \vec{S} \quad (1.30)$$

Here, once again, $c_{\mathbf{k}\sigma}^\dagger, c_{\mathbf{k}\sigma}$ creates, annihilates a conduction electron with energy $\epsilon_{\mathbf{k}}$ and momentum \mathbf{k} ; $\psi^\dagger(0)$ creates a conduction electron at the origin and, as before, \vec{S} is the magnetic impurity's spin.

Kondo then obtained the magnetic scattering rate of electrons as a function of temperature to one order of approximation higher, compared to the Born approximation in the perturbation theory (T-matrix formalism), as follows:

$$J(T) \approx J + 2 J^2 \rho \text{Ln} \frac{D}{T} \quad (1.31)$$

Here, ρ is the DOS for the conduction sea per spin and D is the bandwidth for the conduction band.

Based on Kondo's findings, as the temperature drops, the coupling constant, scattering rate and the resistivity should start to rise. When the rise in the magnetic scattering ($\sim \text{Ln} \frac{D}{T}$) overcomes the phonon scattering ($\sim T^5$), resistivity should develop a minimum. Hence, the physics of an isolated magnetic ion can be explained by the Kondo

model, and the resistivity minimum puzzle can be solved by introducing an antiferromagnetic interaction between the localized spins and their surrounding medium.

Historically, position of the resistance minimum along the temperature scale was chosen as the definition of the Kondo temperature, but this definition is not complete since it depends on the details of the phonon scattering processes (from the electron-phonon scattering contribution to the resistivity curve). In the modern approach, the characteristic temperature, as explained in the following, is chosen as a temperature at which the Kondo treatment is not valid anymore. It is easy to see that for temperatures on the order of

$$T_k \sim D e^{\frac{-1}{2\rho J}} \quad (1.32)$$

the correction due to the perturbation theory becomes as large as the original perturbation (J); and at lower temperatures, Kondo interaction can no longer be treated as a perturbation. As a result of this, Kondo treatment is suitable only for temperatures above the Kondo temperature (T_k), and the physical meaning of the model below this characteristic temperature remains unsolved ('the Kondo problem').

The numerical renormalization method invented by Wilson [63] showed that the effect should be stable down to very low temperatures. A new concept introduced here was that physics of the spin in a metal depends on the energy scale at which it is probed. In other words, this effect is an example of the *asymptotic freedom*, where at high energies local moments inside a metal are asymptotically free, but when the temperature falls below a characteristic temperature (here, Kondo temperature), local moments will interact strongly with the surrounding medium where they screen into a singlet state [64,65].

The mechanism of screening of the local moment is known as the *Kondo effect*. Since the electron scattering in this model does not conserve momentum (lack of translational

invariance due to the single impurity at the origin), large resistivity builds up at low temperatures.

Now, we will discuss the fate of the system as T approaches zero, and thus the Kondo treatment is no longer valid. It is now established that as T approaches zero, a Fermi-liquid behavior is achieved (with renormalized parameters), and that such behavior could be explained in terms of the Kondo resonance.

In Landau's Fermi-liquid theory, the magnetic susceptibility is independent of temperature at low temperatures (Equation (1.33 a)) and the specific heat has a linear dependence on temperature ($C = \gamma T$). The specific heat coefficient (γ) arising from the electron-electron interactions is given by Equation (1.33 b):

$$\chi = \mu_B \frac{\rho^*}{1+F_0^a} \quad (1.33 \text{ a})$$

$$\gamma = \frac{\pi^2 k_B^2}{3} \rho^* \quad (1.33 \text{ b})$$

where ρ^* is the normalized DOS ($\rho^* = \frac{m^*}{m} \rho$) and F_0^a is the spin-dependent part of the interactions between quasiparticles (Landau parameters).

As explained earlier, a peak of width $\sim k_B T_k$ in the DOS will develop near the FL for the Fermi-liquid phase. At temperatures far below T_k , a large DOS will form, which will manifest itself in the large specific-heat coefficient of the Kondo systems. From Equations (1.33) it is evident that the normalized DOS due to the Kondo resonance determines the strength of the enhanced renormalized parameters. We should note that, for a Kondo system with a single impurity, this effect will not be as large as that observed in the heavy-fermion metals with a large reservoir of magnetic impurities ($\sim 10^{23}$). For the latter, the

much larger effect will manifest itself, for example, in the enhanced specific heat coefficient ($\gamma_{heavy\ fermion} \sim 1000 \gamma_{free\ electron}$).

1.2.2 Heavy-fermion metals and Kondo lattice

In this section, we will follow the scientific line of reasoning in Reference [59]. Previously, we have assumed that the impurity-level energy is far from the FL and considered the effects of the Kondo resonance within the framework of the single-impurity Anderson model. In the realm of heavy-fermion materials and mixed-valence systems, such as rare-earth (4*f*) and Actinide (5*f*) compounds, this constraint could be lifted and, in a more general case, the impurity level could be brought up closer to the FL.

First heavy-fermion metal, CeAl₃, was discovered in 1976 [66]. The characteristic features of heavy-fermion metals are: (i) the Curie-Weiss susceptibility at high temperatures $\chi \sim (T + \theta)^{-1}$, (ii) the paramagnetic spin susceptibility $\chi \sim \text{constant}$ at low temperatures, (iii) linear temperature dependence of the specific heat at low temperature (Fermi-liquid behavior with effective quasiparticle masses of more than 1000 times the electron mass), and (iv) quadratic temperature dependence of the low-temperature resistivity ($\sim T^2$).

The simplest Hamiltonian proposed for describing the physics governing the behavior of such heavy-fermion materials is the periodic Anderson model, where the *s-d* mixing (which was originally proposed in the Anderson single-impurity model), is replaced with the *s-f* mixing, essentially switching-out the *d*-orbitals with the *f*-orbitals of the rare-earth or actinide elements.

There are several energy regions, which are highly-relevant in the context of the heavy-fermion materials. The Hubbard energy U and the bandwidth D of the conduction electrons for these materials are usually large. As in the case of the Anderson single-impurity model, for large Hubbard energy it could also be shown that the periodic Anderson model could be replaced with the Kondo lattice model (a lattice version of the single-impurity Kondo model) [67-69]. Here, in effect, we go from the periodic Anderson model to the Kondo lattice model, where the exchange interaction energy J can be written as

$$J = \frac{2V^2}{\epsilon_F - \epsilon_f} \quad (1.34)$$

where ϵ_f is the energy of the impurity level.

The simplest Kondo lattice Hamiltonian is given by

$$H = \sum_{\mathbf{k}\sigma} \epsilon_{\mathbf{k}} c_{\mathbf{k}\sigma}^\dagger c_{\mathbf{k}\sigma} + J \sum_j \vec{S}_j \cdot c_{j\alpha}^\dagger \vec{\sigma}_{\alpha\beta}^\dagger c_{j\beta} \quad (1.35)$$

where $c_{j\alpha}^\dagger$ creates an electron on site j and, as before, \vec{S}_j is the magnetic impurity spin.

Before discussing the effects of the different value of the exchange energy interaction J , we should note that there are two competing magnetic interactions between the local magnetic moments and the conduction electrons in a heavy-fermion material. The presence of an array of magnetic impurities induces a long-range oscillatory magnetic interaction, called the RKKY (Ruderman–Kittel–Kasuya–Yosida) interaction [70]. In the limit wherein the density of the magnetic impurities is low, the RKKY interaction gives rise to a frustrated (glassy) magnetic state, known as the ‘spin glass’. Conversely, in the dense limit it induces an ordered antiferromagnetic state with a Neel temperature on the

order of $T_N \sim J^2 \rho$. The other competing magnetic interaction is the Kondo effect, as discussed previously, which scales as $T_k \sim D \exp(\frac{-1}{2\rho J})$.

In heavy-fermion systems, Kondo scattering will occur at all the lattice sites and, as explained in the previous section, the Kondo resonance peak at the FL will be very large due to the presence of many scattering points, leading to a significant enhancement of the Landau's parameters. In contrast with the single-impurity Kondo model, in a lattice with translational symmetry elastic scattering of the electrons will conserve momentum, which will in-turn lead to the coherent scattering of Kondo singlets. As a result, the resistivity of a heavy-fermion metal will drop toward zero below the Kondo temperature [71].

We will now return to the original discussion of the effects of different values of the exchange interaction energy J on the physical properties of the system. First, we will assume that the impurity level is far below the FL. For this case, it is evident from Equation (1.34) that the exchange interaction energy will be small and the RKKY interaction will overcome the Kondo effect, leading to an antiferromagnetic ground state. These effects are illustrated in the Doniach phase diagram [68].

Second, from Equation (1.34), it is also evident that by bringing the impurity level closer to the FL, we increase the strength of the exchange interaction. By doing so, we enter the region where the Kondo effect will be sizable, compared to the effects from the RKKY interaction. For this case, the impurity level is still far from the Fermi energy, but it is now closer to the FL, as compared to the first scenario. Thus, we expect that the occupation number of the f -level is still close to one. As a result, the Neel temperature for the antiferromagnetic ordering will reduce, and it is said that the system is now close to a heavy-fermion quantum critical point (QCP).

The third scenario arises when the energy of the impurity level approaches that of the FL. In this limit, Equation (1.34) is no longer valid, and one can no longer use the effective Kondo lattice model. Thus, in this limit, it is necessary to revert back to the original periodic Anderson model. This scenario is relevant for the mixed-valence systems, wherein, due to an intermediate occupation of the f shell, the occupation number of the f -level is no longer unity. For example, in SmB_6 , which is a mixed-valence material, the valence of the f -shell is fluctuating between $\text{Sm}^{3+} (4f^5)$ and $\text{Sm}^{2+} (4f^6)$. We should note that the physics of mixed-valence materials is still under investigation and, in fact, is on the frontier of condensed matter physics.

The fourth scenario arises when the f -level moves above the FL. In this case, all the f states will reside in the conduction band and, thus, the impurity level will be empty. As a result, a nonmagnetic metallic phase is obtained.

1.2.3 Kondo insulators

In this section we focus our attention on a more complicated case of heavy fermion materials known as Kondo insulators and, specifically, on SmB_6 , which was discovered in 1969 [72]. At room temperature SmB_6 exhibits magnetic Currie-Weiss susceptibility but, upon cooling below a coherence temperature of about 100-150 K, transforms into a paramagnetic insulator with a hybridization gap of about 21 meV in the bulk DOS [73, 74].

The periodic Anderson model, which is suitable for heavy-fermion materials, can be solved by various techniques. For heavy fermions, the excitonic ordering between the localized f electrons and the conduction electrons (d bands) drives an emergent hybridization gap [75]. The mean-field treatment using the slave boson technique results

in quasi-particle bands, wherein the DOS exhibits a hybridization gap. Specifically, there are two gaps present in the hybridization gap – direct and indirect. The direct gap has a value of $2\tilde{V}$, where \tilde{V} is the renormalized hybridization strength; and the indirect gap has a size proportional to the Kondo temperature. The energy of the f -bands will also be highly renormalized to values closer to the FL. The mixing character between the f -bands and the d -bands in mixed-valence materials is crucial in realizing the topological phases due to the possibility of band inversion. This effect will be discussed in the last section of this chapter.

In heavy-fermion metals, the chemical potential lies within the valence band and, hence, metallicity is expected for these materials. In the special case of SmB_6 , additional heavy f -quasiparticles dope the metal to form a strongly-correlated insulator. The bulk impurity states pin the chemical potential within the hybridization gap and, as a result, the bulk properties are characterized by a thermal activation in the resistivity and the specific heat within an activation energy of approximately 4 meV [76-78].

The value of the gap in a heavy-fermion semiconductor is usually on the order of 10 meV (small gap size is due to the strong Coulomb interaction between the f -electrons) and is temperature-dependent, which is indicative of many-body renormalizations, as mentioned above.

1.2.4 Spin excitons

In this section we will focus on reviewing the key results obtained in References [79-82]. Inelastic neutron scattering measurements have identified anomalous features in the dispersions of heavy-fermion semiconductors SmB_6 [83] and YbB_{12} [84]. These features have excitation energies that are less than the bulk-gap formed by the hybridization

between f and d states, as explained earlier in this Chapter. Furthermore, these excitations disperse with the momentum transfer q and have a minimum at the corner of the first Brillouin zone (R point in the BZ of the cubic crystal of SmB_6).

As was mentioned earlier, there are two competing magnetic interactions present in the heavy fermion metals: the Kondo effect and the RKKY-type interactions from long-range interactions between local magnetic moments. As described phenomenologically by the Doniach phase diagram [68], the QCP will separate these two phases from each other. Since heavy fermions are characterized by small Kondo temperatures, it is believed that the heavy-fermion materials live near a QCP.

For a metal with a paramagnetic phase, the QCP is dominated by the magnetic fluctuations known as paramagnons [85] or anti-paramagnons [86], depending on whether the paramagnetic state is unstable toward the ferromagnetic or anti-ferromagnetic phase, respectively. These fluctuations can decay into particle-hole pairs, and their frequencies soften as the wave vector of the fluctuations approaches the wave vector of the magnetically ordered state. As the QCP is approached, the frequencies of these fluctuations decrease, and their amplitudes increase.

Analogous to the magnetic fluctuations in a metal, for semiconductors that are close to the QCP, spin-excitons are predicted to emerge as the relevant magnetic fluctuations [87]. Spin-excitons are magnetically-bound states of an electron-hole pair with non-zero total angular momentum. Spin-exciton dispersion relation has a minimum occurring at the wave vector of the magnetically-ordered state. In contrast to the metallic case, semiconductors have no low-frequency particle-hole channels available. Thus, as the QCP

is approached, frequency of these fluctuations softens, and the magnetic instability is produced.

Spin-excitons are purely-magnetic excitations, and thus cannot be detected via optical absorption measurements [88]. They were first described within the framework of the periodic Anderson model [79-81], and can be derived as the magnetic excitations of the paramagnetic state in the Anderson lattice model.

Since the system is cubic and also paramagnetic, the bulk magnetic susceptibility is isotropic in spin space. Thus, in the random phase approximation (RPA), magnetic susceptibility of the f -electrons can be evaluated as follows [79]:

$$\chi(q, \omega) = \frac{\chi^0(q, \omega)}{1 - J(q)\chi^0(q, \omega)} \quad (1.36)$$

where $\chi^0(q, \omega)$ is the irreducible f -electron quasiparticle susceptibility associated with the particle-hole excitations, and $J(q)$ is an exchange-interaction term, which is a combination of the RKKY-type interaction and the Anderson super-exchange interaction. For sufficiently large values of the exchange interaction, the denominator of the susceptibility may vanish at a frequency ω_q within the gap, which can be derived from the criteria below:

$$1 - JRe(\chi^0(q, \omega_q)) = 0 \quad (1.37 \text{ a})$$

$$Im(\chi^0(q, \omega_q)) = 0 \quad (1.37 \text{ b})$$

At this specific frequency, density of the magnetic excitations reduces to a delta function peak:

$$Im(\chi(q, \omega)) = \frac{sign(\omega)}{Z_q} \pi \delta(\omega - \omega_q) \quad (1.38)$$

where Z_q is a dimensionless factor, defined as a derivative with respect to ω :

$$Z_q = \left| J^2 \frac{\partial}{\partial \omega} \text{Re}(\chi^0(q, \omega)) \Big|_{\omega=\omega_q} \right| \quad (1.39)$$

where Z_q^{-1} determines the intensity of the spin exciton. For paramagnetic semiconductors, a spin-exciton will have a minimum in its dispersion at the R point in the BZ, as in the case of SmB_6 . Away from the R point, the spin-exciton excitation energy will increase and eventually merge with the particle-hole continuum [82]. Therefore, the spin-exciton in SmB_6 can be regarded as a precursor excitation for an antiferromagnetic instability that occurs close to a QCP. Near the QCP, the value of the spin exciton energy ω_q is expected to be small.

In Chapter 4 we discuss the effects of spin-exciton coupling on the surface states of SmB_6 , which destroys the topological protection due to the time-reversal invariance and spin-momentum locking.

1.2.5 Topological phases of Kondo insulators

In this section we will follow the line of reasoning described in References [44, 45]. In SmB_6 , the Sm $4f$ electrons are subject to a strong spin-orbit coupling [81]. It has been predicted that in Kondo insulators, topologically-nontrivial insulating states should emerge due to the strong spin-orbit coupling arising from the hybridization between the conduction d electrons and the f electrons. [44]. As a result, in these materials, the emergent topological phase is a direct consequence of the strong electronic correlations.

Up until recently, most topological materials have been classified as weakly-correlated electron systems [89]. However, search for candidate topological phases in the strongly-correlated materials has been gaining significant momentum [90]. Due to the discontinuity in the topological character at the interface between a topological insulator

(TI) and vacuum, gapless surface states (Weyl cones) should persist at the surface. These states are robust and are topologically protected against disorder. For ‘weak’ topological insulators, the number of Weyl cones is zero or even, and for ‘strong’ topological insulators this number is odd

It is shown that, for a time-reversal-invariant band insulator in three dimensions, topological phases can be identified with four Z_2 indices [91]. The first Z_2 index (ϑ_0) determines if the material is a strong TI ($\vartheta_0=1$) or a weak TI ($\vartheta_0=0$). For material SmB_6 , the renormalized f -bands are very close to the FL [92]. Calculations show that for a Kondo material to have strong topological phase, the f -bands should lie close to the FL, as in the case of SmB_6 . In fact, this scenario is usually true for the mixed-valent systems, such as SmB_6 . In SmB_6 , band inversion happens at the X point of the BZ, which results in a strong topological phase, based on the Z_2 definition of the topological indices. As a result, the predicted topological phases of SmB_6 may be responsible for the surface conduction at low temperatures, below 5 K [93].

References Cited in Chapter 1

- [1] H. R. Hertz, About an Influence of the Ultraviolet Light on the Electric Discharge, *Ann. Phys. Lpz.*, **33**, 983 (1887).
- [2] W. Hallwachs, About the Influence of Light on Electrostatically Charged Bodies, *Ann. Phys. Lpz.*, **33**, 301 (1888).
- [3] A. Einstein, About a Heuristic Point of View Concerning the Generation and Transformation of light, *Ann. Phys. Lpz.*, **17**, 132 (1905).
- [4] P.A. Wolff, Theory of Secondary Electron Cascade in Metals, *Phys. Rev.*, **95**, 56 (1954).
- [5] D. A. Shirley, High-Resolution X-Ray Photoemission Spectrum of the Valence Bands of Gold, *Phys. Rev. B*, **5**, 4709 (1972).
- [6] Xiaomei Li, Zhaoming Zhang and Victor E. Henrich, Inelastic Electron Background Function for Ultraviolet Photoelectron Spectra, *J. Electron Spectrosc. Relat. Phenom.*, **63**, 253-265 (1993).
- [7] D. E. Eastman, J. A. Knapp, and F. J. Himpsel, Direct Determination of Lifetime and Energy Dispersion for the Empty Conduction Band of Copper, *Phys. Rev. Lett.*, **41**, 825 (1978).
- [8] J. A. Knapp, F. J. Himpsel, and D. E. Eastman, Experimental Energy Band Dispersions and Lifetimes for Valence and Conduction bands of Copper Using Angle-Resolved Photoemission, *Phys. Rev. B*, **19**, 4952 (1979).
- [9] B. J. Slagsvold, J. K. Grepstad and P. O. Gartland, Band Structure Dependent Damping in Photoemission from Copper, *J. Phys. F: Met. Phys.*, **12**, 1679-87 (1982).
- [10] P. H. Citrin, P. Eisenberger, and D. R. Hamann, Phonon Broadening of X-Ray Photoemission Linewidths, *Phys. Rev. Lett.*, **33**, 965 (1974).
- [11] J. W. Gadzuk, S. Holloway, C. Mariani and K. Horn, Temperature-Dependent Photoemission Line Shapes of Physiosorbed Xenon, *Phys. Rev. Lett.*, **48**, 1288 (1982).
- [12] G. D. Mahan, Excitons in Metals: Infinite Hole Mass, *Phys. Rev.*, **163**, 612 (1967).
- [13] G. K. Wertheim and S. Hufner, Many-Body Line Shape in X-Ray Photoemission from Metals, *Phys. Rev. Lett.*, **35**, 53 (1975).
- [14] A. Bodicker and W. Schattke, Theoretical Photoemission Line Shapes and Many Body Correlations, *J. Electron Spectrosc. Relat. Phenom.*, **76**, 265-270 (1995).

-
- [15] A. Fahlman, C. Nordling, K. Siegbahn, ESCA: Atomic, Molecular and Solid-State Structure Studied by Means of Electron Spectroscopy, Vol **20** (1967).
- [16] J. A. Samson, Techniques of Vacuum Ultraviolet Spectroscopy (Wiley, New York, 1980).
- [17] S. D. Kevan, Chapter 1, Angle Resolved Photoemission Theory and Current Applications, (Elsevier, New York, 1992).
- [18] Electrostatic energy analyzers are now commercially available, see for example, the homepage of VG Scienta <http://www.vacgen.com> and the homepage of SPECS GmbH <http://www.specs.de>.
- [19] S. Hufner, Photoelectron Spectroscopy, (Springer, New York, 2003).
- [20] A. Sommerfeld, On the Electron Theory of Metals on the Basis of Mixing Statistics, *Z. fur Physik.*, **47**, 1 (1928).
- [21] H. Y. Fan, Theory of Photoelectric Emission from Metals, *Phys. Rev.*, **68**, 43 (1945).
- [22] C. N. Berglund and W. E. Spicer, Photoemission Studies of Copper and Silver: Theory, *Phys. Rev.*, **136**, 1030 (1964).
- [23] J. B. Pendry, Theory of Photoemission, *Surf. Sci.*, **57**, 679 (1976).
- [24] J. Braun, J. Minár, and H. Ebert, Correlation, Temperature and Disorder: Recent Developments in the One-step Description of Angle-resolved Photoemission, *Phys. Rep.*, **740**, 1 (2018).
- [25] Ebert, D. Ködderitzsch, and J. Minár, Calculating Condensed Matter Properties Using the KKR-Green's Function Method—Recent Developments and Applications, *Rep. Prog. Phys.*, **74**, 096501 (2011).
- [26] J. J. Sakurai, J. Napolitano, Modern Quantum Mechanics, (Adison-Wesley, 2011).
- [27] Henrik Bruus and Karsten Flensberg, Many-Body Quantum Theory in Condensed Matter Physics, (Oxford Graduate Texts, 2002).
- [28] M. Mulazzi, M. Hochstrasser, M. Corso, I. Vobornik, J. Fujji, J. Osterwalder, J. Henk, and G. Rossi, Matrix Element Effects in Angle-Resolved Valence Band Photoemission with Polarized Light from the Ni (111) Surface, *Phys. Rev. B*, **74**, 035118 (2006).

-
- [29] C. N. Veenstra, G. L. Goodvin, M. Berciu and, A. Damascelli, Elusive Electron-Phonon Coupling in Quantitative Analyses of the Spectral Function, *Phys. Rev. B*, **82**, 012504 (2010).
- [30] Tom Lancaster and Stephan J. Blundell, Quantum Field Theory for the Gifted Amateur, (Oxford University Press, New York, 2016).
- [31] Andrea Damascelli, Zahid Hussain, and Zhi-Xun Shen, Angle-Resolved Photoemission Studies of the Cuprate Superconductors, *Rev. Mod. Phys.*, **75**, 473 (2003).
- [32] Thierry Giamarchi, Anibal Iucci, Christophe Berthod, Introduction to Many Body physics, Lecture Notes, University of Geneva, (2013).
- [33] M. P. Seah, W. A. Dench, *Quantitative Electron Spectroscopy of Surfaces: Surf. Interface Anal.*, **I**, 86 (1979).
- [34] H. Ibach, In Electron Spectroscopy for Surface Analysis, Vol. **4** (Springer, Berlin, 1977).
- [35] S. Tanuma, C. J. Powell, O. R. Penn, Calculations of Inelastic Mean Free Paths, *Surf. Interface Anal.*, **21**, 165 (1993).
- [36] A. Jablonski, and, C. J. Powell, Practical Expressions for the Mean Escape Depth, the Information Depth, and the Effective Attenuation Length in Auger-electron Spectroscopy and X-ray Photoelectron Spectroscopy, *J. Vac. Sci. Technol. A*, **27**, 253 (2009).
- [37] W. S. M. Werner, W. Smekal and, C. J. Powell, NIST Database for the Simulation of Electron Spectra for Surface Analysis, Version 1.3, National Institute of Standards and Technology, Gaithersburg, Maryland (2011).
- [38] J. C. Woicik, Hard X-ray Photoelectron Spectroscopy, (Springer, New York, 2016).
- [39] A. X. Gray, C. Papp, S. Ueda, B. Balke, Y. Yamashita, L. Plucinski, J. Minár, J. Braun, E. R. Ylvisaker, C. M. Schneider, W. E. Pickett, H. Ebert, K. Kobayashi and C. S. Fadley, Probing Bulk Electronic Structure with hard X-ray Angle-Resolved Photoemission, *Nat. Mat.*, **10**, 759 (2011).
- [40] A. X. Gray, J. Minár, L. Plucinski, M. Huijben, A. Bostwick, E. Rotenberg, S.-H. Yang, J. Braun, A. Winkelmann, and G. Conti, Momentum-Resolved Electronic Structure at a Buried Interface from Soft X-ray Standing-Wave Angle-Resolved Photoemission, *Europhys. Lett.*, **104**, 17004 (2013).
- [41] Patrick A. Lee, N. Nagaosa and Xiao-Gang Wen, Doping a Mott Insulator: Physics of High Temperature Superconductivity, *Rev. of Mod. Phys.*, **78**, 17 (2006).

-
- [42] G. R. Stewart, Heavy-Fermion Systems, *Rev. Mod. Phys.*, **56**, 4 (1984).
- [43] J. K. Jain, Composite Fermion Theory of Exotic Fractional Quantum Hall Effect, *Annu. Rev. Condens. Matter Phys.*, **6**, 39 (2015).
- [44] M. Dzero, K. Sun, V. Galitski, and P. Coleman, Topological Kondo Insulators, *Phys. Rev. Lett.*, **104**, 106408 (2010).
- [45] T. Takimoto, SmB₆: A Promising Candidate for a Topological Insulator, *J. Phys. Soc. Jpn.*, **80**, 123710 (2011).
- [46] R. K. Pathria, Statistical Mechanics, (Elsevier, Great Britain, 2007).
- [47] L. D. Landau, The Theory of a Fermi Liquid, *Soviet. Phys. JETP.*, **3**, 6 (1957).
- [48] N. Wisser. The Electrical Resistivity of the Simple Metals. *Contemp. Phys.*, **25**, 211 (1984).
- [49] F. Bloch, About the Quantum Mechanics of Electrons in Crystal Lattices, *Z. Phys.*, **52**, 555 (1928)
- [50] J. F. Cochran, D. E. Mapother, and R. E. Mould, Superconducting Transition in Aluminum, *Phys. Rev.*, **103**, 1657 (1956).
- [51] J. Bardeen, L. N. Cooper, and J. R. Schrieffer, Theory of Superconductivity, *Phys. Rev.*, **108**, 1175 (1957).
- [52] R. P. Gupta, Residual Resistivity of Defects in Metals, *Phys. Rev. B*, **35**, 5431 (1987).
- [53] J. Bass, W. P. Pratt, and P. A. Schroeder, The Temperature-dependent Electrical Resistivities of the Alkali Metals, *Rev. Mod. Phys.*, **62**, 3 (1990).
- [54] W. J. de Haas, J. H. de Boer, and G. J. van den Berg, The Electrical Resistance of Gold, Copper and Lead at Low Temperatures, *Physics*, **1**, 1115 (1933).
- [55] D. K. C. MacDonald, K. Mendelssohn, Resistivity of Pure Metals at Low Temperatures: Alkali Metals, *Proc. R. Soc. London*, **202**, 523 (1950).
- [56] M. Sarachik, E. Corenzwit, and L. D. Longinotti, Resistivity of Mo-Nb and Mo-Re Alloys Containing 1% Fe, *Phys. Rev. A*, **135**, 1041 (1964).
- [57] A. J. Heeger, Solid State Physics, (Academic Press, New York, 1969).
- [58] P. W. Anderson, New Approach to the Theory of the Super Exchange Interactions, *Phys. Rev.*, **115**, 2 (1959).

-
- [59] Daniel Khomskii, Basic Aspects of the Quantum Theory of Solids, (Cambridge University Press, 2010).
- [60] P. W. Anderson, Localized Magnetic States in Metals, *Phys. Rev.*, **124**, 41 (1961).
- [61] J. R. Schrieffer, P. A. Wolf, Relation Between Anderson and Kondo Hamiltonians, *Phys. Rev.*, **149**, 491 (1966).
- [62] J. Kondo, Resistance Minimum in Dilute Magnetic Alloys, *Prog. Theor. Phys.*, **32**, 37 (1964).
- [63] K. G. Wilson, The Renormalization Group: Critical Phenomenon and the Kondo Problem, *Rev. Mod. Phys.*, **47**, 773 (1975).
- [64] P. Nozieres, A Fermi Liquid Description of the Kondo Problem at Low Temperatures, *J. Phys., Colloq.*, **37**, 1 (1976).
- [65] P. Nozieres and A. Blandin, Kondo Effect in Real Metals, *J. Phys.*, **41**, 193 (1980).
- [66] K. Andres, J. Graebner, and H. R. Ott, 4f-Virtual-Bound-State Formation in CeAl₃ at Low Temperatures, *Phys. Rev. Lett.*, **35**, 1779 (1975).
- [67] N. F. Mott, Rare Earth Compounds with Mixed Valences, *Philops. Mag.*, **30**, no. 2, 403 (1974).
- [68] S. Doniach, Kondo Lattice and the Weak Antiferromagnetism, *Physica*, **91B**, 231 (1977).
- [69] T. Kasuya, A Theory of Metallic Ferro- and Antiferromagnetism on Zener's Model, *Prog. Theor. Phys.*, **16**, 45 (1956).
- [70] M. A. Ruderman, C. Kittel, Indirect Exchange Coupling of Nuclear Magnetic Moments by Conduction Electrons, *Phys. Rev.*, **96**, 99 (1954).
- [71] J. L. Smith and P.S. Riseborough, Actinides, the Narrowest Band, *J. Magn. Magn. Mater.*, **47**, 545-548 (1985).
- [72] A. Menth, E. Buehler, and T. H. Geballe, Magnetic and Semiconducting Properties of SmB₆, *Phys. Rev. Lett.*, **22**, 295 (1969).
- [73] H. Miyazaki, T. Hajiri, T. Ito, S. Kunni, and S. I. Kimura, Momentum-Dependent Hybridization Gap and Dispersive In-Gap State of the Kondo Semiconductor SmB₆, *Phys. Rev. B*, **86**, 075105 (2012).

-
- [74] X. Zhang, N. P. Butch, P. Syers, S. Ziemak, R. L. Greene, and J. Paglione, Hybridization, Inter-Ion Correlation, and Surface States in the Kondo Insulator SmB_6 , *Phys. Rev. X*, **3**, 011011 (2013).
- [75] P. S. Riseborough, Theory of Dynamic Magnetic Response of $\text{Ce}_3\text{Bi}_4\text{Pt}_3$: A Heavy-Fermion Semiconductor, *Phys. Rev. B*, **45**, 984 (1992).
- [76] K. Flachbart, K. Gloos, E. Konovalova, Y. Paderno, M. Reiffers, P. Samuely, and P. Svec, Energy Gap of Intermediate-Valent SmB_6 Studied by Point-Contact Spectroscopy, *Phys. Rev. B*, **64**, 085104 (2001).
- [77] B. Gorshunov, N. Sluchanko, A. Volkov, M. Dressel, G. Knebel, A. Loidl, and S. Kunii, Low-Energy Electrodynamics of SmB_6 , *Phys. Rev. B*, **59**, 1808 (1999).
- [78] Yazhou Zhou, Qi Wu, Priscila F. S. Rosa, Rong Yu, Jing Guo, Wei Yi, Shan Zhang, Zhe Wang, Honghong Wang, Shu Cai, Ke Yang, Aiguo Li, Zheng Jiang, Shuo Zhang, Xiangjun Wei, Yuying Huang, Yi-feng Yang, Zachary Fisk, Qimiao Si, Liling Sun, and Zhongxian Zhao, Quantum Phase Transition and Destruction of Kondo Effect in Pressurized SmB_6 , *Science Direct*, **62**, 1439 (2017).
- [79] P.S. Riseborough, Magnetic Bound States in SmB_6 , *Ann. Phys.*, **9**, 813 (2000).
- [80] P.S. Riseborough, Spin-Excitons in Heavy-Fermion Semiconductors, *J. Magn. Magn. Mater.*, **226**, 127 (2001).
- [81] P.S. Riseborough, Collapse of the Coherence Gap in the Semiconductors, *Phys. Rev. B*, **68**, 235213 (2003).
- [82] G. A. Kapilevich, P. S. Riseborough, A. X. Gray, M. Gulacsi, Tomasz Durakiewicz, and J. L. Smith, Incomplete Protection of the Surface Weyl Cones of the Kondo Insulator SmB_6 : Spin Exciton Scattering, *Phys. Rev. B*, **92**, 085133 (2015).
- [83] P. M. Alekseev, J. M. Mignot, J. M. Rossat-Mignot, V. N. Lazukov, and I. P. Sadikov, The Origin of Sm Ion Intermediate Valence State in SmB_6 , *Physics B*, **186**, 384 (1993).
- [84] A. Bouvet, T. Kasuya, M. Bonnet, L. P. Regnault, J. Rossat-Mignod, F. Iga, B. Fak, and A. Severing, Magnetic Excitations Observed by Means of Inelastic Neutron Scattering in Polycrystalline YbB_{12} , *J. Phys.: Conds. Matter.*, **10**, 5667 (1999).
- [85] S. Doniach, S. Engelsberg, Low-Temperature Properties of Nearly Ferromagnetic Fermi Liquids, *Phys. Rev. Lett.*, **17**, 750 (1966).

-
- [86] T. Moriya, Spin Fluctuations in Nearly Antiferromagnetic Metals, *Phys. Rev. Lett.*, **24**, 1433 (1970).
- [87] P. S. Riseborough and S. G. Magalhaes, Spin-Excitons in Heavy-Fermion Semimetals, *J. Magn. Magn. Mater.*, **400**, 3 (2016).
- [88] B. Gorshunov, N. Sluchanko, A. Volkov, M. Dressel, G. Knebel, A. Loidl, S. Kunii, Low Energy Electrodynamics of SmB₆, *Phys. Rev. B*, **59**, 1808 (1999).
- [89] M. Z. Hasan, C. L. Kane, Colloquium: Topological Insulators, *Rev. Mod. Phys.*, **82**, 3045 (2010).
- [90] D. Xiao, W. Zhu, Y. Ran, N. Nagaosa and S. Okamoto, Interface Engineering of Quantum Hall Effects in Digital Transition Metal Oxide Heterostructures, *Nat. Commu.*, **10**, 1038 (2011).
- [91] L. Fu, C. L. Kane, E. J. Mele, Topological Insulators in Three Dimensions, *Phys. Rev. Lett.*, **98**, 106803 (2007).
- [92] F. Lu, J. Z. Zhao, H. Weng, Z. Fang, and X. Dai, Correlated Topological Insulators with Mixed Valence, *Phys. Rev. Lett.*, **110**, 096401 (2013).
- [93] D. J. Kim, J. Xia, and Z. Fisk, Topological Surface States in the Kondo Insulator Samarium Hexaboride, *Nat. Mat.*, **13**, 466 (2014).

CHAPTER 2

INSTRUMENTATION AND EXPERIMENTAL PROCEDURE

2.1 Introduction

All the measurements described in this thesis were carried out at the third-generation synchrotron light sources, including Helmholtz-Zentrum Berlin (BESSY II), Swiss Light Source (Paul Scherrer Institute), and Diamond Light Source (DLS).

Conventional lab-based photoelectron spectrometers utilize light from x-ray tube sources or Helium discharge lamps. In a typical x-ray tube, energy of the emitted photons corresponds to the characteristic emission line of the target anode. Electrons emitted by a heated-filament cathode are incident onto an anode target (typically, aluminum (Al) or magnesium (Mg)), which is kept at a high voltage (5,000 – 20,000 V). Inelastic scattering of the incident electrons results in a Bremsstrahlung radiation background. In addition to this, core-level electrons will be ejected from the anode creating electron-holes, which are then filled by the electrons from higher-lying energy levels. The latter relaxation process will result in intense characteristic x-ray emission peaks with the energies corresponding to the difference between the higher-lying electron and the lower-lying electron-hole subshells. For example, a transition from the $2p$ level to the $1s$ level in Mg will result in x-rays with energy centered at 1253.6 eV (Mg $K\alpha$ line), while the same type of transition in Al will result in x-rays with energy centered at 1486.6 eV (Al $K\alpha$ line).

In order to obtain monochromatic light, which is often necessary for high-resolution PES experiments, reflection-grating monochromators are often used for the photon energy

range between a few eV and the soft x-rays, while crystal monochromators with lattice spacing comparable to the photon wavelengths are necessary for hard x-rays.

Luminosity and brilliance of the x-ray source are important factors in any PES experiment. Since the x-ray photoionization cross-sections are low, (especially for photon energies in the tender and hard x-ray regimes), high photon flux may be necessary for achieving meaningful photoelectron yield at the detector. In 1948, synchrotron radiation was observed [1] in a particle physics experiment, and it was soon realized that this ‘parasitic’ radiation can be used as a powerful spectroscopic tool with a wide range of photon energies. First synchrotron radiation experiments were carried out at the high-energy particle physics accelerators, in the ‘parasitic’ mode. These are sometimes referred to as the ‘first-generation’ synchrotron light sources. Following these first experiments, and in order to enhance the photon energy tunability, beam brilliance, stability, and energy resolution, specially-dedicated second- and third-generation synchrotron radiation storage rings were designed specifically for x-ray science.

In the second-generation synchrotron sources, synchrotron radiation is generated by the relativistic electrons (or positrons) moving close to the speed of light in a storage ring, and maintained in their orbit with help of bending magnets designed to curve the electron trajectories [2]. The characteristics of the light produced by such storage rings are high photon energy tunability (from infrared to hard x-rays), high beam brilliance, pulsed time structure, and stable photon flux.

In the third-generation synchrotron sources, insertion devices, such as undulators and wigglers [3,4] are utilized to increase the photon flux. Wigglers and undulators consist of two long (several meters) periodic arrays of permanent magnets that are placed in the

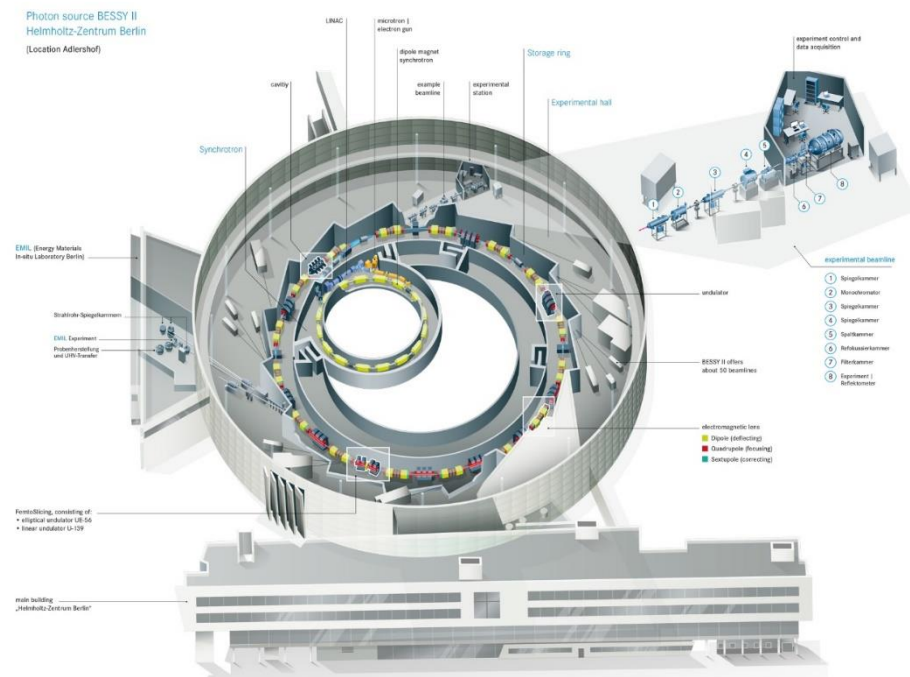


Figure (2.1) – Schematic illustration of the BESSY II storage ring located in Berlin, Germany (adopted from reference [5]).

straight sections of the storage ring. As the electrons travel through these insertion devices, they are forced to oscillate by the alternating magnetic fields. As a result of these undulations, intense and well-focused electromagnetic radiation is produced in the forward direction.

2.2 BESSY II synchrotron radiation source at the Helmholtz-Zentrum Berlin (Germany)

BESSY II is located at the Helmholtz-Zentrum Institute for Materials and Energy in Berlin, Germany, and was the first third-generation synchrotron radiation source in Germany, featuring a storage ring of 240 m in circumference, with electron energy of 1.7 GeV, resulting in 300 mA ring current [5]. The BESSY II storage ring consists of thirty-two deflecting magnets and hosts more than fifty beamlines operating in different areas of x-ray science, as of 2019.

The BESSY II storage ring was designed to provide maximum flux in the VUV and soft x-ray regimes, however several hard x-ray beamlines are currently operational, although with diminished photon flux. All the facilities are available through a competitive peer-review proposal system for research in both academia and industry, and in a wide variety of fields both scientific and industrial areas, including condensed matter physics, materials science, chemistry, biology and life sciences.

All the photoemission measurements described in Chapter 4 of this thesis were carried out at the ‘One-Cubed’ endstation, located at the UE112_PGM-2b-1³ undulator beamline at BESSY II. The beamline facilitates a photon flux of 10^{13} photons per second per 0.1% BW per 0.1 A, and the photon energy can be tuned from 4 eV up to 200 eV, with the resolution of about 1 meV for photon energies of less than 100 eV. The elliptically polarized undulator, which is the insertion device for this beamline, facilitate full polarization control, linear as well as circular. The four-axis (three translational and one rotational) sample manipulator is equipped with a ³He cryostat, which facilitates sample temperatures down to 1 K. The electrostatic electron analyzer (VG Scienta R4000) facilitates kinetic energy resolution of approximately 1 meV. Due to the combined resolution of both the excitation source (1 meV) and the electron energy analyzer (1 meV) as well as the lowest achievable sample temperature (1 K), the endstation is called ‘One-Cubed’ [6]. The unique experimental capabilities facilitated by the One-Cubed endstation at BESSY-II, as described above, were critical for the feasibility of our experiments on SmB₆ (Chapter 4). In particular, the combined energy resolution of less than 3 meV, as well as the ability to cool the sample down to below 5 K was required to observe the in-gap states within the bulk hybridization gap (see chapter Chapter 4 for details).

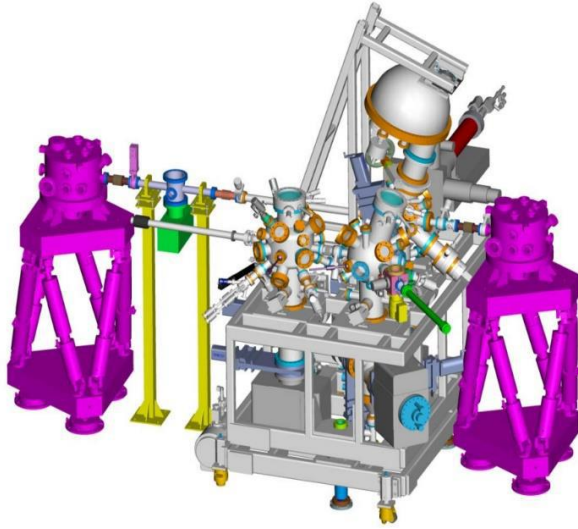


Figure (2.2) SX-ARPES endstation at the ADDRESS beamline of the SLS (adopted from reference [10]).

2.3 Swiss Light Source at the Paul Scherrer Institute (Villigen, Switzerland)

The Swiss Light Source (SLS), located at the Paul Scherrer Institute (PSI) in Villigen, Switzerland, is a third-generation 2.4 GeV synchrotron radiation source with a storage-ring circumference of 288 meters, facilitating 400 mA of beam current [7]. SLS currently (2019) has twenty-two beamlines in user operation, providing a wide variety of x-ray, ultraviolet and infrared techniques for a broad range of scientific research, both in academia and industry.

SLS also utilizes undulators, wigglers, and monochromators to produce intense, focused monochromatic x-rays with tunable photon energy and polarization (both linear and circular). SLS is optimized for the ultraviolet and soft x-ray ranges, providing a photon flux of $\sim 10^{13}$ photons per second per 0.4 Å, and has a stable beam current of 400 mA with continuous charge refilling (top-up mode operation) [8] to increase the beam lifetime.

The electron beam in the storage ring is stabilized by 350+ magnets that focus and reaccelerate the electron bunches. SLS accelerator currently has the narrowest electron beam compared to any other synchrotron facility. ADDRESS beamline is a high-resolution

undulator beamline at the SLS that is optimized for performing angle-resolved photoelectron spectroscopy (ARPES) measurements and resonant inelastic x-ray scattering (RIXS) measurements in the soft x-ray regime [9].

The photon energy range of the ADDRESS beamline can be tuned from 300 eV to 1600 eV, which covers most of the $L_{3,2}$ and $M_{5,4}$ absorption thresholds for the transition- and rare-earth metal elements. This enables resonant photoemission spectroscopy experiments, in which valence-band photoionization cross-sections of the above-mentioned elements are enhanced via resonant excitation. We utilize the Ni L_2 resonant photoemission in our valence-band measurements of the $\text{LaAlO}_3/\text{NdNiO}_3$ [111] heterostructure, as described in Chapter 5.

The total experimental energy resolution ($E/\Delta E$) of the beamline is more than 33,000 at 1 keV photon energy. The photon flux is between 3×10^{11} and 1×10^{13} photons per second per 0.01% BW at 1 keV photon energy. The vertical \times horizontal FWHM x-ray spot size on the sample is approximately $10 \mu\text{m} \times 73.6 \mu\text{m}$ [10]. The photoelectron analyzer has an angular resolution of 0.07° and the total experimental energy resolution of <5 meV. The total experimental resolution is therefore limited by the energy resolution of the beamline, which for our experiments was estimated at 111 meV. The entrance slit size of the analyzer has an angular acceptance angle of 16° .

For typical normal-emission-geometry experiments, the x-ray beam is incident on the sample at a grazing angle of 20° and makes a fixed angle of 70° with the energy analyzer direction. The six-axis sample manipulator is equipped with a liquid He flow cryostat with a minimum achievable cryogenic temperature of approximately 10 K.

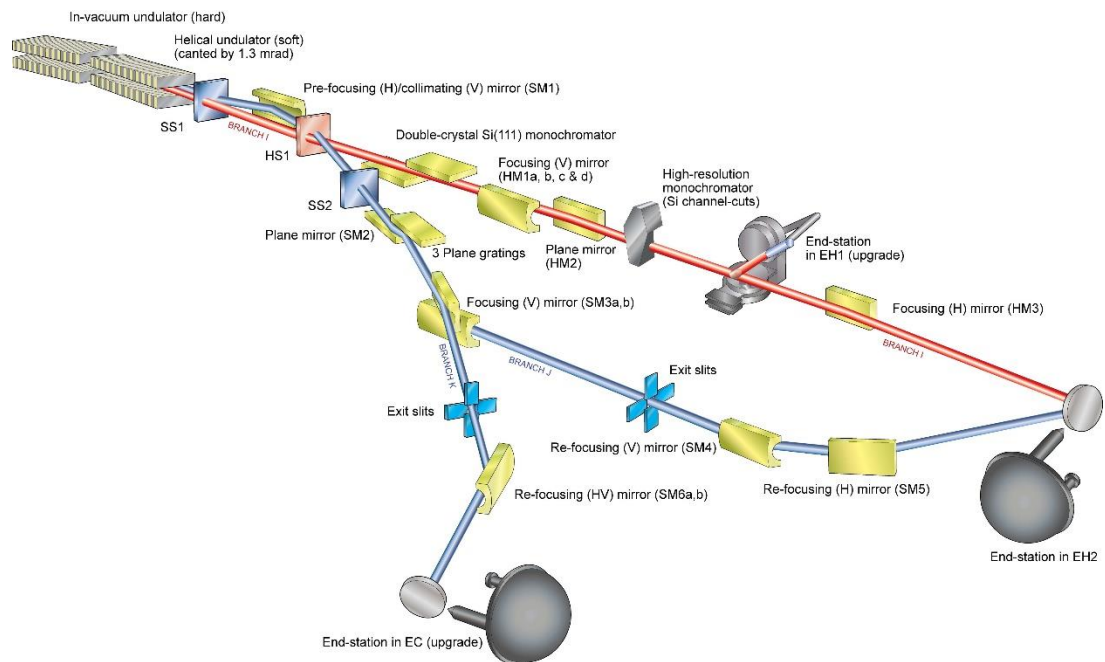


Figure (2.3) – Schematic illustration of beamline I09 at the Diamond Light Source (adopted from references [11,12]).

2.4 Diamond Light Source (Oxfordshire, United Kingdom)

The Diamond Light Source (DLS) is located at the Harwell Science and Innovation Campus in Didcot, Oxfordshire, and is the largest third-generation synchrotron facility in the UK. It has a circumference of 560 m, and is optimized to produce high-brilliance radiation in the infrared, VUV and x-ray regimes. The storage ring is equipped with 48 bending magnets and, as any other third-generation synchrotron facility, DLS utilizes insertion devices, such as wigglers and undulators. The storage ring circulates electrons with the energy of 3 GeV, with a maximum beam current of 300 mA [11].

Currently, DLS hosts about forty beamlines, performing research in a wide variety of disciplines, including various branches physical, chemical, environmental, and life sciences. Beamline I09 is dedicated to surface and interface structural analysis using PES,

near-edge x-ray absorption fine structure (NEXAFS), x-ray standing wave (XSW), and x-ray photoelectron diffraction (XPD).

A unique combination of two canted undulators installed at the beamline provides photons with energies both in the soft x-ray regime (100 - 2100 eV) as well as the hard x-ray regime (2.1 - 20 keV). The vertical \times horizontal x-ray spot size on the sample measures approximately $20 \mu\text{m} \times 40 \mu\text{m}$ (FWHM). A five-axis cryogenic manipulator operated with the flow of liquid Helium facilitates sample temperatures down to 50 K [12]. The Scienta EW4000 electrostatic analyzer operates in both transmission and angular modes, with a wide electron acceptance angle of approximately 60° . The angle between the soft x-ray beam and the analyzer is 87° , and the angle between the soft and hard x-ray beams is 6° .

For our measurements of the $\text{LaAlO}_3/\text{NdNiO}_3$ [111] heterostructure (see Chapter 5) we utilized the hard x-ray branch of the I09 beamline, tuning the photon energy to 6.45 keV. At this energy the IMFP of the valence-band photoelectrons electrons was estimated to be approximately 85 \AA , thus allowing to directly probe the electronic properties of the entire sample and facilitating a straightforward comparison of the experimental data to theory. The kinetic energy of the Fermi level was determined in-situ with a high-statistics measurement on a clean sputtered thin-film Au sample, thus allowing for an accurate calibration of the binding energies.

The total experimental energy resolution was limited by the energy resolution of the hard x-ray beamline, which was estimated at approximately 240 meV by carrying out the Fermi-edge measurements on a clean sputtered gold film at room temperature. The measured Fermi edge was analyzed by fitting the lineshape with a convolution of the

Fermi-Dirac function and a simple Gaussian peak, representing broadening due to the total experimental resolution (see Chapter 3 for details).

References Cited in Chapter 2

- [1] F. R. Elder, R. V. Langmuir, and H. C. Pollock, Radiation from Electrons Accelerated in a Synchrotron, *Phys. Rev.*, **74**, 52 (1948).
- [2] Shigemasa Suga, Akira Sekiyama, Photoelectron Spectroscopy, (Springer, New York, 2014).
- [3] S. Krinsky, Undulators as Sources of Synchrotron Radiation (1983).
- [4] G. Brown, K. Halbach, J. Harris, and H. Winick, *Nuclear Instruments and Methods in Physics Research*, **208**, 65 (1983).
- [5] https://www.helmholtz-berlin.de/quellen/bessy/elektronenspeicherring/index_en.html
- [6] https://www.helmholtz-berlin.de/pubbin/igama_output?modus=einzel&sprache=en&gid=1651&typoid=50740
- [7] <https://www.psi.ch/sls/about-sls>
- [8] A. Ludeke and M. Munoz, in European Particle Accelerator Conference (Proceedings of EPAC, France, 2002), p. 721.
- [9] V. N. Strocov, T. Schmitt, U. Flechsig, T. Schmidt, A. Imhof, Q. Chen, J. Raabe, R. Betemps, D. Zimoch, J. Krempasky, X. Wang, M. Grioni, A. Piazzalunga, and L. Patthey, High-Resolution Soft X-ray Beamline ADRESS at the Swiss Light Source for Resonant Inelastic X-ray Scattering and Angle-Resolved Photoelectron Spectroscopies, *J. Synch. Radi.*, **17**, 631 (2010).
- [10] <https://www.psi.ch/sls/adress/adress>
- [11] <https://www.diamond.ac.uk/Science/Machine.html>
- [12] <https://www.diamond.ac.uk/Instruments/Structures-and-Surfaces/I09/status.html>

CHAPTER 3

DATA ANALYSIS METHODS

3.1 Introduction

In this chapter we will review some basic data analysis methods, which are routinely utilized for post-processing of photoemission spectroscopic data and are instrumental for accurate interpretation and analysis. We will also briefly describe a new method developed by us, which is instrumental for the interpretation of ARPES data and direct comparison of such experimental data to theoretical band-structure calculations.

As was explained in Chapter 1, typical PES spectra are modulated by experimental artefacts, and thus data post-processing and analysis procedures are usually necessary in order to account for the presence of such effects. For example, the PES spectra will always be modulated by an inelastic background caused by secondary electrons, which needs to be removed prior to any meaningful peak-fitting and analysis. As another example, typical experimental core-level peaks will always be affected by both lifetime and resolution-related broadening effects that produce Voigt profiles, which are convolutions of Gaussian and Lorentzian lineshapes. As a result, sophisticated analytical peak-fitting procedures are often required to fit multiple-peak spectral features and to accurately extract the positions,

widths (both Gaussian and Lorentzian components), and intensities of individual lineshapes. For the ARPES measurements, datasets usually contain large multi-dimensional arrays of data, containing values of photoemission intensities as functions of various experimental degrees of freedom, such as photoelectron momentum components in three dimensions (k_x , k_y , k_z), binding energies, incidence angles, and physical position/rotation of the sample. Such multi-dimensional datasets often require post-processing using various procedures, such as normalization, background subtraction, and linear offsets, which could be different for each of the dimensions (degrees of freedom).

In order to carry out typical post-processing and analysis of large arrays of data in an efficient and consistent way, it is instrumental to have the analytical tools that alleviate the need to repeat the same data analysis procedures multiple times, by enabling self-consistent automated processing. Hence, as a part of this thesis, we developed a comprehensive MATLAB-based spectroscopic data analysis package with a user-friendly graphical user interface (GUI) for such automated post-processing analysis. Below, we describe some of the key features that were implemented in this software package. At the end of the section, we describe a new method for comparing ARPES data to theoretical density functional theory (DFT) calculations, wherein the output of the DFT calculations is used for simulating APRES data for various experimental geometries and photon energies. The two above-mentioned components of our software are shown in Figures (3.1 a-b) below.

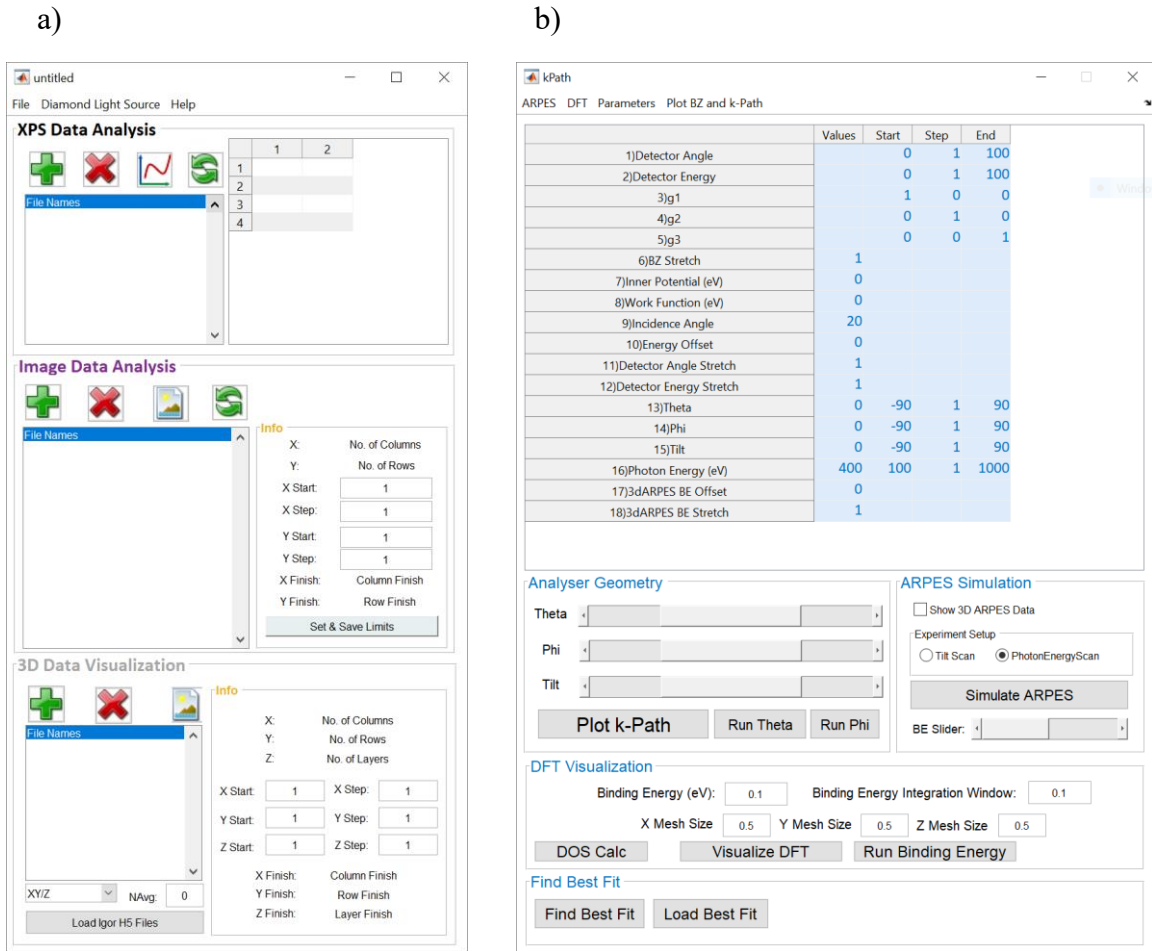


Figure (3.1) – a) Data analysis and post-processing GUI designed in MATLAB. b) k-Path software for simulating the ARPES data using theoretical DFT calculations.

3.2 X-ray photoelectron spectroscopy (XPS) GUI in MATLAB

Figure (3.1 a) shows the MATLAB GUI interface developed for comprehensive photoemission spectroscopic data post-processing and analysis. The software is comprised of three modules: XPS, ARPES and 3D data analysis. Typical features in the XPS module include the Shirley background subtraction, Fermi-Dirac function fitting, XPS peak fitting, normalization, *etc.*

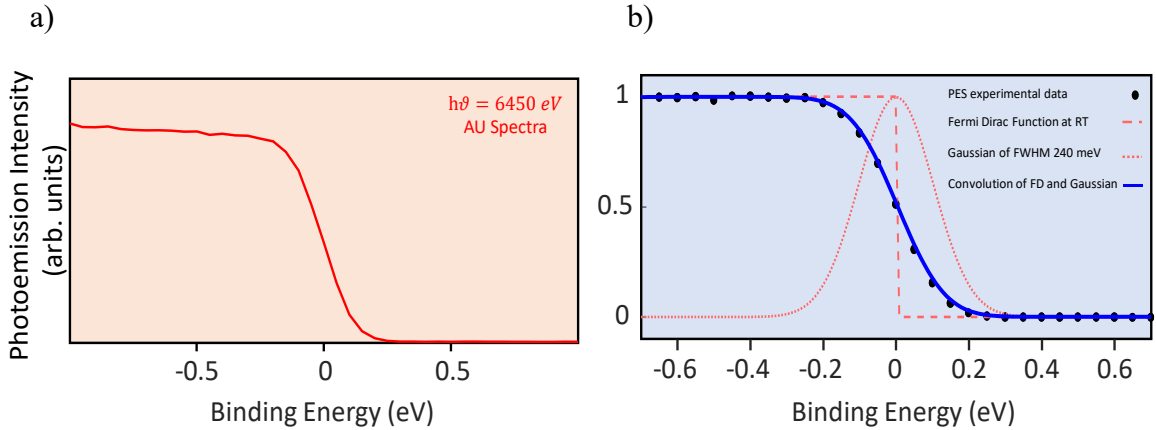


Figure (3.2) – a) Au valence-band spectrum at room temperature and at photon energy of 6450 eV. b) Au valence band spectrum shown with dot black circles at room temperature and photon energy of 6450 eV. Fermi-Dirac distribution is also shown with the dashed red line at room temperature which doesn't fit to the VB spectra of Au at RT. The Gaussian function with a FWHM of 240 eV is also shown with the small red dashed line. Blue curve which fits the experimental data is the convolution between the Fermi-Dirac distribution at RT and the Gaussian function of FWHM of 240 eV, hence the experimental resolution can be determined to be about 240 eV.

Here, we provide two basic examples of data treatment and analysis methods we used in this thesis. These techniques are described extensively in Chapters 4 and 5, in the context of specific material systems and measurements.

In Figure (3.2 a) we show an angle-integrated photoemission measurements of a clean sputtered Au film, recorded at a photon energy of 6450 eV (hard x-ray regime) and at room temperature (further details of this experiment are provided in Chapter 5). Since Au is a metal, we expect to observe a Fermi-Dirac distribution for the valence-band (VB) PES spectrum at the Fermi level. In fact, such spectrum of the Au VB-maximum can be used to calibrate the Fermi energy (E_F) in PES measurements. If we fit the experimental spectrum to a Fermi-Dirac function calculated for room-temperature (300 K), one can see that the fit between the theory and experiment is not optimal (see dashed red line in Figure (3.2 b)).

This inconsistency between the experiment and theory arises due to the effects of total energy-resolution broadening in a photoemission measurement, which is comprised of the bandwidth of the incident beam and the energy resolution of the electron analyzer.

The overall experimental resolution can be thus estimated by fitting the experimental data to a convolution of the above-mentioned Fermi-Dirac function, calculated for room temperature, and a Gaussian lineshape with a variable full-width half-maximum (FWHM), to match the experimental data (see solid red line in Figure (3.2 b)). The value of FWHM resulting in the best fit between the experimental and the calculated curves (see solid blue line in Figure (3.2 b)) is a fair measure of the overall instrumental energy resolution, which in this case was estimated to be 240 meV.

The position of the Fermi-Dirac edge extracted from the fitting is a fair measure of the true photon energy of the beam and the E_F . Thus, for samples exhibiting a semiconducting gap, an accurate estimate of the valence-band bandgap ($E_{VB-max} - E_F$) can be inferred. Our HAXPES measurements of the $\text{LaAlO}_3/\text{NdNiO}_3$ [111] heterostructure, described in Chapter 5 of this thesis, reveal the presence of a valence-band bandgap of 265 meV, consistent with theoretical calculations.

Figure (3.3) shows a PES survey of the above-mentioned $\text{LaAlO}_3/\text{NdNiO}_3$ [111] heterostructure, with the VB manifold appearing on the right side of the energy scale (from

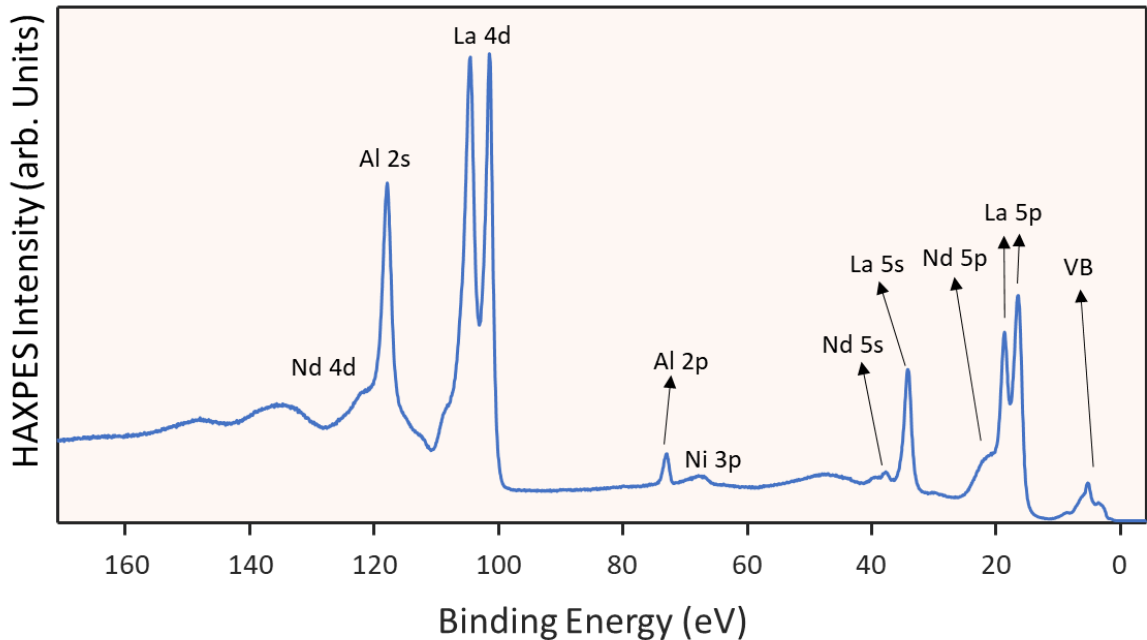


Figure (3.3) – Photoemission spectrum of the material $\text{LaAlO}_3\text{-NdNiO}_3$ [111] at photon energy of 6450 eV and thus probing the entire depth of the sample as evident from photoemission core levels from top layer (LaAlO_3) and the buried layer (NdNiO_3).

-5 to 170 eV). Core-level photoemission peaks from the shallow-lying subshells appear at their corresponding binding energies. It is immediately apparent that the inelastic background appears throughout the entire spectrum, increasing the overall photoemission intensities of each peak asymmetrically on the higher-binding-energy side. Removal of such background, typically accomplished using a method introduced by Shirley [1], enables accurate fitting analysis of the core peaks, as well as more straight-forward analysis of the valence-band structures. As an example of the Shirley-background subtraction, raw (as-measured) angle-integrated valence-band spectrum of SmB_6 , is shown as a solid blue curve in Figure (3.4). A ‘Shirley-type’ background, plotted as a dashed red curve, has been subtracted from the raw data in order to remove spectral asymmetry due to the inelastic

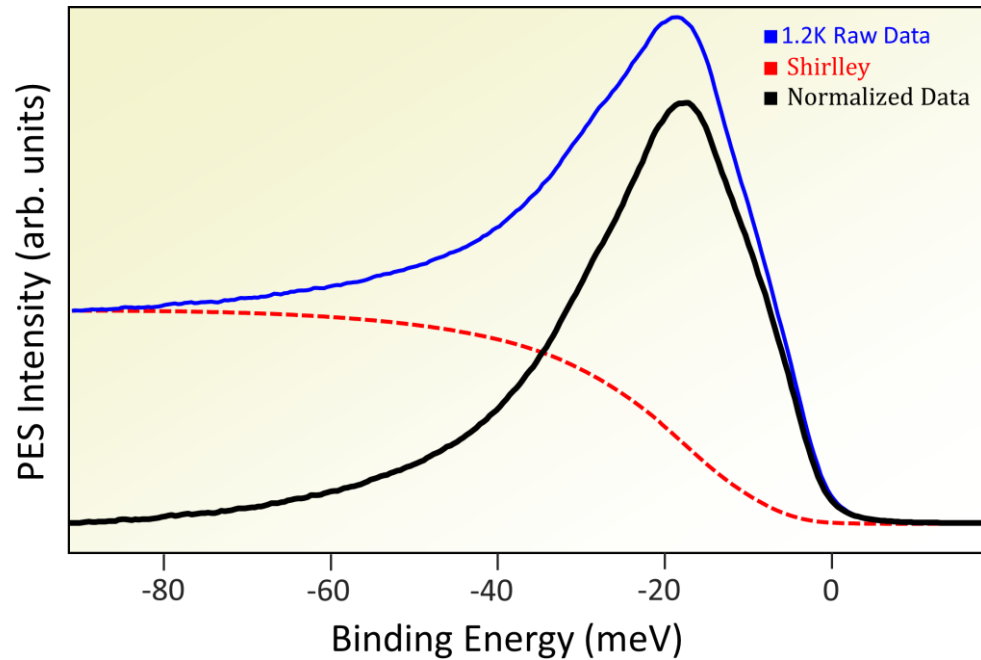


Figure (3.4) – Blue curve shows the angle integrated photoemission spectrum at 1.2 K. Red dashed line is the calculated Shirley background and the Black curve is the spectrum data after Shirley background removal

scattering events, resulting in a solid black lineshape. After such background removal, further processing and analysis of the VB spectrum becomes accessible, including peak-fitting and determination of the Fermi velocity, as described in detail in Chapter 4.

For SmB_6 , accurate determination of the chemical potential can be a challenging task.

Our VB measurements of SmB_6 were carried-out at two different temperatures (1.2 K and 20 K). By calculating the Fermi-Dirac distribution functions for these two temperatures, convolving them with Gaussian lineshapes with the FWHM of 3 meV (corresponding to the overall experimental energy resolution), and then multiplying the results by the corresponding experimental VB spectra, we can identify the chemical potential of SmB_6 , as described below.

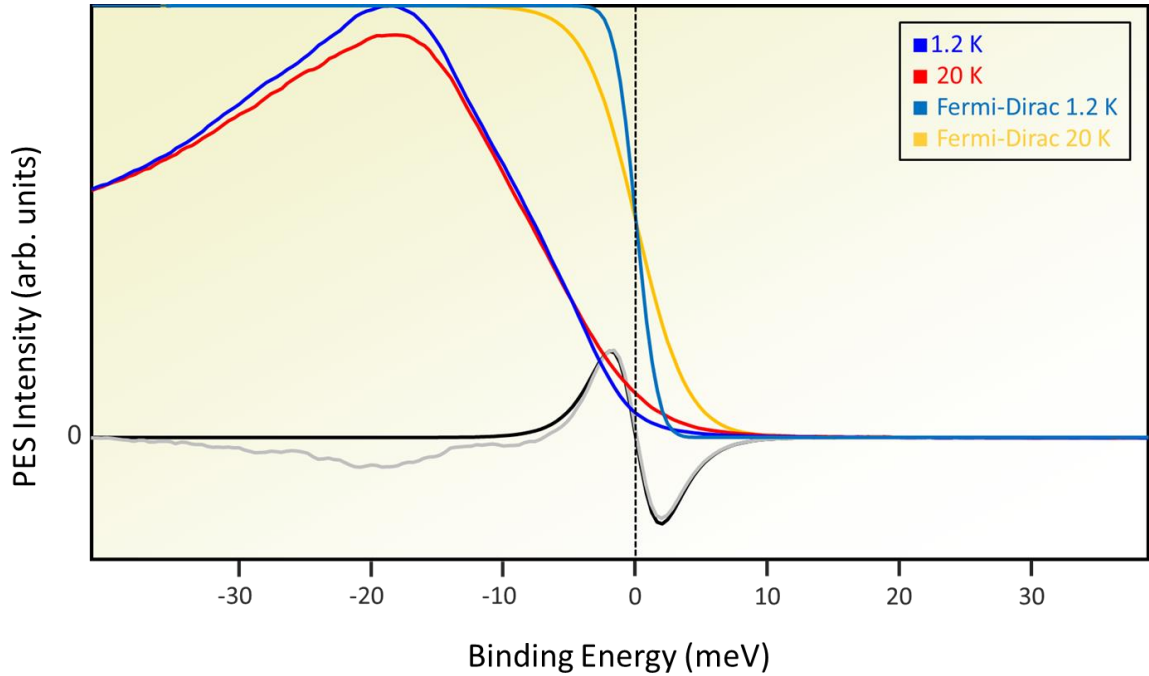


Figure (3.5) – Photoemission spectrum of the material SmB_6 at 1.2 K (blue curve) and 20 K (red curve). Fermi Dirac functions convoluted with a Gaussian of FWHM of 3 meV is also shown. Difference between the F-D functions is shown with the black color curve. Difference between the F-D function multiplied by the experimental data is also shown with the gray color. At Fermi difference between black-color curve and gray-color curve will be minimum.

In Figure (3.5), the difference between the low- and high-temperature Gaussian-broadened Fermi-Dirac functions is plotted with a solid black curve. The solid grey curve represents the difference between low-temperature Gaussian-broadened Fermi-Dirac function multiplied by the VB spectrum at 1.2 K and the high-temperature Gaussian-broadened Fermi-Dirac function multiplied by the VB spectrum at 20 K. At the chemical potential, the difference between the gray-color solid line and the black-color solid line should be minimized, and therefore the chemical potential can be determined by scanning the broadened FD function along the energy scale and then performing the above-mentioned procedure at each point of the photoemission data close to the rising edge of the

VB spectrum. All the above-mentioned post-processing and analytical procedures are available in our GUI software package.

The ARPES and 3D-data analysis modules of the software contain a suite of all data- and image-processing tools, as well as data-analysis routines necessary for the post-processing and interpretation of ARPES data. As an illustrative demonstration of some of the features of this module, here, we discuss an E_B - k_x ARPES map recorded for the above-mentioned $\text{LaAlO}_3/\text{NdNiO}_3$ [111] heterostructure along the K' - Γ - K high-symmetry direction (see Fig. 5.3 (a) in Chapter 5). Careful examination of the data reveals that the experimental band-structure contains both dispersive and non-dispersive (nearly-flat) bands. In order to enhance the relative intensity of the dispersive bands, we could perform a common data-analysis procedure, wherein the image is normalized by the binding-energy-averaged and the k -averaged spectra. This results in the suppression of the intensity for most of the flat bands [2]. The result is shown in Figure (5.4), where dispersive bands are now more apparent to the eye due to the normalization procedure described above.

The ARPES software module also facilitates all the relevant angle-momentum and photon-energy-momentum conversions in the nearly-free-electron picture described earlier in Chapter 1. All other relevant post-processing procedures, such as normalization, rotation, energy distribution curves (EDC), momentum distribution curves (MDC), *etc.*

could be applied in parallel to all spectra and 2D slices. Thus, the 3D data analysis module facilitates straightforward interpretation of 3D ARPES datasets and provides user-friendly procedures for extracting relevant processed, normalized and energy/momentum-calibrated spectra and maps from the (k_x, k_y, E_B) and/or $(k_x, h\nu, E_B)$ data arrays.

Here, we will briefly describe a method we developed to facilitate a direct comparison between the experimental ARPES data and theoretical DFT band-structure calculations. As was mentioned in Chapter 1, the perpendicular component of the photoelectron final momentum in the nearly-free-electron picture could be obtained via Equation (1.23). This value sets the limit for the radius of an arc traversed by the k_f vector in the extended BZ picture for a particular measurement, wherein the length of the arc is determined by the analyzer's acceptance angle (Figure (3.6)). The orientation of the arc is determined by the experimental geometry, namely the relative orientation of the analyzer and the sample. The simplest arc in k -space can be obtained in the normal-emission experimental geometry. In this experimental configuration, by varying the photon energy one can tune the radius of the arc, thus scanning the perpendicular component of the final photoelectron momentum (k_{\perp}) in k -space.

By fixing the photon energy and, thus, the magnitude of k_{\perp} at a set value, one could resolve the y -component of the momentum (k_y) by rotating the sample along the polar tilt

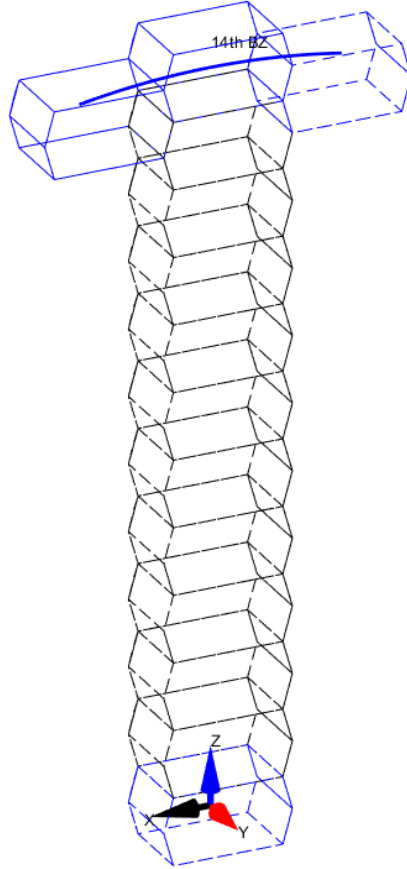


Figure (3.6) – Schematic illustration of linecut in momentum space for a normal emission geometry measurement at photon energy of 600 eV and with analyzer's acceptance angle range of 20° for the material WP_2 . The linecut highlights the 14th BZ in the extended-BZ scheme which covers three adjacent BZs.

axis (by changing the angle β), as defined in Figure (1.3) (Chapter 1). As a result, a section of the surface of a sphere with a fixed radius k_\perp could be obtained in the extended BZ picture, by scanning the arc in k -space around the tilt axis.

From the discussion above, it is evident that a typical ARPES scan is not flat in momentum space, but rather has a curvature due to the fixed value of the photon energy, which determines the radius of the curvature, or k_\perp . This consideration becomes important when one attempts to compare experimental ARPES scans to theoretical band-structure

and Fermi-surface calculations, which are usually represented by flat cuts in momentum-energy space. The curvature effects are specifically important for wide-acceptance-angle electrostatic analyzers, where the detector angle may span several BZs. At high excitation energies, and thus large values of k_{\perp} , this effect becomes pronounced even for electrostatic analyzers with smaller acceptance angles.

In all the above-mentioned cases, the effects of the curved momentum-space path are crucial for a meaningful comparison of the experimental results to theoretical band-structure calculations. For this specific purpose, we have developed a software module which facilitates simulations of ARPES measurements in any arbitrary experimental geometry and at any arbitrary excitation energy using imported theoretical band-structure data. A typical band-structure calculation, such as a DFT calculation, could be arranged in a four-dimensional data set, as described below. If b_1 , b_2 and b_3 represent the reciprocal lattice unit vectors, one could form a parallelepiped using these unit vectors. The BZ will be the Wigner-Seitz cell of this manifold, thus, in order to obtain a complete band dispersion in k -space it suffices to have the band information inside this volume. By using a fine mesh, it is then possible to obtain band energies in each one of the mesh points in this parallelepiped for various band indexes. These values comprise the fourth dimension of the 4D dataset, where the first three dimensions are the coordinates of the bands with specific energies in the parallelepiped. Thus, if the path of the final photoelectron

momentum vector resulting from a detector, tilt, or photon-energy scan is well-defined, one could plot the k -space band dispersion for any experimental geometry and/or photon energies. Furthermore, the topology of the bands in k -space in the first BZ for different energies and in all three dimensions in momentum space could also be visualized. More details regarding this method are provided in Appendix A.

References Cited in Chapter 3

- [1] D. A. Shirley, High-Resolution X-Ray Photoemission Spectrum of the Valence Bands of Gold, *Phys. Rev. B*, **5**, 4709 (1972).
- [2] A. X. Gray, C. Papp, S. Ueda, B. Balke, Y. Yamashita, L. Plucinski, J. Minár, J. Braun, E. R. Ylvisaker, C. M. Schneider, W. E. Pickett, H. Ebert, K. Kobayashi and C. S. Fadley, Probing Bulk Electronic Structure with hard X-ray Angle-Resolved Photoemission, *Nat. Mat.*, **10**, 759 (2011).

CHAPTER 4

EFFECTS OF SPIN EXCITONS ON THE SURFACE STATES OF SmB_6

4.1 Introduction

As we described in Chapter 1, SmB_6 is a Kondo insulator in which a ~ 21 -meV hybridization gap in the bulk density of states forms for temperatures below the coherence temperature of about 100–150 K [1, 2]. The small magnitude of the gap is due to a renormalization by the strong Coulomb interactions between the Sm $4f$ electrons. Bulk-impurity states pin the chemical potential within the gap. Thus, the bulk properties are characterized by a thermal activation in the resistivity and specific heat, with an activation energy of about 4 meV [3-5]. However, at temperatures on the order of 4 K, the resistivity shows a plateau [6, 7] indicative of the presence of surface states at the Fermi energy [8-11].

The material SmB_6 has been the focus of much renewed interest ever since it was proposed that it is a topological Kondo insulator [12, 13]. Doping SmB_6 with magnetic impurities has been shown to increase the low-temperature resistivity, whereas nonmagnetic impurities do not change the resistivity saturation [10]. The insensitivity to nonmagnetic impurities suggests that the electronic surface states are protected from $k \rightarrow -k$ scattering by a spin texture and time-reversal symmetry as expected for a topological insulator. Furthermore, through spin-resolved ARPES measurements [14] a spin texture, which is expected for a topological insulator, has indeed been observed in the above-Fermi-surface states, although this observation has been subject of a debate [15]. The existence of metallic surface states found via transport measurements is also consistent with the

results of magnetic torque [16] and ARPES experiments [17-19], although alternate three-dimensional interpretations have been proposed [20, 21].

ARPES measurements reveal that the measured surface Fermi surface consists of three sheets; a small sheet around the Γ point, and elliptical sheets located around the X and Y points. ARPES measurements [22] have also identified an in-gap peak due to the surface states at an energy of about -5 meV.

Surface Fermi-surface velocities as large as $v_F \approx 8.45 \times 10^5$ m/s have been observed in quantum oscillation measurements, while ARPES measurements yield $v_F \approx 4.0 \times 10^4$ m/s, which are an order of magnitude lower. Both values are orders of magnitudes larger than those obtained from theory [23, 24] ($v_F \sim 4.5 \times 10^3$ and $\sim 7.6 \times 10^3$ m/s) and from transport measurements, which yield $v_F \approx 7 \times 10^2$ m/s [25]. The large discrepancies between the values of the surface Fermi velocities have led to the speculation that the surface may have undergone a phase transition in which the $4f$ ions localize, leaving the surface states to be dominated by conduction electrons with light masses [26].

Here we present the results of high-resolution angle-integrated photoemission spectroscopy measurements of SmB_6 , which indicate the presence of a V-shaped density of states within the bulk gap. We estimate that the Weyl point and the chemical potential reside within the bulk gap and have very similar energies. This points to the existence of a heavy band of surface electronic states, as has been predicted by theory and inferred from low-temperature transport measurements [27]. By examining the difference of the integrated spectra at temperatures of 20 and 1.2 K, we find that the density of states exhibits a low-temperature peak located at about -9 meV. The difference spectrum shows that this feature has its intensity derived from the X and Y points and is of surface origin. We identify

this peak as a resonance in the surface electronic density of states caused by the coupling of the surface states to the in-gap spin-exciton excitations [28].

As was described in Chapter 1, spin excitons are magnetic excitations that occur in the gap of paramagnetic Kondo insulators and have been observed in bulk SmB_6 with excitation energies of 12 to 14 meV [29-31]. The intensity of the spin-exciton peak seen in neutron scattering experiments [32] increases and the peak width decreases with decreasing temperature. At the temperature of 25 K, the intensity is approximately half of its value at liquid-helium temperatures, while its line width is saturating at a value comparable to the experimental resolution [32]. Supporting evidence for the exceptionally long lifetime of the spin exciton has been provided by Raman scattering experiments [33] which see a $q \sim 0$ feature at 16 meV with a width of 0.5 meV in an Al flux-grown SmB_6 sample at $T = 15$ K. The narrow linewidth of the spin exciton is caused by the absence of an electron-hole pair decay channel within the bulk hybridization gap. A shift of the peak from 13 meV in the bulk to 9 meV at the surface would indicate that the surface states are close to a quantum critical point [34].

The existence of large-amplitude, low-frequency spin-flip scattering at the surface would also result in the surface states not being completely protected from back-scattering and gives rise to a resonant peak in the low-temperature surface electronic density of states. This spin exciton-induced resonance in the surface electronic spectrum is expected to occur at low-temperatures at a sharp defined energy but, due to the requirement of conservation of crystal momentum combined with the narrow spin exciton dispersion, should be spread over a finite range of crystal momenta. Since the resonance is a many-body effect, it is also

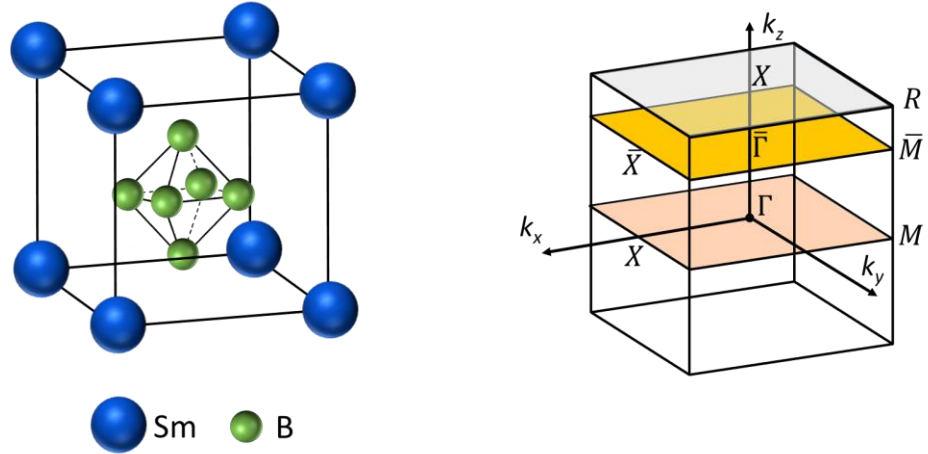


Figure (4.1) – a) Cubic crystal structure of SmB_6 b) Schematic graph of BZ with high symmetry points identified as Γ , X, M, R. The yellow plane highlights the plane probed by ARPES measurements at photon energy of 35 eV in the k_x - k_y plane in momentum space.

expected to have a significantly reduced spectral weight. Therefore, this feature is expected to be most identifiable as the difference between the high-temperature and low-temperature angle-integrated photoemission spectrum.

4.2 Experiment and Results

High-quality SmB_6 crystals were grown using aluminum flux method in a continuous Ar purged vertical high temperature tube furnace [35]. SmB_6 crystallizes in a body centered cubic lattice where Sm ions are located at the corners of the lattice while B_6 octahedra is located at the center of the lattice. Figure (4.1) shows the crystal structure of this compound along with the cubic Brillouin zone (BZ) in the reciprocal lattice with the corresponding high symmetry points.

High-resolution valence-band photoemission measurements were carried out in the normal emission geometry using linearly p -polarized light with photon energy of 35 eV at the 1³ end-station of the BESSY II storage ring of the Helmholtz-Zentrum Berlin (see Chapter 2). The sample was cleaved *in situ* at 1.2 K along the (001) plane and measured in

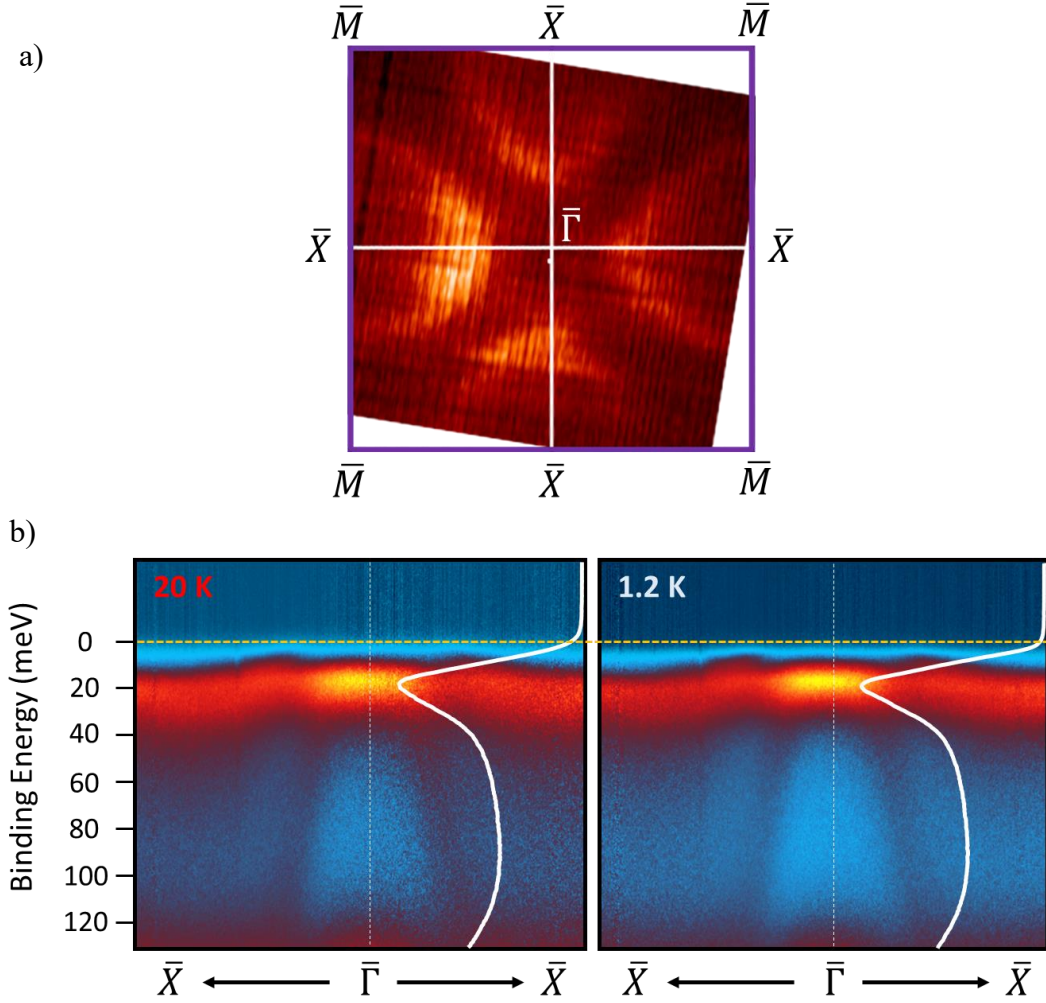


Figure (4.2) – a) ARPES k_x-k_y map at Fermi energy b) ARPES E_b-k_x maps along the high symmetry direction $\bar{X} - \bar{\Gamma} - \bar{X}$ at two different sample's surface temperatures of 1.2 K and 20 K.

an ultrahigh vacuum of 10^{-11} torr at cryogenic temperatures of 1.2 and 20 K. The overall energy resolution was estimated to be about 3 meV. The inner potential is determined to be about 13.5 eV [1]. As a result, at photon energy of 35 eV, final photoelectron momentum will be about 3.5 \AA^{-1} which falls close to the X point between the $\bar{\Gamma}$ point and X point along k_z direction in the third BZ as shown in Figure (4.1 b).

Figure (4.2 a) shows an iso-energetic k_x-k_y ARPES map at the Fermi energy, revealing the Fermi-surface topology in the $\bar{\Gamma}$ plane. ARPES E_b-k_x maps at two different temperatures (1.2 K and 20 K) are shown along the $\bar{X} - \bar{\Gamma} - \bar{X}$ direction in Figure (4.2 b).

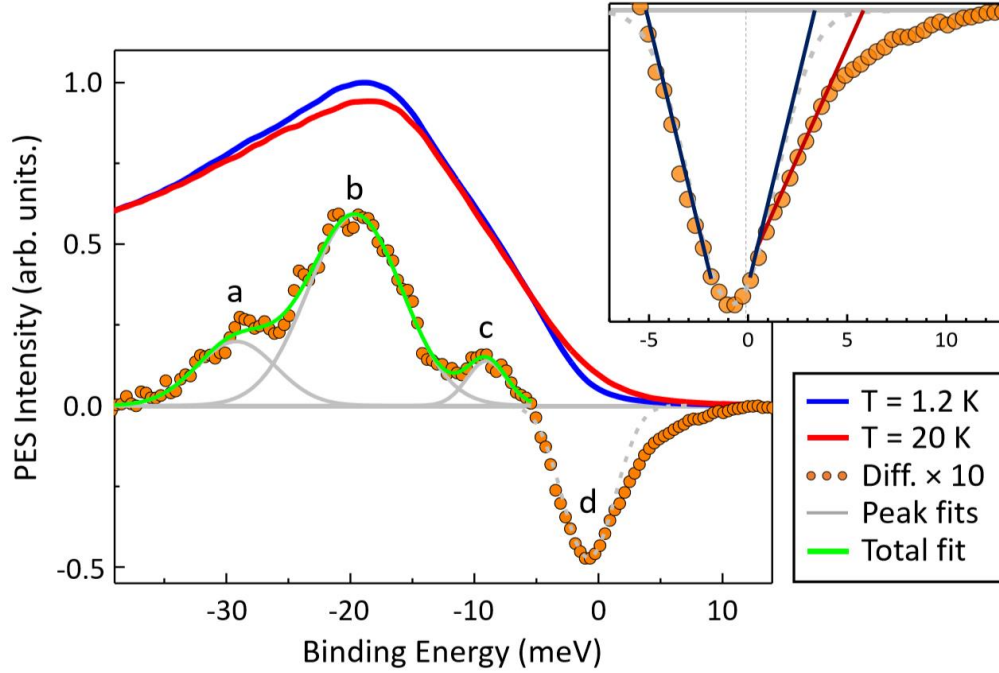


Figure (4.3) – The angle integrated valence-band photoemission spectra measured at the sample temperatures of 1.2 K (blue line) and 20 K (red line). The difference between the spectra at these two temperatures is shown in orange. To enhance the excursions, the difference spectrum has been multiplied by a factor of 10. The inset shows a close-up of the difference spectrum near the Fermi-energy. Spectra were measured along the $\bar{X} - \bar{\Gamma} - \bar{X}$ direction in the BZ and integrated over the entire angular range of the detector ($\sim 30^\circ$).

White curves on the right-hand side of the ARPES E_b - k_x maps, represent the angle-integrated energy distribution curves (EDC) which are strongly-modulated by the matrix element effects. As can be seen from Figure (4.2 b), the intensity of the in-gap feature is derived mostly from the features in the vicinity of the X point.

Figure (4.3) shows the intensity profile of the angle-integrated valence-band photoemission spectra (as also shown with the white-color curves in the angle-resolved maps in Figure (4.2 b)) measured at the sample temperatures of 1.2 K (blue) and 20 K (red). The difference spectrum is shown in orange. To enhance the major features, spectrum has been multiplied by a factor of 10. The three positive peaks below -5 meV, labeled as (a), (b), and (c), were fit with simple Gaussians. Feature (d), near the Fermi energy, has a negative weight and cannot be fit with a single Gaussian line shape.

Feature (a) occurs at the binding energy of -29 meV. The presence of a low-temperature surface feature at this energy is completely unexpected. We note that this feature is separated from the edge of the bulk gap by an energy that roughly corresponds to the spin-exciton energy. This might indicate that the feature is a bulk feature caused by coupling to a spin exciton, however, such a temperature dependence is not expected for a bulk feature. Alternatively, this feature might be attributable to a crystal-field level. However, a corresponding crystal-field feature was not observed in inelastic neutron scattering experiments and would not be expected to be so temperature-dependent.

Feature (b) is a nondispersive peak located at a binding energy of about 20 meV. It is identified as a $4f$ feature at the bottom of the bulk gap caused by the hybridization of Sm $4f$ and Sm $5d$ electronic states. The bulk ARPES of the Kondo insulator SmB_6 has been previously reported [1] and the bulk gap has been observed to form below a characteristic temperature of between 80 and 150 K.

Feature (c) at -9 meV is present at the lower temperature (1.2 K) but is absent at the higher temperature (20 K). This feature is of surface origin and its weight is mainly derived from the vicinity of the X and Y points [21]. Due to its energy, its temperature dependence and its appearance in the angle-integrated spectrum, we attribute this feature to a resonance in the surface electronic density of states caused by the coupling of the surface states to spin-exciton excitations. More specifically, it is assigned to a resonant process involving the filling of the photo-hole at $\omega = -\omega_0$ by an electron in a state just below $\omega = 0$ accompanied by the emission of a spin exciton of energy ω_0 . Because the process involves electrons just below the Fermi energy, the resonant feature depends sensitively on temperature.

Feature (d) centered at -0.8 meV resides within the bulk gap and has a V shape. It can be identified with the conical surface density of states with a minimum that is located at the Weyl point [36]. The peak has been fit (gray dashed-line) with the convolution of a V-shaped density of states and a Gaussian resolution function of the full-width half-maximum of 3 meV (the overall experimental resolution). We note that the shape of feature (d), shown in the inset of Figure (4.3), resembles the differential conductance reported by planar tunneling spectroscopy measurements [36] where the data is of the form of an asymmetric V shape followed by a break, a distinct flattening at +4 meV, which is related to a surface density of states coming from the inequivalent cones located at the Γ and X points and to the coupling to a spin exciton with energy of 4 meV. The straight lines are guides to the eye.

The surface electronic density of states can be estimated by subtracting a Shirley background from the angle-integrated spectrum and then normalizing the area below the Weyl point to unity. By normalizing the area under the Shirley-background-subtracted data, we can effectively obtain the density of states and, hence, the Fermi velocity. For a Weyl-cone, the energy dispersion curve is given by the equation $E = \hbar v_F |\mathbf{k}|$ where v_F is the Fermi velocity. As a result, density of states can be calculated from the equation below:

$$DOS(E) = \frac{A}{(2\pi)^2} \int \delta(E - E(k)) d\mathbf{k} = \frac{A}{2\pi \hbar^2 v_F^2} E \quad (4.1)$$

Hence, from the derivative of the DOS with respect to energy, we can find the Fermi velocity. A is the area of one-unit cell of SmB_6 ($A = a^2$, where a is lattice constant, which is approximately 4.31 \AA).

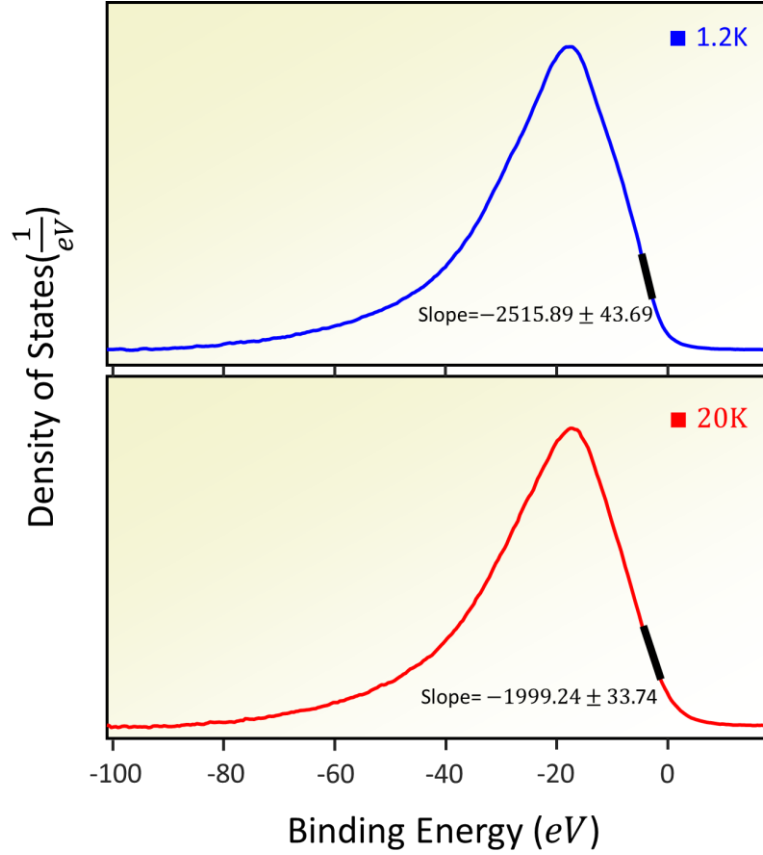


Figure (4.4) – The graph on top, shows the normalized PES spectrum at 1.2 K and the bottom graph shows the normalized PES spectrum at 20 K. Both spectra were first Shirley-background-subtracted and then normalized to unity to the area under the curve. Fermi velocity is calculated by taking the slope of the graphs at the Fermi level, based on Equation (4.2).

Since the intensity of a PES spectrum is given in arbitrary units (such as detector counts), by normalizing the PES spectrum to its area [area = arb. units \times meV] the intensity will be expressed in the units of 1/eV (after normalizing the area underneath the graph to unity). Hence, the slope of such normalized graph will have the units of $1/eV^2$. As a result, the slope of the graph close to the vicinity of the Weyl cone will be equal to

$$Slope = \frac{A}{2\pi\hbar^2 v_F^2} = \Rightarrow v_F = \frac{a}{h} \sqrt{\frac{2\pi}{Slope}} \quad (4.2)$$

Figure (4.4) shows the results of such analysis for the angle-integrated spectra measured at the temperatures of 1.2 K (blue curve) and 20 K (red curve). The estimated Fermi velocity at 1.2 K is approximately 5.2×10^3 m/s, while at a higher temperature of 20

K, the Fermi velocity is estimated to be approximately 5.8×10^3 m/s. These values are compatible with the theoretical values of $v_F = 4.5 \times 10^3$ and 7.6×10^3 m/s, respectively [23, 24].

4.3 Theory

In this section, we will briefly present the key results from the theoretical work presented in this study. An extended description of this work was published in *Phys. Rev B* **94**, 235125 (2016) [37].

In order to make closer contact with experiment, we consider the (unperturbed) Weyl cone to be asymmetric, where the Weyl point is separated from the upper edge of the hybridization gap by an energy, Δ_+ , of only +5 meV and from the lower edge by an energy Δ_- of 18 meV (hence a gap of total width of 23 meV). Since we are interested in the evolution of the surface electronic states for temperatures below 25 K, it seems reasonable to assume that the temperature dependency of the hybridization gap has saturated and thus, Δ_{\pm} , may be approximated by constant values. The values of Δ_{\pm} were chosen to model the experimental data.

The surface Fermi-energy is positioned at an energy $\mu = +2$ meV above the Weyl point (3 meV below the conduction band). This positioning of the surface Fermi energy is consistent with the ≈ 3 meV activation energy observed in bulk experiments [3], which is associated with the bulk impurities that pin the Fermi energy. The existence of these bulk in-gap states has recently been confirmed by Raman scattering measurements [33], which indicate that 1% of Sm vacancies close the gap in the bulk density of states. This vacancy

concentration is in very good agreement with theoretical predictions [38, 39] that suggests that the bulk hybridization gap is closed with only 5% of Sm vacancies [40].

Since the inelastic neutron scattering experiments indicate that the spin-exciton energy $\omega(q)$ has only a weak dispersion [29-32], we shall mainly ignore the dispersion. We shall set the spin-exciton energy as $\omega_0 \sim 8$ meV, which is reduced from the bulk value since, due to reduced coordination number, the surface is expected to be closer to a magnetic instability (QCP).

We calculate the self-energy for electrons in the surface states due to the emission and absorption of spin excitons [28], using the imaginary time Green's functions and then analytically continuing $i\omega_n \rightarrow \omega - i\eta$. At $T = 0$, the self-energy only has a contribution from the fermionic statistics and is evaluated as follows:

$$Re\Sigma(\omega) = \left(\frac{3J'^2}{4Z_0}\right) \left[\left(\frac{\Delta_+ - \Delta_-}{\Delta_+ \Delta_-}\right) + \frac{x_-}{\Delta_+^2} \ln \left| \frac{\hbar(\omega - \omega_0)}{x_- - \Delta_+} \right| - \frac{x_+}{\Delta_+^2} \ln \left| \frac{\hbar(\omega + \omega_0)}{x_+} \right| + \frac{x_+}{\Delta_-^2} \ln \left| \frac{x_+}{x_+ + \Delta_-} \right| \right] \quad (4.3 \text{ a})$$

$$Im\Sigma(\omega) = \left(\frac{3\pi J'^2}{4Z_0}\right) \left[\frac{x_-}{\Delta_+^2} \{\Theta(\Delta_+ - x_-) - \Theta(\omega_0 - \omega)\} + \frac{x_+}{\Delta_+^2} \{\Theta(x_+) - \Theta(\omega_0 + \omega)\} - \frac{x_+}{\Delta_-^2} \{\Theta(\Delta_- + x_+) - \Theta(x_+)\} \right] \quad (4.3 \text{ b})$$

where

$$x_{\pm} = \hbar(\omega \pm \omega_0) + \mu \quad (4.4)$$

and Z_0 is a dimensionless quantity that determines the intensity of the spin-exciton, as explained in Chapter 1:

$$Z_0 = J^2 \left(\frac{\partial \chi^0(\omega)}{\partial \hbar\omega} \right) \Big|_{\omega_0} \sim \frac{2J^2 \hbar\omega_0}{(\Delta_+ + \Delta_-)^3} \quad (4.5)$$

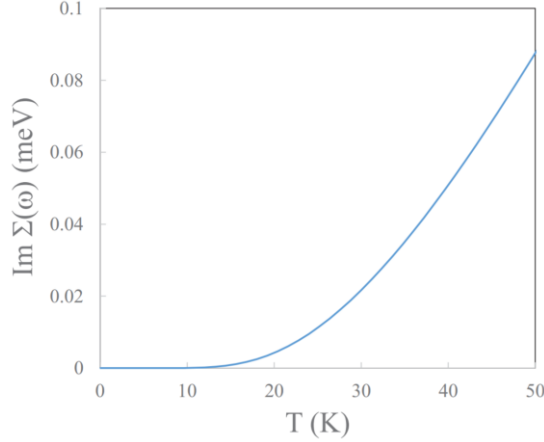


Figure (4.5) – The thermally activated temperature dependence of the imaginary part of the self-energy due to interactions with spin excitons, for electrons on the surface Fermi surface (adopted from reference [37]).

and J is the value of the bulk exchange interaction. We shall use the ratio of the surface-to-bulk values of the Kondo exchange of

$$\frac{J'}{J} \sim \exp\left(-\frac{\Delta_+ + \Delta_-}{\hbar v_F}\right) \sim \exp\left(-\frac{8}{3}\right) \quad (4.6)$$

The real part of the $T = 0$ self-energy has logarithmic singularities at $\omega = \pm\omega_0$ with coefficients proportional to the unperturbed density of states at the Fermi energy (i.e. $\sim 2\mu/\Delta_{\pm}^2$). It is these peaks in the self-energy that are responsible for the resonant structure in the angle integrated density of states and, since the structure is associated with electrons or holes in the close vicinity of μ , the intensity of the structure is expected to decrease as the temperature is raised because of smearing caused by the Fermi function [28]. The inclusion of a finite dispersion for the spin-exciton energies would also result in the $T = 0$ logarithmic singularities being broadened [28]. The logarithmic singularities involving Δ_{\pm} are artifacts due to the continuum model having discontinuities in the density of states at the band edges. The structures associated with the band edges, in a more realistic model [28], should consist of rounded peaks.

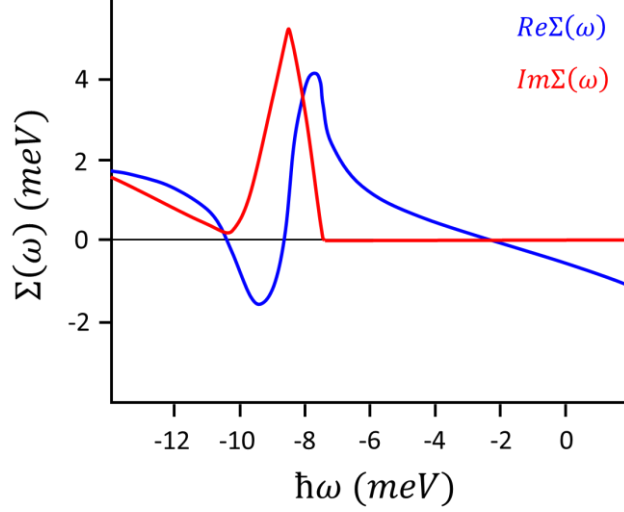


Figure (4.6) –The frequency dependence of the T = 0 self-energy (adopted from reference [37]).

The imaginary part of the T = 0 self-energy is nonzero for energies ω such that $\omega \geq \omega_0$ or $\omega \leq -\omega_0$, and so it does not contribute to scattering of quasiparticles near the Fermi energy. For finite temperatures, the fermionic contribution becomes appreciable outside the edges of these regions due to Fermi-function smearing. However, the bosonic contribution to the self-energy is nonzero at the Fermi energy $\hbar\omega = 0$ and has an intensity proportional to the Bose-Einstein distribution function $N(\hbar\omega_0)$. The bosonic contribution to the self-energy $\Sigma_B(\omega)$ is given by:

$$\text{Re}\Sigma_B(\omega) = N(\hbar\omega_0) \left(\frac{3J'^2}{4Z_0}\right) \left[2 \left(\frac{\Delta_+ - \Delta_-}{\Delta_+ \Delta_-}\right) - \frac{x_-}{\Delta_+^2} \ln \left| \frac{x_+ - \Delta_+}{x_+} \right| - \frac{x_-}{\Delta_+^2} \ln \left| \frac{x_- - \Delta_+}{x_-} \right| - \frac{x_+}{\Delta_-^2} \ln \left| \frac{x_+ + \Delta_-}{x_+} \right| - \frac{x_-}{\Delta_-^2} \ln \left| \frac{x_- + \Delta_-}{x_-} \right| \right] \quad (4.7 \text{ a})$$

$$\text{Im}\Sigma_B(\omega) = N(\hbar\omega_0) \left(\frac{3\pi J'^2}{4Z_0}\right) \left[\frac{x_-}{\Delta_+^2} \{\Theta(\Delta_+ - x_-) - \Theta(-x_-)\} + \frac{x_+}{\Delta_+^2} \{\Theta(\Delta_+ - x_+) - \Theta(-x_+)\} - \frac{x_-}{\Delta_-^2} \{\Theta(\Delta_- + x_-) - \Theta(x_-)\} - \frac{x_+}{\Delta_-^2} \{\Theta(\Delta_- + x_+) - \Theta(x_+)\} \right] \quad (4.7 \text{ b})$$

As can be seen from Figure (4.5), the imaginary part of the bosonic contribution to the self-energy of quasiparticles at the Fermi energy is thermally activated. For the

parameters used in this model, one finds that at 50 K the spin-exciton intensity starts to be appreciable and its width is still a decreasing function of temperature. However, for temperatures of the order of 10 K, where the spin exciton intensity has saturated and its linewidth is resolution limited, the spin-exciton scattering rate is almost completely suppressed. For this temperature, one expects that the dominant contribution to the surface electron scattering comes from interactions with magnetic and nonmagnetic impurities. The frequency dependence of the $T=0$ self-energy is also shown in Figure (4.6).

4.4 Discussion

Here, we have observed an in-gap feature in the photoemission spectra at an energy -9 meV. However, other ARPES experiments [18, 41] observed an in-gap surface feature at around -5 meV. This discrepancy is compatible with the overall experimental resolution combined with the difficulty of accurately determining the Fermi-energy, but the discrepancy might also be due to the measurements being made on different types of surface areas. This is quite probable since through STM measurements, the reconstructed and unreconstructed patches with different terminations may be found on the same surfaces [42]. Similar in-gap resonances have been previously observed in STM measurements [43, 44]. These measurements had a similar temperature dependence to that inferred for feature (c) in our experiments.

One of the STM measurements [43] attributed the resonance to the effect of collective magnetic fluctuations, like the spin-exciton mechanism advocated here. The -9 meV energy of the feature that we observe is also consistent with the -8 meV feature seen in another STM measurements as well [44]. The peak -8 meV, observed in that study, is

damped with increasing temperature much faster than expected from thermal broadening. In fact, the intensity of the feature was completely suppressed above $T \sim 40$ K.

Their experiment also showed a residual spectral density within the gap, in accord with the theory [28]. However, the authors argue that the -8 meV feature is due to the bulk hybridization. We consider this explanation as unlikely, since the bulk 20-meV gap already starts forming in the temperature range of 80 K [36] \sim 100 K [1] \sim 150 K [2]. We consider it more likely that the sharp -8 meV peak observed by the STM measurements and the feature in our experiments have a common origin and represents a spin-exciton resonance in the surface Weyl-cone density of states [28].

Our calculations show the coupling to spin excitons does affect the states of the Weyl cone at energies other than just near the resonance energy. In particular, the resonance produces an exponential temperature dependence of the lifetime, renormalized dispersion relation and reduced quasiparticle weight for the near-Fermi-energy surface states.

The near Fermi-energy spin-exciton-driven scattering is thermally activated but should only appear below the temperature of $T \sim 25$ K at which the bulk spin exciton seen in neutron scattering experiments becomes intense and sharp [29]. The scattering rate is almost completely saturated for temperatures below 10 K. This temperature is considerably lower than the temperature at which the bulk hybridization gap is first observed. Therefore, we argue that the formation of the Fermi liquid that is responsible for the surface conduction should only occur at very low temperatures and may be responsible for the plateau in the resistivity at 5 K.

References Cited in Chapter 4

- [1] H. Miyazaki, T. Hajiri, T. Ito, S. Kunii, and S. I. Kimura, Momentum-Dependent Hybridization Gap and Dispersive In-Gap State of the Kondo Semiconductor SmB_6 , *Phys. Rev. B*, **86**, 075105 (2012).
- [2] X. Zhang, N. P. Butch, P. Syers, S. Ziemak, R. L. Greene, and J. Paglione, Hybridization, Inter-Ion Correlation, and Surface States in the Kondo Insulator SmB_6 , *Phys. Rev. X*, **3**, 011011 (2013).
- [3] K. Flachbart, K. Gloos, E. Konovalova, Y. Paderno, M. Reiffers, P. Samuely, and P. Svec, Energy Gap of Intermediate-Valent SmB_6 Studied by Point-Contact Spectroscopy, *Phys. Rev. B*, **64**, 085104 (2001).
- [4] B. Gorshunov, N. Sluchanko, A. Volkov, M. Dressel, G. Knebel, A. Loidl, and S. Kunii, Low-Energy Electrodynamics of SmB_6 , *Phys. Rev. B*, **59**, 1808 (1999).
- [5] Yazhou Zhou, Qi Wu, Priscila F. S. Rosa, Rong Yu, Jing Guo, Wei Yi, Shan Zhang, Zhe Wang, Honghong Wang, Shu Cai, Ke Yang, Aiguo Li, Zheng Jiang, Shuo Zhang, Xiangjun Wei, Yuying Huang, Yi-feng Yang, Zachary Fisk, Qimiao Si, Liling Sun, and Zhongxian Zhao, Quantum Phase Transition and Destruction of Kondo Effect in Pressurized SmB_6 , *Science Direct*, **62**, 1439 (2017).
- [6] J. C. Nickerson, R. M. White, K. N. Lee, R. Bachman, T. H. Geballe and G. W. Hull Jr., Physical Properties of SmB_6 , *Phys. Rev. B*, **3**, 2030 (1971).
- [7] J. W. Allen, B. Batlogg, and P. Wachter, Large Low-Temperature Hall Effect and Resistivity in Mixed-Valent SmB_6 , *Phys. Rev. B*, **20**, 4807(1979).
- [8] S. Wolgast, C. Kurdak, K. Sun, J. W. Allen, D.-J. Kim, and Z. Fisk, Low-Temperature Surface Conduction in the Kondo Insulator SmB_6 , *Phys. Rev. B*, **88**, 180405 (2013).
- [9] D. J. Kim, S. Thomas, T. Grant, J. Botimer, Z. Fisk, and J. Xia, Surface Hall Effect and Nonlocal Transport in SmB_6 : Evidence for Surface Conduction, *Sci. Rep.*, **3**, 3150 (2013).
- [10] D. J. Kim, J. Xia, and Z. Fisk, Topological Surface State in the Kondo Insulator Samarium Hexaboride, *Nature Material*, **13**, 466 (2014).

-
- [11] P. Syers, D. Kim, M. S. Fuhrer, and J. Paglione, Tuning Bulk and Surface Conduction in the Proposed Topological Kondo Insulator SmB_6 , *Phys. Rev. Lett.*, **114**, 096601 (2015).
- [12] M. Dzero, K. Sun, V. Galitski, and P. Colemann, Topological Kondo Insulators, *Phys. Rev. Lett.*, **104**, 106408 (2010).
- [13] T. Takimoto, SmB_6 : A Promising Candidate for a Topological Insulator, *J. Phys. Soc. Jpn.*, **80**, 123710 (2011).
- [14] N. Xu, P. K. Biswas, J. H. Dil, R. S. Dhaka, G. Landolt, S. Muff, C. E. Matt, X. Shi, N. C. Plumb, M. Radovic, E. Pomjakushina, K. Conder, A. Amato, S. V. Borisenko, R. Yu, H-M. Weng, Z. Fang, X. Dai, J. Mesot, H. Ding, and M. Shi, Direct Observation of the Spin Texture in SmB_6 as Evidence of the Topological Kondo Insulator, *Nat. Commun.*, **5**, 4566 (2014).
- [15] P. Hlawenka, K. Siemensmeyer, E. Weschke, A. Varykahlov, A. Sanchez-Barringa, N. Y. Shitselova, A. V. Dukhnenko, V. B. Filipov, S. Gabani, K. Flachbart, O. Rader, and E. D. L. Rienks, Samarium Hexaboride is a Trivial Surface Conductor, *Nat. Commun.*, **9**, 517 (2018).
- [16] G. Li, Z. Xiang, F. Yu, T. Asaba, B. Lawson, P. Cai, C. Tinsman, A. Berkley, S. Wolgast, Y. S. Eo, D-J. Kim, C. Kurdak, J. W. Allen, K. Sun, X. H. Chen, Y. Y. Wang, Z. Fisk, and L. Li, Two-dimensional Fermi Surfaces in Kondo Insulator SmB_6 , *Science*, **346**, 1208 (2014).
- [17] J. Jiang, S. Li, T. Zhang, Z. Sun, F. Chen, Z. R. Ye, M. Xu, Q. Q. Ge, S. Y. Tan, X. H. Niu, M. Xia, B. P. Xie, Y. F. Li, X. H. Chen, H. H. Wen, and D. L. Feng, Observation of Possible Topological In-Gap Surface States in the Kondo Insulator SmB_6 by Photoemission, *Nat. Commun.*, **4**, 3010 (2013).
- [18] M. Neupane, N. Alidoust, S.-Y. Xu, T. Kondo, Y. Ishida, D. J. Kim, C. Liu, I. Belopolski, Y. J. Jo, T.-R. Chang, H.-T. Jeng, T. Durakiewicz, L. Balicas, H. Lin, A. Bansil, S. Shin, and Z. Fisk, Surface Electronic Structure of the Topological Kondo-Insulator Candidate Correlated Electron System SmB_6 , *Nat. Commun.*, **4**, 2991 (2013).
- [19] N. Xu, X. Shi, P. K. Biswas, C. E. Matt, R. S. Dhaka, Y. Huang, N. C. Plumb, M. Radovic, J. H. Dil, E. Pomjakushina, K. Conder, A. Amato, Z. Salman, D. McK. Paul, J. Mesot, H. Ding, and M. Shi, Surface and Bulk Electronic Structure of the Strongly Correlated System SmB_6 and Implications for a Topological Kondo Insulator, *Phys. Rev. B*, **88**, 121102 (2013).

-
- [20] B. S. Tan, Y.-T. Hsu, B. Zeng, M. C. Hatnean, N. Harrison, Z. Zhu, M. Hartstein, M. Kiourlappou, A. Srivastava, M. D. Johannes, T. P. Murphy, J.-H. Park, L. Balicas, G. G. Lonzarich, G. Balakrishnan, and S. E. Sebastian, Unconventional Fermi Surface in an Insulating State, *Science*, **349**, 287 (2015).
- [21] E. Frantzeskakis, N. de Jong, B. Zwartsenberg, Y. K. Huang, Y. Pan, X. Zhang, J. X. Zhang, F. X. Zhang, L. H. Bao, O. Tegus, A. Varykhalov, A. de Visser, and M. S. Golden, Kondo Hybridization and the Origin of Metallic States at the (001) Surface of SmB₆, *Phys. Rev. X*, **3**, 041024 (2013).
- [22] M. Neupane, N. Alidoust, S.-Y. Xu, T. Kondo, Y. Ishida, D. J. Kim, C. Liu, I. Belopolski, Y. J. Jo, T.-R. Chang, H.-T. Jeng, T. Durakiewicz, L. Balicas, H. Lin, A. Bansil, S. Shin, and Z. Fisk, Surface Electronic Structure of the Topological Kondo-Insulator Candidate Correlated Electron System SmB₆, *Nat. Commun.*, **4**, 2991 (2013).
- [23] V. Alexandrov, M. Dzero, and P. Coleman, Cubic Topological Kondo Insulators, *Phys. Rev. Lett.*, **111**, 226403 (2013).
- [24] F. Lu, J. Z. Zhao, H. Weng, Z. Fang, and X. Dai, Correlated Topological Insulators with Mixed Valence, *Phys. Rev. Lett.*, **110**, 096401 (2013).
- [25] Y. Luo, H. Chen, J. Dai, Z.-A. Xu, and J. D. Thompson, Heavy Surface State in a Possible Topological Kondo Insulator: Magneto Thermoelectric Transport on the (011) Plane of SmB₆, *Phys. Rev. B*, **91**, 075130 (2015).
- [26] V. Alexandrov, P. Coleman, and O. Erten, Kondo Breakdown in Topological Kondo Insulators, *Phys. Rev. Lett.*, **114**, 177202 (2015).
- [27] Y. Luo, H. Chen, J. Dai, Z.-A. Xu, and J. D. Thompson, Heavy Surface State in a Possible Topological Kondo Insulator: Magneto Thermoelectric Transport on the (011) Plane of SmB₆, *Phys. Rev. B*, **91**, 075130 (2015).
- [28] G. A. Kapilevich, P. S. Riseborough, A. X. Gray, M. Gulacsi, Tomasz Durakiewicz, and J. L. Smith, Incomplete Protection of the Surface Weyl Cones of the Kondo Insulator SmB₆: Spin Exciton Scattering, *Phys. Rev. B*, **92**, 085133 (2015).
- [29] P. A. Alekseev, J.-M. Mignot, J. Rossat-Mignod, V. N. Lazukov, I. P. Sadikov, E. S. Konalova, and Y. B. Paderno, Magnetic Excitation Spectrum of Mixed-Valence SmB₆ Studied by Neutron Scattering on a Single Crystal, *J. Phys.: Condens. Matter*, **7**, 289 (1995).

-
- [30] P. A. Alekseev, V. N. Lazukov, K. S. Némovskii, and I. P. Sadikov, Magnetic Excitations in Systems with a Nonmagnetic Ground State and Valence Fluctuations, *J. Exp. Theor. Phys.*, **111**, 285 (2010).
- [31] W. T. Fuhrman, J. Leiner, P. Nikolic, G. E. Granroth, M. B. Stone, M. D. Lumsden, L. De Beer-Schmitt, P. A. Alekseev, J.-M. Mignot, S. M. Koohpayeh, P. Cottingham, W. A. Phelan, L. Schoop, T. M. McQueen, and C. Broholm, Interaction Driven Sub Gap Spin Exciton in the Kondo Insulator SmB_6 , *Phys. Rev. Lett.*, **114**, 036401 (2015).
- [32] P. A. Alekseev, J.-M. Mignot, J. Rossat-Mignod, V. N. Lazukov, I. P. Sadikov, E. S. Konalova, and Y. B. Paderno, Magnetic Excitation Spectrum of Mixed-Valence SmB_6 Studied by Neutron Scattering on a Single Crystal, *J. Phys.: Condens. Matter*, **7**, 289 (1995).
- [33] Michael E. Valentine, Seyed Koohpayeh, W. A. Phelan, Tyrel M. McQueen, Priscila F. S. Rosa, Zachary Fisk, and Natalia Drichko, Breakdown of the Kondo Insulating State in SmB_6 by Introducing Sm Vacancies, *Phys. Rev. B*, **94**, 075102 (2016).
- [34] P. S. Riseborough and S. G. Magalhaes, Spin-Excitons in Heavy-Fermion Semimetals, *J. Magn. Magn. Mater.*, **400**, 3 (2016).
- [35] S. Wolgast, C. Kurdak, K. Sun, J. W. Allen, D.-J. Kim, and Z. Fisk, Low-Temperature Surface Conduction in the Kondo Insulator SmB_6 , *Phys. Rev. B*, **88**, 180405 (2013).
- [36] W.-K. Park, Lunan Sun, Alexander Noddings, Dae-Jeong Kim, Zachary Fisk, and Laura H. Greene, Topological Surface States Interacting with Bulk Excitations in the Kondo Insulator SmB_6 Revealed via Planar Tunneling Spectroscopy, *Proc. Natl. Acad. Sci.*, **113**, 6599 (2016).
- [37] Arian Arab, A. X. Gray, S. Nemsak, D. V. Evtushinsky, C. M. Schneider, D. J. Kim, Z. Fisk, P. F. S. Rosa, T. Durakiewicz and P. S. Riseborough, Effects of Spin Excitons on the Surface States of SmB_6 : A Photoemission Study, *Phys. Rev. B*, **94**, 235125 (2016).
- [38] P. Schlotmann, Impurity Bands in Kondo Insulators, *Phys. Rev. B*, **46**, 998 (1992).
- [39] P. Schlotmann, Influence of a Kondo-Hole Impurity Band on Magnetic Instabilities in Kondo Insulators, *Phys. Rev. B*, **54**, 12324 (1996).
- [40] P.S. Riseborough, Collapse of the Coherence Gap in the Semiconductors, *Phys. Rev. B*, **68**, 235213 (2003).

-
- [41] N. Xu, C. E. Matt, E. Pomjakushina, X. Shi, R. S. Dhaka, N. C. Plumb, M. Radovic, P. K. Biswas, D. Evtushinsky, V. Zabolotnyy, J. H. Dil, K. Conder, J. Mesot, H. Ding, and M. Shi, Exotic Kondo Crossover in a Wide Temperature Region in the Topological Kondo Insulator SmB_6 Revealed by High-Resolution ARPES, *Phys. Rev. B*, **90**, 085148 (2014).
- [42] S. Robler, L. Jaio, D. J. Kim, S. Seiro, K. Rasim, F. Steglich, L. H. Tjeng, Z. Fisk, and S. Wirth, Surface and Electronic Structure of SmB_6 Through Scanning Tunneling Microscopy, *Philos. Mag.*, **96**, 3262 (2016).
- [43] W. Ruan, C. Ye, M. Guo, F. Chen, X. Chen, G. M. Zhang, and Y. Wang, Emergence of a Coherent In-Gap State in the SmB_6 Kondo Insulator Revealed by Scanning Tunneling Spectroscopy, *Phys. Rev. Lett.*, 112, 136401 (2014).
- [44] M. M. Yee, Y. He, A. Soumyanarayanan, D. J. Kim, Z. Fisk, and J. E. Hoffmann, Imaging the Kondo Insulating Gap on SmB_6 , arXiv:1308.1085v2.

CHAPTER 5
ELECTRONIC STRUCTURE OF A GRAPHENE-LIKE ARTIFICIAL CRYSTAL OF
NdNiO₃ (111)

5.1 Introduction

A central theme threading through the modern condensed matter is the search and understanding of novel quantum phases of matter. After decades of intense studies, strong electron correlations, initially neglected in the band theory, have been recognized as the key factor that can drive a system into diverse many-body phases such as heavy-fermion behavior (discussed in Chapter 1), unconventional magnetic and superconducting states, metal-to-insulator transition, quantum criticality, and glass-like spin and charge states to name a few [1].

Subsequently, during the past decade, it was realized that strong spin-orbit coupling (SOC), once added to the band structure of a weakly-correlated material, can dramatically influence the electronic states and lead to qualitatively new phases of matter, including topological insulators, topological superconductors, and topological semimetals [2-5]. Inspired by these results, very recently, it has been proposed that merging electronic correlations and SOC can potentially bring about a plethora of exotic quantum states such as axion insulator, topological Mott insulator, multipolar order, Kitaev spin liquid, and so on [6-10]. Furthermore, search for the materials with singularities in the density of states stemming from internal lattice symmetries and fine-tuned interactions have attracted a particular interest as the possible platform for topologically non-trivial interacting states of

matter, including quantum anomalous Hall effect and topological superconductivity [11-13].

Very recently it has been predicted that artificial complex-oxide heterostructures containing ultrathin buried layers grown along the pseudocubic [111] direction to host a plethora of new quantum states arising from the graphene-like lattice geometry and the interplay between strong electronic correlations and band topology [7, 10, 14-16].

From the experimental standpoint, however, the realization of the correlated topological states runs into a major challenge of finding bulk crystals to closely match the theoretical proposals. With the recent advances in synthesis of ultra-thin layers of chemically-complex materials, this challenging issue could be potentially mitigated. Specifically, the fabrication of a specific number of unit cells of an ultra-thin film derived from perovskite or pyrochlore structure along high-index crystallographic directions naturally gives rise to the buckled graphene-like or frustrated lattice geometry, and results in interactions favoring the correlated topological phases.

To date, however, two key obstacles stand in the path of realization of such a design paradigm: (1) the ongoing difficulties of the growth along polar directions [17-20] and (2) the critical problem of measurement of electronic band structure from only one- or two-unit cells buried under a non-active capping layer. As a result, most conventional surface-sensitive probes such as angle-resolved photoemission spectroscopy (ARPES), which provides direct information on the electronic bands, are severely limited in their applicability for such interesting material systems. Once resolved, the exquisite control over lattice geometry and electronic structure stemming from the successful resolution of

these two challenges will enable the next generation of artificial topological materials with strong electronic correlations.

In this Chapter, we present the results of the study, wherein we used a combination of bulk-sensitive soft x-ray angle-resolved photoelectron spectroscopy (SX-ARPES) [21, 22], hard x-ray photoelectron spectroscopy (HAXPES) [23] and density functional theory (DFT+ U) calculations to investigate the momentum-resolved and angle-integrated valence-band electronic structure of the buried two-dimensional NdNiO₃ layer in a geometrically engineered superlattice grown epitaxially on a LaAlO₃ (111) oriented single-crystal substrate [24].

In this system, the nickelate layer forms a buckled honeycomb lattice that was initially proposed to give rise to a characteristic band structure consisting of four bands around the Fermi level: two linearly crossing at K forming a Dirac point, and two flat bands with a quadratic touching point of the two sets at Γ for ferromagnetic (FM) coupling [25-27]. More recent DFT+ U calculations showed that a bond disproportionation in a form of breathing-mode distortion of the oxygen octahedra lifts the equivalence of the two Ni sublattices and opens a small gap at the Dirac (K, K') points, thus destroying the topological QAH/FM phase and shifting the material towards the Mott part of the phase diagram [28, 29].

Furthermore, x-ray resonant magnetic scattering measurements found indication for antiferromagnetic (AFM) spin correlations instead. Polarization-dependent x-ray absorption spectroscopy (XAS) measurements [24] revealed almost an order of magnitude stronger x-ray linear dichroism (XLD) effect than that observed in (001)-oriented superlattices [30-32].

As suggested by the first-principle calculations, such surprising observation is related to the appearance of an antiferro-orbital ordering of $d_{3z^2-r^2}$ and $d_{3x^2-r^2}$ orbitals, stemming from the lowering of structural symmetry to P1 [24]. This unusual effect originates from the decoupling of the two Ni sublattices due to AFM order where the decoupling of the NiO_6 octahedra is realized by the surrounding AlO_6 octahedra in the double perovskite structure. Theoretically, two different orbital arrangements are possible: one with P1 symmetry in a 1×1 -unit cell and another with P3 symmetry in a larger $\sqrt{3} \times \sqrt{3} R30^\circ$ lateral unit cell [Figure (B.1) in Appendix B]. In this Chapter, we provide unambiguous evidence by the SX-ARPES measurements supporting the P1 symmetry, which is consistent with the reported XLD results.

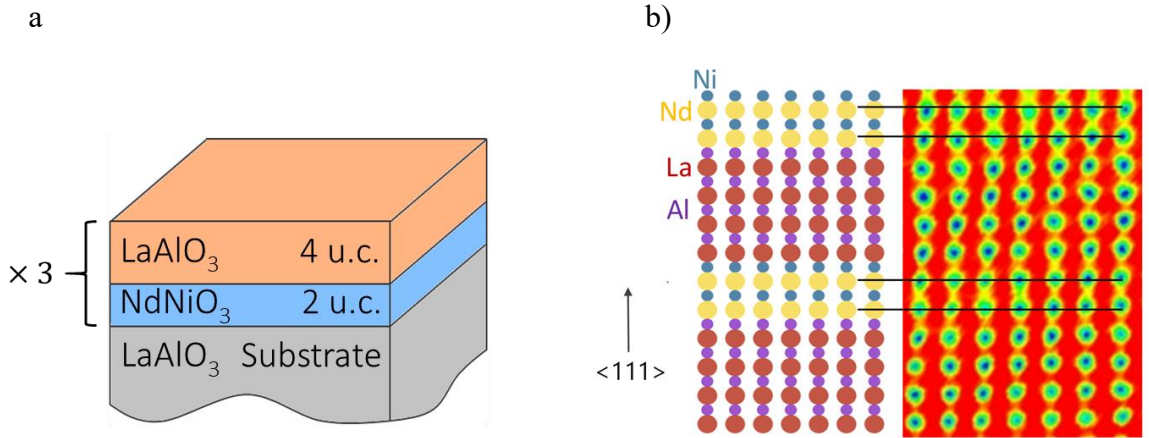


Figure (5.1) – a) Schematic diagram of the $\text{LaAlO}_3/\text{NdNiO}_3$ heterostructure, grown along the $[111]$ direction b) High-resolution STEM cross sectional image of the sample and the corresponding schematics identifying atomic arrangements in the bilayer.

5.2 Experimental Results

For our experiments, high-quality epitaxial superlattice consisting of three repetitions of (111) oriented $[2 \text{ u.c. NdNiO}_3 / 4 \text{ u.c. LaAlO}_3]$ (with LaAlO_3 layer on top) was grown by pulsed laser interval deposition system [24] on a LaAlO_3 (111) substrate, Figure (5.1 a). The growth was carried out at 670°C under 150 mTorr partial pressure of oxygen. The sample was annealed at the growth temperature for 30 minutes under 1 bar pressure of ultra-pure oxygen.

Coherent epitaxy and thicknesses of all layers were monitored during growth using reflection high-energy electron diffraction (RHEED) and confirmed *ex-situ* using scanning transmission electron microscopy (STEM), Figure (5.1 b). The STEM measurements were carried out using a spherical aberration-corrected JEM-ARM200F microscope operated at 200 kV in the high-angle annular dark field (HAADF) imaging mode. The quality (flatness) of the surface was verified using atomic force microscopy (see Figure (C.1 a) in Appendix C), revealing RMS roughness of approximately 200 pm (less than one-unit cell). Crystallinity and correct layering of the superlattice was confirmed using high-resolution

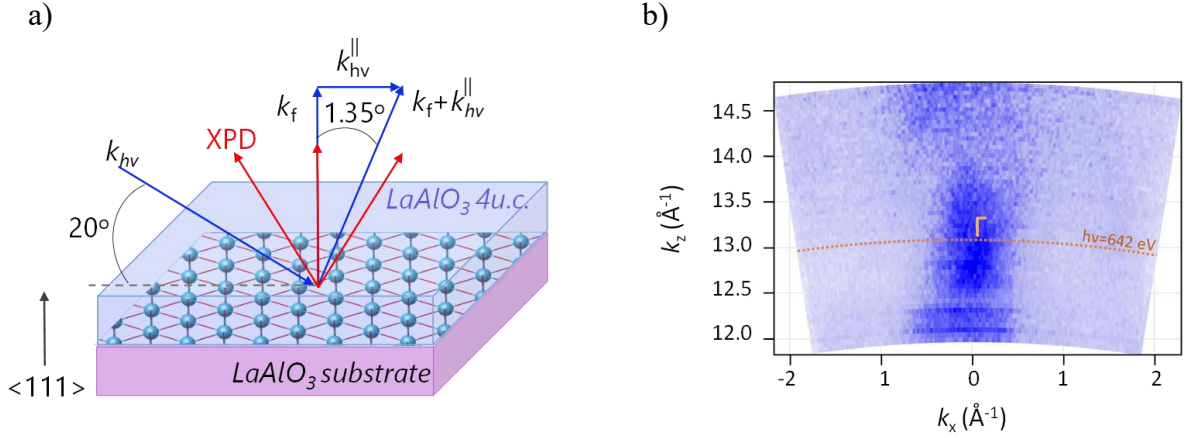


Figure (5.2) – a) Schematic diagram of the experimental geometry with all the relevant momentum vectors shown and labeled b) Momentum-resolved k_x - k_z map obtained by scanning the excitation photon energy. At the photon energy of 642 eV, the final photoelectron wave vector k_f points close to a high-symmetry point along the k_z direction in the extended BZ picture.

synchrotron-based x-ray diffraction spectroscopy (see Figure (C.1 b) in the Appendix C). Additional details regarding synthesis and characterization are provided in [33, 34] with relevant references to prior studies focusing on optimization and characterization of this and similar [111] multilayer structures.

5.2.1 Soft x-ray angle-resolved photoemission E_b - k_x measurements

Soft x-ray angle-resolved photoemission spectroscopy measurements were carried out at the high-resolution ADDRESS beamline of the Swiss Light Source [22]. The SX-ARPES endstation at the ADDRESS beamline is equipped with a SPECS PHOIBOS-150 hemispherical electrostatic analyzer and a six-axis cryogenic manipulator, allowing for facile three-dimensional mapping of the valence-band electronic structure in the momentum space (k_x , k_y and k_z via variable photon energy, see Chapter 3).

At the photon energy of 642 eV, total instrumental energy resolution was estimated to be 111 meV. All the measurements were carried in the near-normal emission (NE) [111] experimental geometry. For the angle-resolved SX-ARPES measurements, the fixed angle

of 70° between the beamline and the analyzer direction thus required the grazing incidence angle to be set at 20° ($= 90^\circ - 70^\circ$), Figure (5.2 a). The sample temperature was set to 100K. At photon energy of 642 eV, the final photoelectron wave vector \mathbf{k}_f will be close to a high-symmetry point along the k_z direction in the extended BZ picture. This is also confirmed experimentally with a variable photon energy (k_z) scan as shown in Figure (5.2 b).

Figure (5.3 a) shows a valence-band dispersion along the $K'-\Gamma-K$ high-symmetry direction recorded at the photon energy of 642 eV. The spectra in Figure (5.3 a) are strongly modulated by the photoemission matrix elements in energy resulting in MEW-DOS, which is represented by a white energy distribution curve (EDC) on the right side of the plot, with the four most prominent features appearing at -1.6, -3.3, -5.1 and -10.0 eV, and labeled A through D, respectively.

The experimental momentum dispersion exhibits excellent agreement with the band structure calculated with DFT+ U for the AFM ordering of the Ni sites with the P1 symmetry, Figure (5.3 b). Density functional theory (DFT+ U) calculations were carried out with the all-electron full potential linearized augmented plane wave method in the WIEN2k code [35, 36]. The valence-band dispersion is dominated by two flat bands just below the Fermi level (one in each spin channel), a dense set of relatively flat bands in the intermediate region between -0.3 and -5 eV, followed by several more dispersive bands at the bottom of the valence band with a minimum at Γ , corresponding to feature D in Figure (5.3 a). The total width of the calculated valence-band manifold is slightly underestimated, as evidenced by the different binding energy scale - a general feature of this calculation scheme, wherein parameters such as the bandgap, d -band bandwidths and positions are

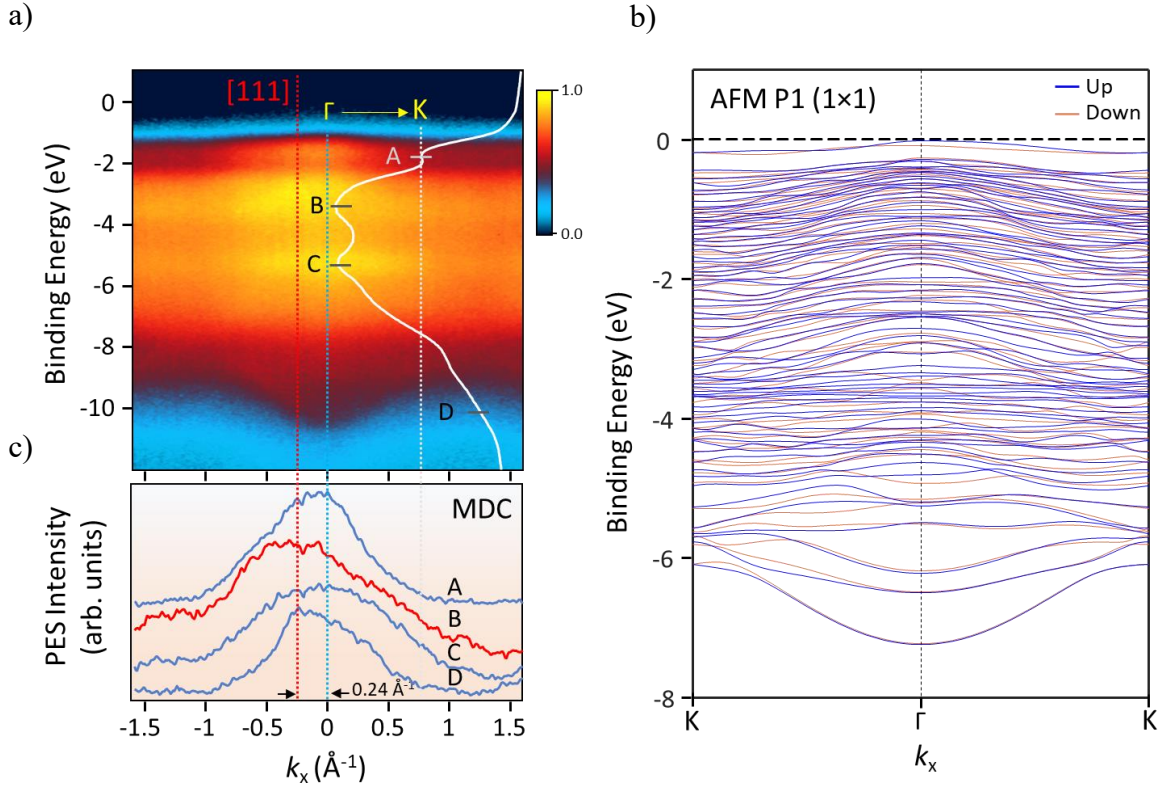


Figure (5.3) – a) SX-APRES spectrum of the valence-band dispersion measured along the $K'-\Gamma-K$ high-symmetry direction. The white EDC curve represents the momentum-integrated MEW-DOS, with most prominent features A-D labeled. b) The DFT+U calculation of the spin-projected band structure for the AFM P1 (1 \times 1) configuration shown for the same cut of the BZ. c) Momentum distribution curves recorded at the binding energies of the features A, B, C and D.

very sensitive to the changes in the Hubbard terms (see *e.g.* a systematic study of these effects in ZnO in [37]).

The momentum distribution curves (MDC) recorded at the binding energies of the four above-mentioned features A-D, Figure (5.3 c), reveal an important effect, which is characteristic of the higher-energy (soft- and hard x-ray) ARPES [38, 39]. Specifically, as the dipole approximation, which is typically used in ARPES, no longer fully holds for the higher photon energies, the non-negligible photon momentum wave vector ($\mathbf{k}_{h\nu}$) shifts the position of the final photoelectron wave vector (\mathbf{k}_f) along the k_x direction in accordance with a simple wave vector conservation equation $\mathbf{k}_f = \mathbf{k}_i + \mathbf{k}_{h\nu}^{\parallel}$, where \mathbf{k}_i is the initial-state wave vector and $\mathbf{k}_{h\nu}^{\parallel} = \mathbf{k}_{h\nu} \cos(20^\circ)$ is the photon momentum wave vector adjusted for the

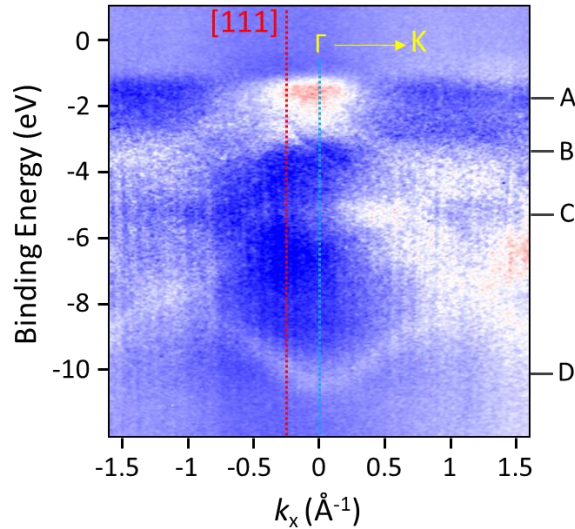


Figure (5.4) – SX-APRES spectrum of the valence-band dispersion measured along the $K'\text{-}\Gamma\text{-}K$ high-symmetry direction at photon energy of 642 eV. Spectrum can be normalized by the binding-energy-averaged and the k -averaged spectra to enhance the dispersive features.

grazing incidence angle of 20° . As a result, electronic dispersion observed in the 2D detector is shifted relative to the normal $[111]$ direction by approximately 0.24 \AA^{-1} , in excellent agreement with the theoretically predicted shift of 0.3 \AA^{-1} (or 1.35° in the detector-angle units).

This shift is immediately apparent to the eye for feature D, due to its strongly-dispersive nature. From Figure (5.3 a), it is evident that this parabolic band is clearly centered around the $\mathbf{k}_{h\nu}$ -shifted Γ point (blue dashed line). In stark contrast with the strongly-dispersive feature D, the intensity of a mostly non-dispersive feature B is centered around the normal $[111]$ direction (red dashed line in Figures (5.3 a, c)). The angular photoelectron intensity distributions for such mostly-flat features are dominated by the XPD effects and not affected by the photon momentum ($\mathbf{k}_{h\nu}$) shift, analogous to localized core-levels with no dispersion in k [40, 41]. As an intermediate case, feature A, which is weakly dispersive, shows a mixture of XPD and electronic band structure characteristics, as evident from its MDC, which is centered in-between the $[111]$ and Γ directions, with its

maximum somewhat closer to the Γ point. For such features, it is critical to emphasize the importance of utilizing data normalization procedures that separate the effects of true electronic-state dispersion from XPD in soft- and hard x-ray ARPES. This will be explained in section 5.2.4. In order to enhance the relative intensities of the dispersive features (*e.g.* A and D) and, at the same time, suppress the non-dispersive features (*e.g.* B and C) of the raw ARPES E_b - k_x map shown in Figure (5.3 a), the ARPES spectra could be normalized by the binding-energy-averaged and the k -averaged spectra. The result of this normalization procedure is shown in Figure (5.4).

5.2.2 Soft x-ray valence-band resonant photoemission measurement

To identify the elemental and orbital origins of the key features in the valence-band spectra we utilize resonant photoemission spectroscopy at the Ni L_2 absorption threshold, in conjunction with first-principles GGA+ U DOS calculations. The generalized gradient approximation [42] was used for the exchange-correlation functional together with an on-site Hubbard U term [43] with $U = 5.0$ eV and $J = 1.7$ eV for Ni $3d$ and $U = 8$ eV for Nd. The 1×1 unit cell with P1 symmetry was modelled with a 30-atom supercell with the lateral lattice constant of LaAlO_3 , while the $\sqrt{3} \times \sqrt{3} R30^\circ$ reconstruction required a three-times-larger unit cell. Octahedral tilts and distortions were fully considered. The Fermi surface calculations for different isoenergetic levels were carried out with a very dense $30 \times 30 \times 10$ k -point grid and plotted using the XCRYSDEN package [44].

Figure (5.5 a) shows the VB photoemission spectra recorded at the photon energies of 868.5 eV and 873.4 eV, corresponding to the 'off' and 'on' resonant conditions for the Ni L_2 absorption edge, respectively. The corresponding XAS spectrum, measured *in-situ* using

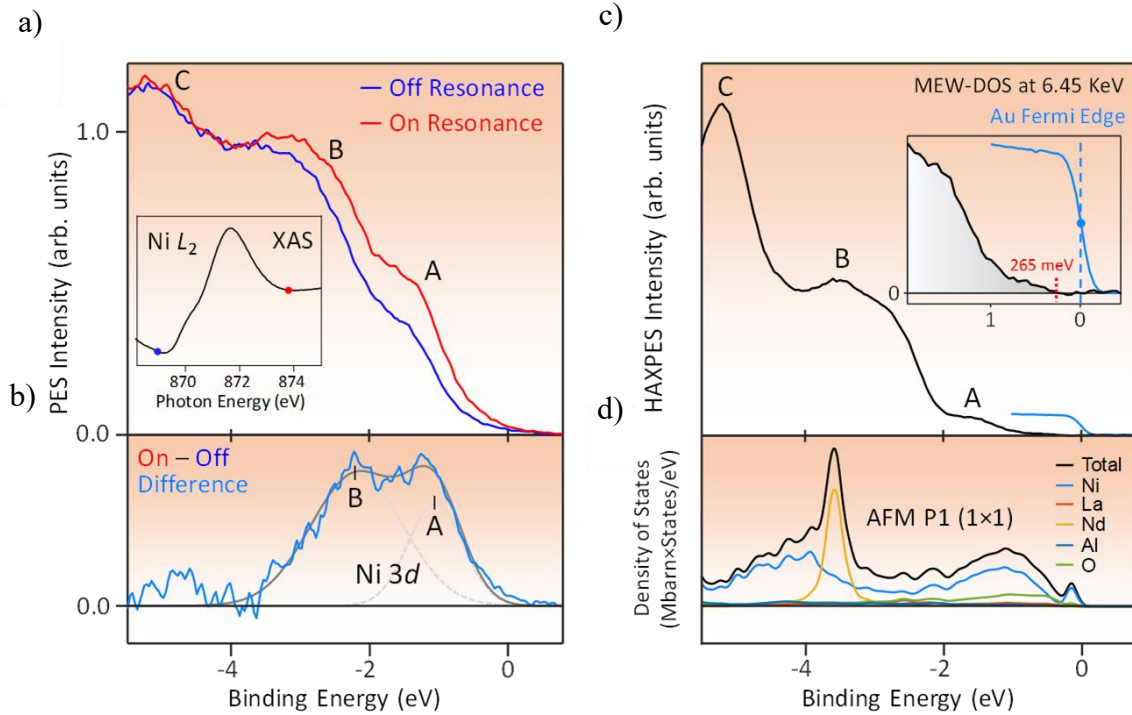


Figure (5.5) – a) Angle-integrated VB spectra recorded at the photon energies of 868.5 eV (off resonance) and 873.4 eV (on resonance) reveal the contribution of the Ni 3*d* states via resonant enhancement. Inset shows the Ni *L*₂ XAS spectrum with the blue and red markers at the relevant photon energies. b) The difference spectrum obtained by subtracting the ‘off’ spectrum shown in panel (a) from the ‘on’ spectrum. Two distinct components A and B, corresponding to the NdNiO₃-derived Ni 3*d* states, are fitted using two Gaussian peaks centered at -1.1 and -2.2 eV. c) Bulk-sensitive HAXPES spectrum recorded at the photon energy of 6.45 keV with the IMFP of approximately 85 Å. Inset shows a high-statistics spectrum of the valence-band maximum (at -265 meV), referenced to the Au Fermi edge. d) Cross-section weighted element-projected and total DOS of the superlattice, calculated in the GGA+*U* framework of DFT, and broadened by convolution with Gaussian and Lorentzian functions to account for both experimental and hole-lifetime broadening.

the total electron yield detection mode, is shown in the inset. We note that the Ni *L*₂ resonance had to be used instead of *L*₃, due to the strong overlap of the latter with the La *M*₄ absorption edge [45].

Resonant photoemission at the transition-metal *L*_{2,3} edges takes advantage of the interference between the direct photoemission channel $2p^63d^n \rightarrow 2p^63d^{n-1} + e^-$ and the decay of a resonantly-excited state $2p^53d^{n+1} \rightarrow 2p^63d^{n-1} + e^-$, which leads to the enhancement of the 3*d* photoemission cross section [45]. As a result, in our case the

contribution from the Ni $3d$ states in the valence bands is significantly amplified, as evident from the "on resonance – off resonance" difference spectrum shown in Figure (5.5 b).

The above-mentioned difference spectrum exhibits two distinct resonant features labeled A and B near the Fermi level (at -1.1 and -2.2 eV), corresponding to the strongly-hybridized Ni $3d$ e_g and t_{2g} states, as well as some additional resonant enhancement of photoemission intensity between -4 and -5 eV, fully-consistent with the first-principles GGA+ U calculations shown in Figure (5.5 d) and discussed below.

It is important to point out that, although the 4 u.c.-thick LaAlO₃ layer resides on top of the NdNiO₃ layer, in the soft x-ray regime we expect to see a dominant contribution from the NdNiO₃-derived strongly-hybridized Ni $3d$ states near the Fermi level. This is in part because, based on the values of the energy-dependent atomic subshell photoionization cross sections [46], the valence bands of the [2 u.c. NdNiO₃ / 4 u.c. LaAlO₃] system are dominated (by orders of magnitude) by the Nd $4f$ and Ni $3d$ states. Specifically, at a photon energy of 642 eV, the photoemission intensities from various constituent states in the MEW-DOS are scaled in accordance with the following differential cross section ratios, normalized to the highest cross section: Nd $4f$: Ni $3d$: O $2p$: Al $3s$: La $5d$ = 1.00 : 0.91 : 0.05 : 0.05 : 0.04, respectively. Other orbitals, such as La $6s$ and Al $3p$ are expected to contribute less than 1% to the detected intensities.

In comparison to such significant cross section-related enhancement, the inelastic and elastic scattering of the photoelectrons originating from NdNiO₃ by the LaAlO₃ overlayer is expected to attenuate the Ni $3d$ and Nd $4f$ VB intensities only by a factor of ~2 at this photon energy, which is significantly less than the disparity in the values of the cross

sections (20× to 100×). In short, the combination of the significantly increased IMFPs in the soft x-ray regime and the dominant character of the Nd $4f$ and Ni $3d$ photoionization cross sections are the key factors enabling the measurement of valence states from the buried NdNiO₃ layer.

5.2.3 Hard x-ray valence-band photoemission measurement

In order to probe the entire depth of the sample, we carried out complementary angle-integrated HAXPES measurements of the valence bands at a photon energy of 6.45 keV, at which the IMFP is estimated to be approximately 85 Å [47], thus allowing to directly probe the MEW-DOS of the entire superlattice and facilitating a straightforward comparison of the experimental data to theory.

The kinetic energy of the Fermi level was determined with a high-statistics measurement on a clean sputtered thin-film Au sample, thus allowing for an accurate calibration of the binding energies for both HAXPES and SX-ARPES measurements. The experimental HAXPES VB spectrum, shown in Figure (5.5 c) exhibits excellent agreement with the total DOS obtained using first-principles GGA+ U calculations (black spectrum in Figure (5.5 d)) both in terms of the relative intensities and relative positions of the key features. Furthermore, the experimental valence-band maximum appears at the binding energy of -265 meV ($E_{\text{VB-max}}$) below the Fermi level, as referenced by the Au Fermi edge measurement (inset). The magnitude of this value corresponds to the size of the valence-band bandgap ($E_{\text{VB-max}} - E_{\text{F}}$), suggesting that the full bandgap of NdNiO₃ (111) is at least this large. Indeed, the DFT+ U calculations render a gap of approximately 1 eV.

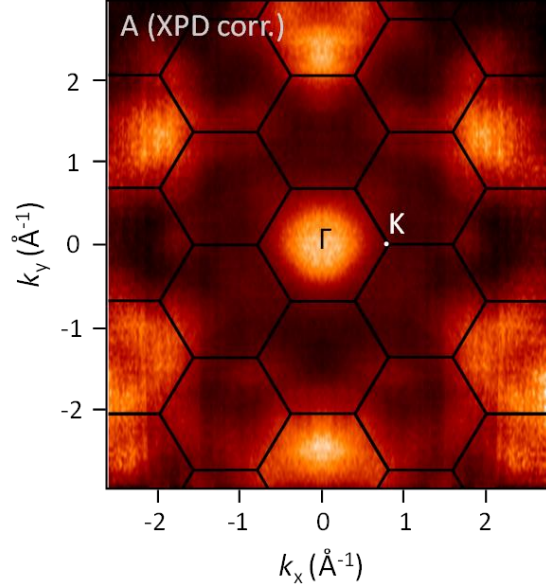


Figure (5.6) – Momentum-resolved XPD-corrected SX-ARPES photoemission intensity map of the Ni 3d states near the valence-band maximum (feature A, centered at -1.6 eV below E_F).

Finally, the photoionization cross-section-weighted [48] element-projected DOS spectra in Fig. 2d (color spectra) reveal the dominant character of the NdNiO₃-derived states within the valence band. In particular, while the Nd 4*f* states contribute to a strong localized peak at -4 eV, the Ni 3*d* states hybridized with oxygen dominate the whole width of the valence bands with *e_g* character just below the Fermi level and extending up to the bottom of the VB (not shown here), and Ni *t_{2g}* states in between, in agreement with the soft x-ray resonant photoemission results in Figure (5.5 a, b).

5.2.4 Soft x-ray angle-resolved Fermi-surface mapping

Figure (5.6) shows the XPD-corrected isoenergetic SX-ARPES intensity map in (k_x , k_y) integrated over a 200 meV binding-energy window, which is comparable with our total experimental energy resolution of 111 eV and centered at the binding energy of the VB feature A (Ni 3*d* peak at -1.6 eV). The map was obtained by recording the E_b - k_x dispersions while rotating the sample about the polar ‘tilt’ axis, which is orthogonal to k_x and thus

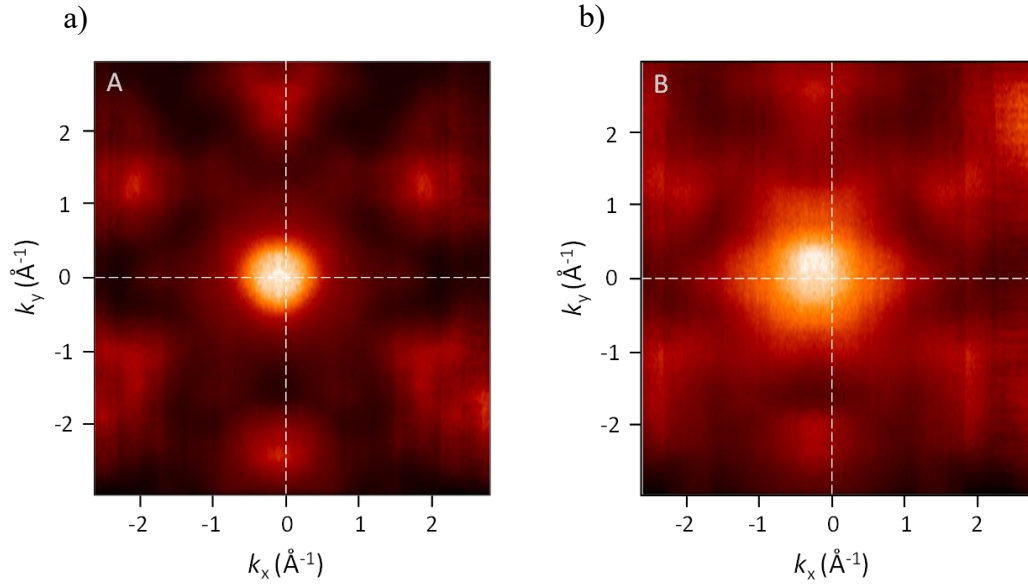


Figure (5.7) – a) Non-normalized momentum-resolved photoemission intensity map of the VB feature A, containing combined contributions from the Ni $3d$ dispersive states and the XPD intensity modulations. The central intensity peak appears shifted toward the [111] emission direction due to a significant XPD contribution to the spectrum. b) Non-normalized photoemission intensity map of the VB feature B comprised of flat XPD-like bands. The central intensity peak appears exactly along the [111] emission direction, confirming an overwhelming fraction of the XPD-derived intensity in the spectrum.

corresponds to the k_y direction in the momentum space, as explained for a typical ARPES experiment in Chapter 1. To access a wider range of k_x values, angle-resolved measurements were repeated at the photoelectron take-off angles of $\pm 4^\circ$ from the normal [111] direction. The data was combined with the NE measurement to form a larger, more complete dataset. Faint vertical lines at $k_x = \pm 2 \text{\AA}^{-1}$ in Figure (5.6) mark the places where the datasets overlapped.

The XPD correction, resulting in the separation of the electronic band dispersion from the residual XPD intensity modulations, was carried out according to the procedure described in the following and is consistent with that used in the prior studies [40,41]. The non-normalized momentum-resolved photoemission intensity map of the VB feature A, containing combined contributions from the Ni $3d$ dispersive states and the XPD intensity modulations is shown in Figure (5.7 a). The central intensity peak appears shifted toward

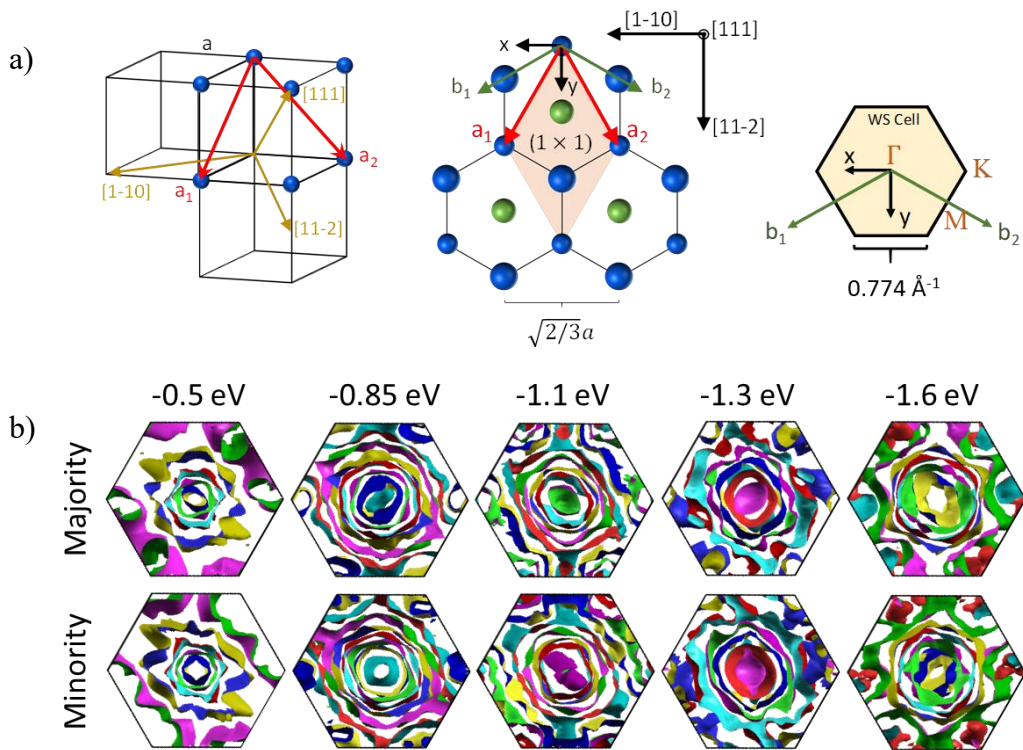


Figure (5.8) – a) Perovskite structure along conventional $[001]$ direction on the left and along $[111]$ direction in the middle are shown; right panel shows the hexagonal Brillouin Zone of the $[111]$ structure. b) Isoenergetic cuts through the band structure in reciprocal space for the majority (top row) and minority (bottom row) bands, calculated for the binding-energy range from -0.5 eV to -1.6 eV, and spanning the major Ni $3d$ features near the VB maximum.

the $[111]$ emission direction due to a significant XPD contribution to the spectrum. The non-normalized photoemission intensity map of the VB feature B comprised of flat XPD-like bands is shown in Figure (5.7 b). The central intensity peak appears exactly along the $[111]$ emission direction, confirming an overwhelming fraction of the XPD-derived intensity in the spectrum as shown in Figure (5.7 b).

Features in the electronic band dispersion observed at this relatively low binding energy to a large extent determine some of the key functional properties of such materials and can be meaningfully compared to the theoretical band structure, which becomes increasingly complicated at higher binding energies (as evident from Figure (5.8 b)).

The calculated schematic map of the extended BZ picture zone boundaries, with the central BZ at $(0 \text{ \AA}^{-1}, 0 \text{ \AA}^{-1})$, is overlaid on the experimental data, matching perfectly the

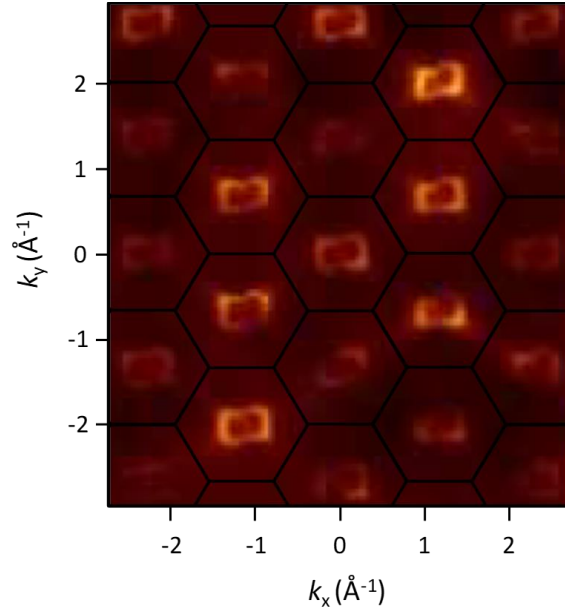


Figure (5.9) – One step theory calculation of the momentum-resolved SX-ARPES spectra showing Ni $3d$ states near the Fermi level. Calculations were carried out using experimental SX-ARPES geometry for the photon energy of 642 eV. Clear modulations of the intensities between adjacent BZs due to the strong matrix-element effects are observed, consistent with the experimental observations.

hexagonal symmetry of the observed photoemission intensity distribution, consistent with the buckled honeycomb NdNiO_3 (111) structure, Figure (5.8 a). Minor apparent distortions in the image are observed near the edges of the map since the final photoelectron wave vector spans a spherical (and not planar) trajectory in the three-dimensional extended BZ picture as explained in Chapter 3 [39]. Additionally, the neighboring BZs alternate in the overall photoemission intensities due to the matrix-element effects, which are ubiquitous in angle-resolved photoemission experiments as explained in Chapter 1 [49, 50]. This inherent experimental artefact, leading to suppression of the photoemission intensities for every other Brillouin zone along the Γ -M high symmetry directions, has been recently observed in similar [111] compounds [51, 52], as well as other solids with hexagonal crystalline structure [53, 54].

The observed periodicity and the BZ size correspond to the simulated AFM P1 symmetry, as shown schematically in Figure (5.8 b), giving further evidence for the latter.

In Figure (5.8 b), we show isoenergetic cuts through the band structure in reciprocal space for the majority and minority bands, calculated for the energy range spanning the near- E_F Ni 3*d* states (from -0.5 eV to -1.6 eV). Additional calculations for a wider energy range, from -0.075 eV to -3.58 eV, are shown in the Figure (D.1) in Appendix D. The isoenergetic cuts are dominated by the hexagonal/circular features around Γ and additional features centered at the zone boundary at K. Although some of the fine details of the (k_x, k_y) band dispersion observed in theory are averaged out in the experiment because of our total energy resolution (~ 111 meV), as well as the choice of our binding-energy integration window (200 meV), we observe a good agreement between the two. This is not surprising, considering the excellent agreement between the experiment and theory for both the momentum-resolved band structure and the total MEW-DOS.

As an additional theoretical benchmarking test, we compared our results to the one-step photoemission calculations based on a fully relativistic LDA+*U* layer-KKR approach and a time-reversed LEED final state [55], Figure (5.9). The SX-ARPES calculations were carried out within the framework of the fully-relativistic one-step model of photoemission [56], as implemented in the multiple scattering Green function SPR-KKR package [55]. This method accounts for all relevant experimental aspects of the photoemission process, including experimental geometry, photon energies, x-ray polarization, matrix element effects, multiple scattering in the initial and final states, and all surface- and interface-related effects in the excitation process. Results from these additional calculations represent true angular distributions of photoemission intensities in the extended BZ picture, as applied to the actual multilayer structure with the explicitly included surface. Good similarities between the experiment and the simulation are observed: the sizes and the

periodicity of the BZs that are consistent with the 1×1 P1 structure modeled for our specific experimental geometry, along with the above-mentioned depressions in the intensities of adjacent BZs due to the matrix-element effects. Such calculations represent a key first step in the interpretation of the bulk-sensitive momentum-resolved photoemission data for [111] oriented multilayers.

5.3 Conclusion

In summary, we utilized a combination of bulk-sensitive soft- and hard x-ray photoemission techniques to map out momentum-resolved electronic band dispersion of a buried two-dimensional NdNiO_3 (111) layer in a geometrically-engineered $[2 \text{ u.c. NdNiO}_3 / 4 \text{ u.c. LaAlO}_3] \times 3$ superlattice, and to directly measure its MEW-DOS. Our results, in conjunction with the first-principles DFT+ U calculations, provide a direct evidence of the formation of a new AFM orbital arrangement with the P1 symmetry in a 1×1 -unit cell in graphene-like NdNiO_3 . These results demonstrate a crucially important way of investigating electronic structure of novel quantum materials and pave the way for the discovery of new topological states in [111]-grown perovskite and pyrochlore heterostructures and buried interfaces.

References Cited in Chapter 5

- [1] M. Imada, A. Fujimori, and Y. Tokura, Metal Insulator Transitions, *Rev. Mod. Phys.*, **70**, 1039 (1998).
- [2] M. Z. Hasan and C. L. Kane, Colloquium: Topological Insulators, *Rev. Mod. Phys.*, **82**, 3045 (2010).
- [3] X.-L. Qi and S.-C. Zhang, Topological Insulators and Superconductors, *Rev. Mod. Phys.*, **83**, 1057 (2011).
- [4] M. Sato and Y. Ando, Topological Superconductors, *Rep. Prog. Phys.*, **80**, 076501 (2017).
- [5] B. Yan and C. Felser, Topological Materials: Weyl Semimetals, *Annu. Rev. Condens. Matter Phys.*, **8**, 337 (2017).
- [6] W. Witczak-Krempa, G. Chen, Y. B. Kim, and L. Balents, Correlated Quantum Phenomena in the Strong Spin-Orbit Regime, *Annu. Rev. Condens. Matter Phys.* **5**, 57 (2014).
- [7] G. A. Fiete and A. Rüegg, Topological Phases in Oxide Heterostructures with Light and Heavy Transition Metal Ions, *J. Appl. Phys.* **117**, 172602 (2015).
- [8] J. G. Rau, E. Kin-Ho Lee, and H.-Y. Kee, Spin-Orbit Physics Giving Rise to Novel Phases in Correlated Systems: Iridates and Related Materials, *Annu. Rev. Condens. Matter Phys.* **7**, 195 (2016).
- [9] R. Schaffer, E. Kin-Ho Lee, B.-J. Yang, and Y. B. Kim, Recent Progress on Correlated Electron Systems with Strong Spin–Orbit Coupling, *Rep. Prog. Phys.* **79**, 094504 (2016).
- [10] S. Okamoto and D. Xiao, Transition-Metal Oxide (111) Bilayers, *J. Phys. Soc. Jpn.* **87**, 041006 (2018).
- [11] T. Löthman and A. M. Black-Schaffer, Universal Phase Diagrams with Superconducting Domes for Electronic Flat Bands, *Phys. Rev. B* **96**, 064505 (2017).
- [12] A. Ramachandran, A. Andreanov, and S. Flach, Chiral Flat Bands: Existence, Engineering, and Stability, *Phys. Rev. B* **96**, 161104(R) (2017).
- [13] K.-E. Huhtinen, M. Tylutki, P. Kumar, T. I. Vanhala, S. Peotta, and P. Törmä, Spin-Imbalanced Pairing and Fermi Surface Deformation in Flat Bands, *Phys. Rev. B* **97**, 214503 (2018).

-
- [14] S. Okamoto, Doped Mott Insulators in (111) Bilayers of Perovskite Transition-Metal Oxides with a Strong Spin-Orbit Coupling, *Phys. Rev. Lett.* **110**, 066403 (2013).
- [15] D. Xiao, W. Zhu, Y. Ran, N. Nagaosa, and S. Okamoto, Interface Engineering of Quantum Hall Effects in Digital Transition Metal Oxide Heterostructures, *Nat. Commun.* **2**, 596 (2011).
- [16] L. Si, O. Janson, G. Li, Z. Zhong, Z. Liao, G. Koster, and K. Held, Quantum Anomalous Hall State in Ferromagnetic SrRuO₃ (111) Bilayers, *Phys. Rev. Lett.* **119**, 026402 (2017).
- [17] J. L. Blok, X. Wan, G. Koster, D. H. A. Blank, and G. Rijnders, Epitaxial oxide growth on polar (111) surfaces, *Appl. Phys. Lett.* **99**, 151917 (2011).
- [18] I. Hallsteinsen, J. E. Boschker, M. Nord, S. Lee, M. Rzchowski, P. E. Vullum, J. K. Grepstad, R. Holmestad, C. B. Eom, and T. Tybell, Surface Stability of Epitaxial La_{0.7}Sr_{0.3}MnO₃ Thin Films on (111)-oriented SrTiO₃, *J. Appl. Phys.* **113**, 183512 (2013).
- [19] H. F. Yang, Z. T. Liu, C. C. Fan, Q. Yao, P. Xiang, K. L. Zhang, M. Y. Li, J. S. Liu, and D. W. Shen, Avoiding Polar Catastrophe in the Growth of Polarly Orientated Nickel Perovskite Thin Films by Reactive Oxide Molecular Beam Epitaxy, *AIP Adv.* **6**, 085115 (2016).
- [20] X. Liu, S. Middey, Y. Cao, M. Kareev, and J. Chakhalian, Geometrical Lattice Engineering of Complex Oxide Heterostructures: A Designer Approach to Emergent Quantum States, *MRS Commun.* **6**, 133-144 (2016).
- [21] L. Plucinski, J. Minár, B. S. Sell, J. Braun, H. Ebert, C. M. Schneider, and C. S. Fadley, Band Mapping in Higher-Energy x-ray Photoemission: Phonon Effects and Comparison to One-Step Theory, *Phys. Rev. B* **78**, 035108 (2008).
- [22] V. N. Strocov, M. Kobayashi, X. Wang, L. L. Lev, J. Krempasky, V. V. Rogalev, T. Schmitt, C. Cancellieri, and M. L. Reinle-Schmitt, Soft-X-ray ARPES at the Swiss Light Source: From 3D Materials to Buried Interfaces and Impurities, *Synchr. Rad. News* **27**, 31 (2014).
- [23] C. S. Fadley, x-ray Photoelectron Spectroscopy and Diffraction in Hard x-ray Regime: Fundamental Considerations and Future Possibilities, *Nucl. Instrum. Meth. A* **547**, 24-41 (2005).
- [24] S. Middey, D. Meyers, D. Doennig, M. Kareev, X. Liu, Y. Cao, Z. Yang, J. Shi, L. Gu, P. J. Ryan, R. Pentcheva, J. W. Freeland, and J. Chakhalian, Mott Electrons in an Artificial Graphenelike Crystal of Rare-Earth Nickelate, *Phys. Rev. Lett.* **116**, 056801 (2016).

-
- [25] K.-Y. Yang, W. Zhu, D. Xiao, S. Okamoto, Z. Wang, and Y. Ran, Possible Interaction-Driven Topological Phases in (111) Bilayers of LaNiO_3 , *Phys. Rev. B* **84**, 201104R (2011).
- [26] A. Rüegg and G. A. Fiete, Topological Insulators from Complex Orbital Order in Transition-Metal Oxides Heterostructures, *Phys. Rev. B* **84**, 201103R (2011).
- [27] A. Rüegg, C. Mitra, A. A. Demkov, and G. A. Fiete, Electronic Structure of $(\text{LaNiO}_3)_2/(\text{LaAlO}_3)_N$ Heterostructures Grown Along [111], *Phys. Rev. B* **85**, 245131 (2012).
- [28] A. Rüegg, C. Mitra, A. A. Demkov, and G. A. Fiete, Lattice Distortion Effects on Topological Phases in $(\text{LaNiO}_3)_2/(\text{LaAlO}_3)_N$ Heterostructures Grown Along the [111] Direction, *Phys. Rev. B*, **88**, 115146 (2013).
- [29] D. Doennig, W. E. Pickett, and R. Pentcheva, Confinement-Driven Transitions Between Topological and Mott Phases in $(\text{LaNiO}_3)_N/(\text{LaAlO}_3)_M$ (111) Superlattices, *Phys. Rev. B*, **89**, 121110R (2014).
- [30] A. Blanca-Romero and R. Pentcheva, Confinement-Induced Metal-to-Insulator Transition in Strained $\text{LaNiO}_3/\text{LaAlO}_3$ Superlattices, *Phys. Rev. B*, **84**, 195450 (2011).
- [31] M. J. Han, X. Wang, C. A. Marianetti, and A. J. Millis, A. J. Dynamical Mean-Field Theory of Nickelate Superlattices, *Phys. Rev. Lett.*, **107**, 206804 (2011); *ibid.* **110**, 179904(E) (2013).
- [32] A. Frano, E. Schierle, M. W. Haverkort, Y. Lu, M. Wu, S. Blanco-Canosa, U. Nwankwo, A. V. Boris, P. Wochner, G. Cristiani, H. U. Habermeier, G. logvenov, V. Hinkov, E. Benckiser, E. Weschke, and B. Keimer, Orbital Control of Noncollinear Magnetic Order in Nickel Oxide Heterostructures, *Phys. Rev. Lett.*, **111**, 106804 (2013).
- [33] S. Middey, P. Rivero, D. Meyers, M. Kareev, X. Liu, Y. Cao, J. W. Freeland, S. Barraza-Lopez and J. Chakhalian, Polarity Compensation in Ultra-Thin Films of Complex Oxides: The Case of a Perovskite Nickelate, *Sci. Rep.* **4**, 6819 (2014).
- [34] S. Middey, D. Meyers, M. Kareev, E. J. Moon, B. A. Gray, X. Liu, J. W. Freeland, and J. Chakhalian, Epitaxial Growth of (111)-Oriented $\text{LaAlO}_3/\text{LaNiO}_3$ Ultra-Thin Superlattices, *Appl. Phys. Lett.* **101**, 261602 (2012).
- [35] K. Schwarz and P. Blaha, P. Solid State Calculations Using WIEN2k, *Computer. Matter. Sci.*, **28**, 259 (2003).
- [36] P. Blaha, K. Schwarz, G.K.H. Madsen, D. Kvasnicka, and J. Luitz, Wien2k, An Augmented Plane Wave Plus Local Orbitals Program for Calculating Crystal Properties, ISBN 3-9501031-1-2 (Vienna University of Technology, Vienna, Austria, 2001).

-
- [37] E. S. Goh, J. W. Mah, and T. L. Yoon, Effects of Hubbard Term Correction on the Structural Parameters and Electronic Properties of Wurtzite ZnO, *Comp. Mater. Sci.*, **138**, 111-116 (2017).
- [38] R. C. White, C. S. Fadley, M. Sagurton, and Z. Hussain, Angle-Resolved x-ray Photoemission From the Valence Bands of Tungsten with High Angular Resolution and Temperature Variation, *Phys. Rev. B* **34**, 5226-5238 (1986).
- [39] A. X. Gray, C. Papp, S. Ueda, B. Balke, Y. Yamashita, L. Plucinski, J. Minár, J. Braun, E. R. Ylvisaker, C. M. Schneider, W. E. Pickett, H. Ebert, K. Kobayashi, and C. S. Fadley, Probing Bulk Electronic Structure with Hard X-ray Angle-Resolved Photoemission, *Nat. Mater.* **10**, 759 (2011).
- [40] A. X. Gray, J. Minár, L. Plucinski, M. Huijben, A. Bostwick, E. Rotenberg, S.-H. Yang, J. Braun, A. Winkelmann, and G. Conti, Momentum-Resolved Electronic Structure at a Buried Interface from Soft X-ray Standing-Wave Angle-Resolved Photoemission, *Europhys. Lett.* **104**, 17004 (2013).
- [41] J. Osterwalder, E. A. Stewart, D. Cyr, C. S. Fadley, J. Mustre de Leon, and J. J. Rehr, X-ray Photoelectron Diffraction at High Angular Resolution, *Phys. Rev. B* **35**, 9859(R) (1987).
- [42] J. P. Perdew, K. Burke, and M. Ernzerhof, Generalized Gradient Approximation Made Simple, *Phys. Rev. Lett.*, **77**, 3865 (1996).
- [43] V. I. Anisimov, J. Zaanen, and O. K. Andersen, Band Theory and Mott Insulators: Hubbard U Instead of Stoner, *I. Phys. Rev. B*, **44**, 943 (1991).
- [44] A. Kokalj, Computer Graphics and Graphical User Interfaces as Tools in Simulations of Matter at the Atomic Scale, *Computer. Matter. Sci.*, **28**, 155-168 (2003).
- [45] O. Tjernberg, S. Söderholm, U. O. Karlsson, G. Chiaia, M. Qvarford, H. Nylén, and I. Lindau, Resonant Photoelectron Spectroscopy on NiO, *Phys. Rev. B*, **53**, 10372 (1996).
- [46] J. J. Yeh & I. Lindau, Atomic Data and Nuclear Data Tables 32, 1-155 (1985).
- [47] A. Jablonski and C.J. Powell, Practical Expressions for the Mean Escape Depth, the Information Depth, and the Effective Attenuation Length in Auger-Electron Spectroscopy and x-ray Photoelectron Spectroscopy *J. Vac. Sci. Technol. A* **27**, 253 (2009).
- [48] J. H. Scofield, Theoretical Photoionization Cross Sections from 1 to 1500 keV, *Tech. Rep.*, LLNL Report No. UCRL-51326 (1973).
- [49] M. Mulazzi, M. Hochstrasser, M. Corso, I. Vobornik, J. Fujii, J. Osterwalder, J. Henk, and G. Rossi, Matrix Element Effects in Angle-Resolved Valence Band

Photoemission with Polarized Light from the Ni(111) Surface, *Phys. Rev. B* **74**, 035118 (2006).

[50] J. N. Crain, K. N. Altmann, C. Bromberger, and F. J. Himpsel, Fermi Surfaces of Surface States on Si(111)-Ag, Au, *Phys. Rev. B.* **66**, 205302 (2002).

[51] C. Bareille, F. Fortuna, T. C. Rodel, F. Bertran, M. Gabay, O. Hijano Cubelos, A. Taleb-Ibrahimi, P. Le Fèvre, M. Bibes, A. Barthelemy, T. Maroutian, P. Lecoeur, M. J. Rozenberg, and A. F. Santander-Syro, Two-dimensional Electron Gas with Six-fold Symmetry at the (111) Surface of KTaO₃, *Sci. Rep.*, **4**, 3586 (2014).

[52] F. Y. Bruno, M. Gibert, S. McKeown Walker, O. E. Peil, A. de la Torre, S. Ricco, Z. Wang, S. Catalano, A. Tamai, F. Bisti, V. N. Strocov, J.-M. Triscone, and F. Baumberger, Electronic Structure of Buried LaNiO₃ Layers in (111)-oriented LaNiO₃/LaMnO₃ Superlattices Probed by Soft X-ray ARPES, *APL Materials*, **5**, 016101 (2017).

[53] Y. Sassa, M. Månsson, M. Kobayashi, O. Götberg, V. N. Strocov, T. Schmitt, N. D. Zhigadlo, O. Tjernberg, and B. Batlogg, Probing Two- and Three-dimensional Electrons in MgB₂ with Soft X-ray Angle-resolved Photoemission, *Phys. Rev. B*, **91**, 045114 (2015).

[54] Z. K. Liu, J. Jiang, B. Zhou, Z. J. Wang, Y. Zhang, H. M. Weng, D. Prabhakaran, S. K. Mo, H. Peng, P. Dudin, T. Kim, M. Hoesch, Z. Fang, X. Dai, Z. X. Shen, D. L. Feng, Z. Hussain, and Y. L. Chen, A Stable Three-Dimensional Topological Dirac Semimetal Cd₃As₂, *Nature Material*, **13**, 677-681 (2014).

[55] Ebert, D. Ködderitzsch, and J. Minár, Calculating Condensed Matter Properties Using the KKR-Green's Function Method—Recent Developments and Applications *Rep. Prog. Phys.* **74**, 096501 (2011).

[56] J. Braun, J. Minár, and H. Ebert, Correlation, Temperature and Disorder: Recent Developments in the One-Step Description of Angle-Resolved Photoemission, *Phys. Rep.* **740**, 1 (2018).

CHAPTER 6

SUMMARY AND OUTLOOK

In the first part of this thesis, we investigated the effects of spin excitons on the surface states of samarium hexaboride (SmB_6), which has been proposed to be a candidate topological Kondo insulator material. As described in Chapter 4, spin excitons are the elementary bulk magnetic excitations that occur in the gap of paramagnetic Kondo insulators with energies in the range of 12 to 14 meV. The intensity of a spin-exciton peak increases and the peak-width decreases with decreasing temperature. The narrow linewidth of the spin exciton, which is an evidence for the long lifetime of these magnetic excitations, is caused by the absence of an electron-hole pair decay channel within the bulk hybridization gap. Existence of large-amplitude, low-frequency spin-flip scattering at the surface would result in the surface states not being completely protected from back-scattering and would give rise to a resonant peak in the low-temperature surface electronic density of states.

The predicted spin-exciton resonance happens in the bulk gap of SmB_6 , which is on the order of 20 meV. Because of such relatively narrow energy scale, the photoemission experiments must be performed with an instrument facilitating very high (few meV) energy resolution. Furthermore, since the above-mentioned resonance is a many-body effect, it is expected to have a significantly reduced spectral weight. Thus, the resulting spectral feature is expected to be identifiable in the difference between the high-temperature and low-temperature angle-integrated photoemission spectra.

In order to observe this feature, high-resolution valence-band photoemission measurements were carried out in the normal-emission experimental geometry using

linearly p -polarized light with the photon energy of 35 eV at the 1³ end-station of the BESSY II storage ring of the Helmholtz-Zentrum Berlin, where the total experimental resolution is estimated to be approximately 3 meV. By examining the difference of the angle-integrated spectra recorded at the sample temperatures of 20 and 1.2 K, we found that the density of states exhibits a low-temperature peak located at approximately -9 meV. The difference spectrum shows that this feature has its intensity derived from the X and Y points and is of surface origin. We identify this peak as a resonance in the surface electronic density of states caused by the coupling of the surface states to the in-gap spin-exciton excitations. Our valence-band angle-integrated photoemission experiment also reveal the presence of a V-shaped density of states within the bulk gap and, hence, we estimate that the Weyl point and the chemical potential reside within the bulk gap and have very similar energies.

Calculations show that the near Fermi-energy spin-exciton-driven scattering is thermally-activated and should only appear below the temperature of $T \sim 25$ K. The scattering rate has almost completely saturated for temperatures below 10 K. This temperature is considerably lower than the temperature at which the bulk hybridization gap is first observed. Therefore, we argue that the formation of the Fermi liquid that is responsible for the surface conduction should only occur at very low temperatures and may be responsible for the plateau in the resistivity at 5 K.

In the second part of this thesis, we investigated the electronic structure of the strongly-correlated oxide NdNiO_3 grown on LaAlO_3 along the unconventional pseudocubic [111] direction and buried under 4 u.c. of an insulating oxide LaAlO_3 . It is predicted that transition metal oxides grown along the highly polarized pseudocubic [111]

direction could host several interesting topological phases due to the similarity of the lattice structure to graphene, as well as the strong electronic correlations due to the confinement of electrons along the out-of-plane direction.

Soft x-ray angle-resolved photoemission measurements were carried out at the high-resolution ADDRESS beamline of the Swiss Light Source. All the measurements were carried in the near-normal emission (NE) [111] experimental geometry and the sample surface temperature was set at 100 K. In order to map the electronic structure of 2 u.c. NdNiO₃ layer, we performed angle-resolved photoemission measurements in the soft x-ray regime with photon energy of 642 eV, effectively increasing the inelastic mean free path of the electrons. At this photon energy the final photoelectron momentum highlighted a high symmetry point along the k_z direction in the extended BZ picture, which was confirmed by scanning the photon energy and obtaining a k_x - k_z ARPES map. Angle-resolved E_b - k_x map obtained at the photon energy of 642 eV along the K' - Γ -K high-symmetry direction showed excellent agreement with the theoretical calculations for the AFM ordering of the Ni sites with P1 symmetry of the 1×1 lattice.

To identify the elemental and orbital origins of the key features in the valence-band spectra, we utilized resonant photoemission spectroscopy at the Ni L_2 absorption threshold, at photon energies of 868.5 eV and 873.4 eV corresponding to the 'off' and 'on' resonant conditions for the Ni L_2 absorption edge, respectively. The results from resonant photoemission measurements exhibits two distinct resonant features near the Fermi level corresponding to the strongly-hybridized Ni $3d$ states with oxygen $2p$ states, fully-consistent with the first-principles GGA+ U calculations.

In addition to this, angle-integrated photoemission measurements carried out in the hard x-ray regime ($h\nu = 6.45$ keV) probed the entire depth of the sample and hence provided a way to perform a meaningful comparison of the experimental valence-band spectra with the theoretical DOS calculations for the entire superlattice. The measurements revealed the presence of a valence-band bandgap ($E_{\text{VB-max}} - E_{\text{F}}$) of 265 meV, suggesting that the full bandgap of NdNiO₃ (111) is at least this large, consistent with the theoretical value of 1 eV, predicted by DFT+*U*.

In summary, a combination of bulk-sensitive soft- and hard x-ray photoemission techniques was shown to be an effective methodology for probing momentum-resolved electronic band dispersion of a buried two-dimensional NdNiO₃ (111) layer in a geometrically-engineered [2 u.c. NdNiO₃ / 4 u.c. LaAlO₃] ×3 superlattice, and to directly measure its MEW-DOS. Our results, in conjunction with the first-principles DFT+*U* calculations, provide a direct evidence for the formation of a new AFM orbital arrangement with the P1 symmetry in a 1×1-unit cell in graphene-like NdNiO₃. Furthermore, our results demonstrate a unique way of investigating momentum-resolved and angle-integrated electronic structure of novel quantum materials which are buried within heterostructures and superlattices.

APPENDICES

APPENDIX A

ANALYSIS OF THE FOUR-DIMENSIONAL DFT DATA FOR ARPES INTERPRETATION

As mentioned in Chapter 3, four-dimensional datasets can be obtained in the following format from DFT calculations:

$$DFT = [b_1, b_2, b_3, \text{band index}]$$

If we now arrange the reciprocal lattice unit vectors in a matrix, as follows:

$$G = \begin{bmatrix} b_1^x & b_2^x & b_3^x \\ b_1^y & b_2^y & b_3^y \\ b_1^z & b_2^z & b_3^z \end{bmatrix}$$

transformation between k -points in the parallelepiped $k_{\text{parallelepiped}}$ formed by b_1 , b_2 and b_3 (reciprocal lattice vectors) and the k -points in momentum space $k_{\text{momentum-space}}$ can be obtained by the inverse of the reciprocal lattice unit matrix defined above:

$$k_{\text{parallelepiped}} = G^{-1} \times k_{\text{momentum-space}}$$

k -points in momentum space $k_{\text{momentum-space}}$ can be obtained in two steps. First, we can start with the normal emission geometry and map out a linecut in the momentum-space, as follows:

$$k_{\text{initial}} = \left[\begin{array}{c} k_e \sin(\theta_{TOA}) + k_{hv} \cos(\theta_{inc}) \\ 0 \\ 0.5124 \sqrt{KE_e \cos^2(\theta_{TOA})} + V_0 - k_{hv} \sin(\theta_{inc}) \end{array} \right]; k_e = \sqrt{\frac{2mKE_e}{\hbar^2}}$$

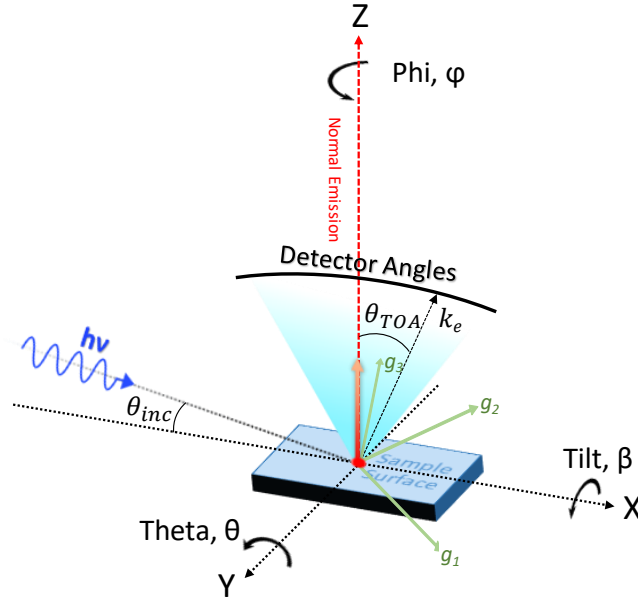


Figure (A.1) - Schematic diagram identifying the global coordinate system and the axes of rotations along the x, y and z directions.

where KE_e is the kinetic energy of the photoelectron in eV, k_e is the photoelectron momentum, V_0 is the inner potential (in eV) as explained in Chapter 1 and θ_{TOA} is the take-off-angle as measured from normal emission direction. Here, we also considered the effects of the photon momentum (k_{hv}) on the final photoelectron momentum, which cannot be neglected for high excitation energies in the soft and hard x-ray regimes. After introducing the $k_{initial}$, as described above, and then, by rotating the line-cut in momentum-space along the azimuth angle (φ), tilt angle (β) and theta angle (θ), as shown schematically in Figure (A.1), we can obtain the desired datapoints in momentum-space from the tilt-scan measurements or the photon-energy-scan measurements, as follows:

$$k_{rotated} = \mathbf{Rot}_{[001]}^{Phi} \times \mathbf{Rot}_{[100]}^{-Tilt} \times \mathbf{Rot}_{[010]}^{-Theta} \times k_{initial}$$

where $\mathbf{Rot}_{\vec{a}}^{\alpha}$ is a global rotation matrix about a unit vector \vec{a} with an angle of α . At the end, $k_{rotated}$ could be used to obtain the band-energy information from the DFT calculations for each of the points in the momentum-space.

APPENDIX B

DIFFERENCE BETWEEN THE 1×1 AND $\sqrt{3} \times \sqrt{3}$ STRUCTURES FOR PEROVSKITES ALONG $[111]$

Figure (S.2.1) shows the *structural diagrams* of the perovskite structure along the conventional $[001]$ direction (a), and the difference between the (1×1) and $(\sqrt{3} \times \sqrt{3} R(30^\circ))$ symmetries (b and c) along the $[111]$ direction. For clarity, NdNiO_3 structure is depicted in the pseudocubic notation (a) and the oxygen atoms are not shown (b, c). This diagram is mainly useful in defining the sizes of the corresponding unit cells.

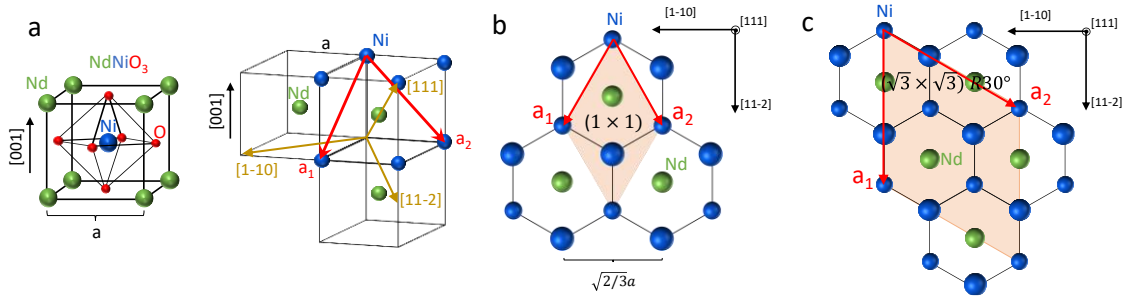


Figure (B.1) - Schematic diagrams of perovskite structures along $[001]$ and $[111]$ pseudocubic directions.

APPENDIX C

AFM, XRD AND STEM MEASUREMENTS OF $\text{LaAlO}_3/\text{NdNiO}_3$ [111]

In order to address the morphology of the sample, atomic force microscopy (AFM) measurements of an $[\text{2NdNiO}_3/4\text{LaAlO}_3]$ (111) film grown on LaAlO_3 (111) substrate has been performed and shown in Figure (C.1 a). The surface roughness was found to be approximately 200 pm (less than one-unit cell), which confirms smooth surface morphology of the film. *In-situ* RHEED (reflection high-energy electron diffraction) imaging, recorded during the growth confirms atomic layer-by-layer growth of each unit cell along the [111] direction is shown in Figure (C.1 b). The details of RHEED characterization could be found in prior studies [1,2]. The streak pattern observed along the Laue circles infers smooth surface morphology of the surface and entirely *excludes* the possibility of faceted morphology of the sample [3].

Additional analysis of the HAADF-STEM image is shown in Figure (C.2). The intensity scan along a long column, indicated in the magnified HAADF-STEM image

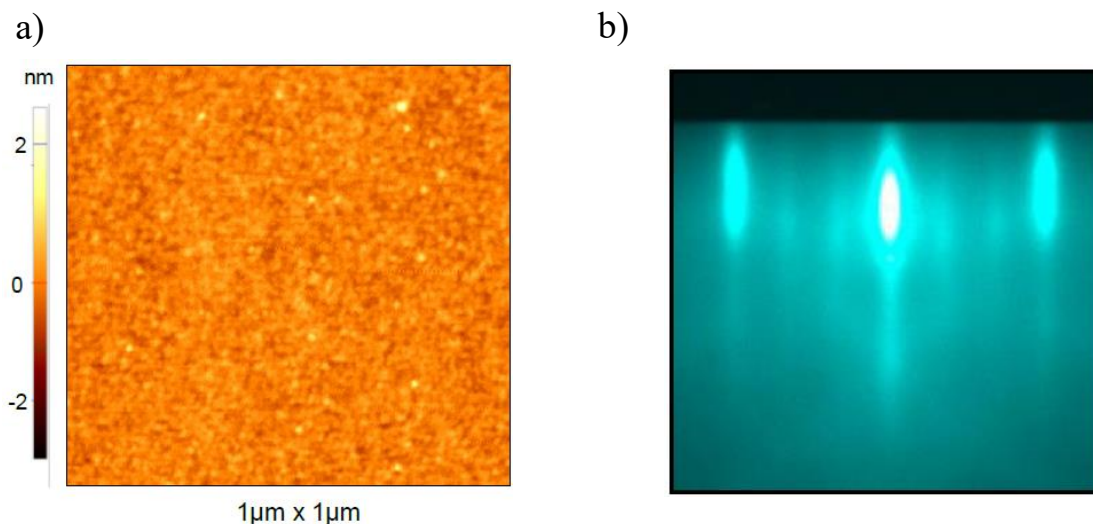


Figure (C.1) - a) AFM image revealing surface morphology b) RHEED image recorded during the growth confirming atomic layer-by layer growth of each unit cell along [111] direction.

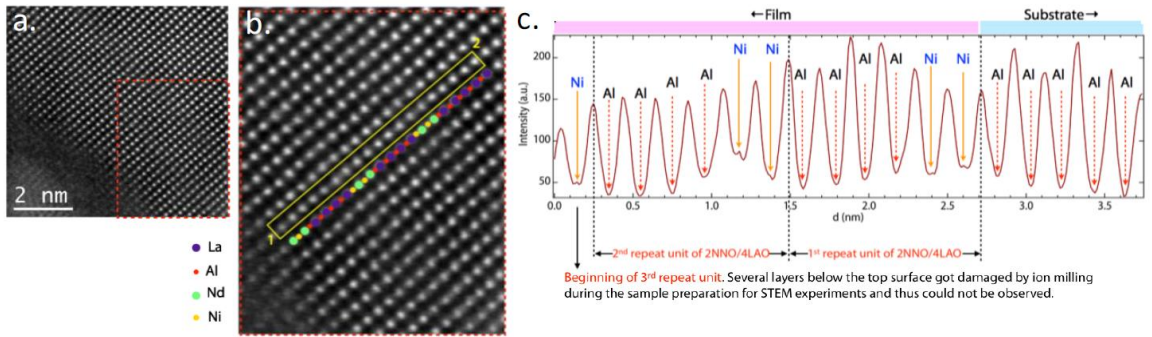


Figure (C.2) - HAADF-STEM image shown in (a) and intensity scan along a long column, indicated in the magnified HAADF-STEM image (b) and plotted in (c).

(panel b) has been plotted in panel (c). As seen, while Al and O ions cannot be discerned due to their low atomic numbers, the intensity scans clearly demonstrate the presence of *two* full repeat units of [2NNO/4LAO] and the beginning of a *third* repeat unit. Common for STEM of ultra-thin oxides, the ion-milling used for the sample preparation damages several layers from the top surface, resulting only in the partial imaging of the 3rd [2NNO/4LAO] repeat unit. This result confirms the proper [2NNO/4LAO] structural layering of the superlattice. Most importantly, this STEM imaging also establishes the presence of 2 NNO layers (separated by 4 u.c. of LAO). It should be noted that small local cation disorder at the interfaces cannot be entirely ruled out.

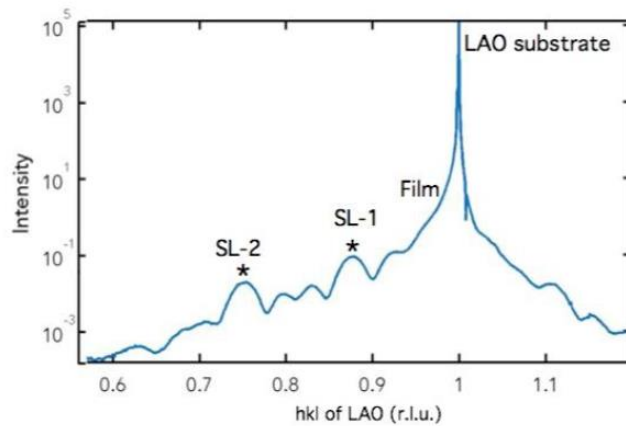


Figure (C.3) - XRD measurement to probe the crystal structure.

Since STEM is a very local probe of the structure, additional high-resolution synchrotron-based XRD measurements were also performed [3], which probes the crystal structure over a much larger and statistically-significant length scale is shown in Figure (C.3). Apart from confirming the desired growth along the [111] direction, the XRD spectrum exhibits thickness fringes along with the superlattice reflections (marked by *) as expected for a 2NNO/4LAO repeat unit (= 6-unit cells), both implying very sharp interfaces over the macroscopically large length scale. The presence of such superlattice reflections and the intensity variation over several orders of magnitude attest to the atomic sharpness of the interfaces, excluding the possibility of chemical disorder over the long-range scale.

APPENDIX D

ADDITIONAL ISOENERGETIC K_X - K_Y MAPS FOR NdNiO_3 [111] (THEORY)

Isoenergetic cuts through the band structure in reciprocal space for the majority (top row) and minority (bottom row) bands, calculated for the binding-energy range from -0.075 eV to -3.58 eV, and spanning the major Ni $3d$ features in the VB manifold is shown in

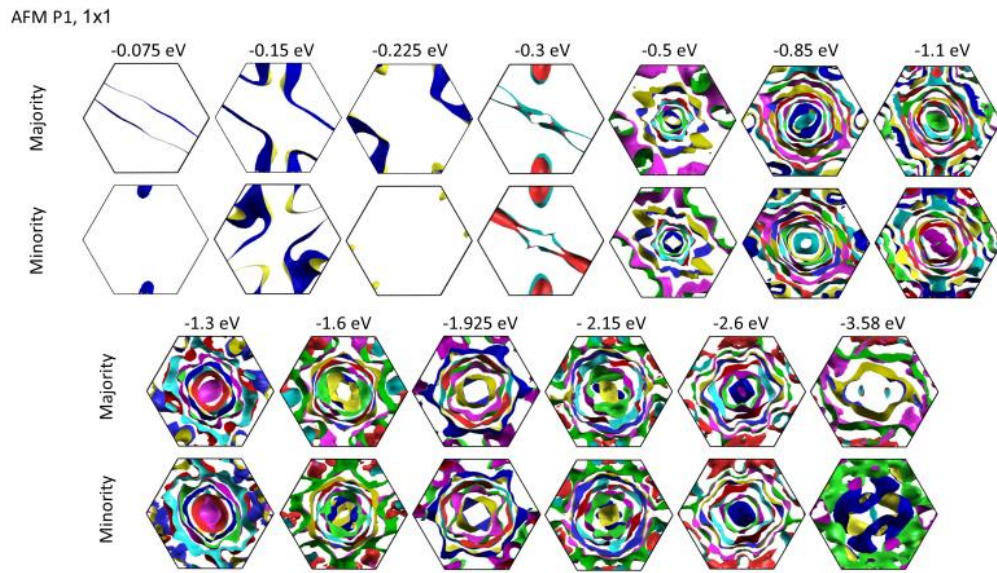


Figure (D.1) - Additional isoenergetic cuts through the band structure in reciprocal space for the majority (top row) and minority (bottom row) bands.

Figure (D.1).

APPENDIX E

ADDITIONAL E_B - k_x MAPS FOR P1 AND P3 SYMMETRIES (THEORY)

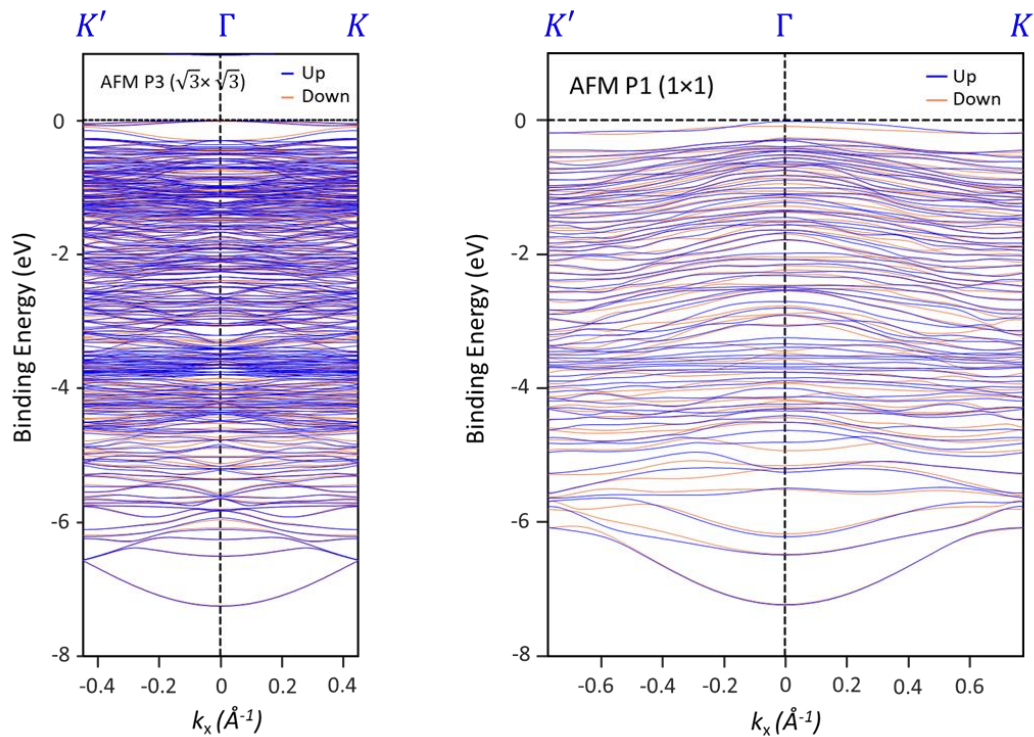


Figure (E.1) – Additional E_b - k_x band-structure calculations for P1 and P3 symmetry.

References Cited in Appendices

- [1] S. Middey, D. Meyers, D. Doennig, M. Kareev, X. Liu, Y. Cao, Z. Yang, J. Shi, L. Gu, P. J. Ryan, R. Pentcheva, J. W. Freeland, and J. Chakhalian, *Phys. Rev. Lett.* **116**, 056801 (2016).
- [2] S. Middey, P. Rivero, D. Meyers, M. Kareev, X. Liu, Y. Cao, J. W. Freeland, S. Barraza-Lopez and J. Chakhalian, *Sci. Rep.* **4**, 6819 (2014).
- [3] S. Middey, D. Meyers, D. Doennig, M. Kareev, X. Liu, Y. Cao, Z. Yang, J. Shi, L. Gu, P. J. Ryan, R. Pentcheva, J. W. Freeland, and J. Chakhalian, Mott Electrons in an Artificial Graphenelike Crystal of Rare-Earth Nickelate, *Phys. Rev. Lett.* **116**, 056801 (2016).